Recovery of Cerebrovascular Morphodynamics from Time-resolved Rotational Angiography

张翀
CHONG ZHANG

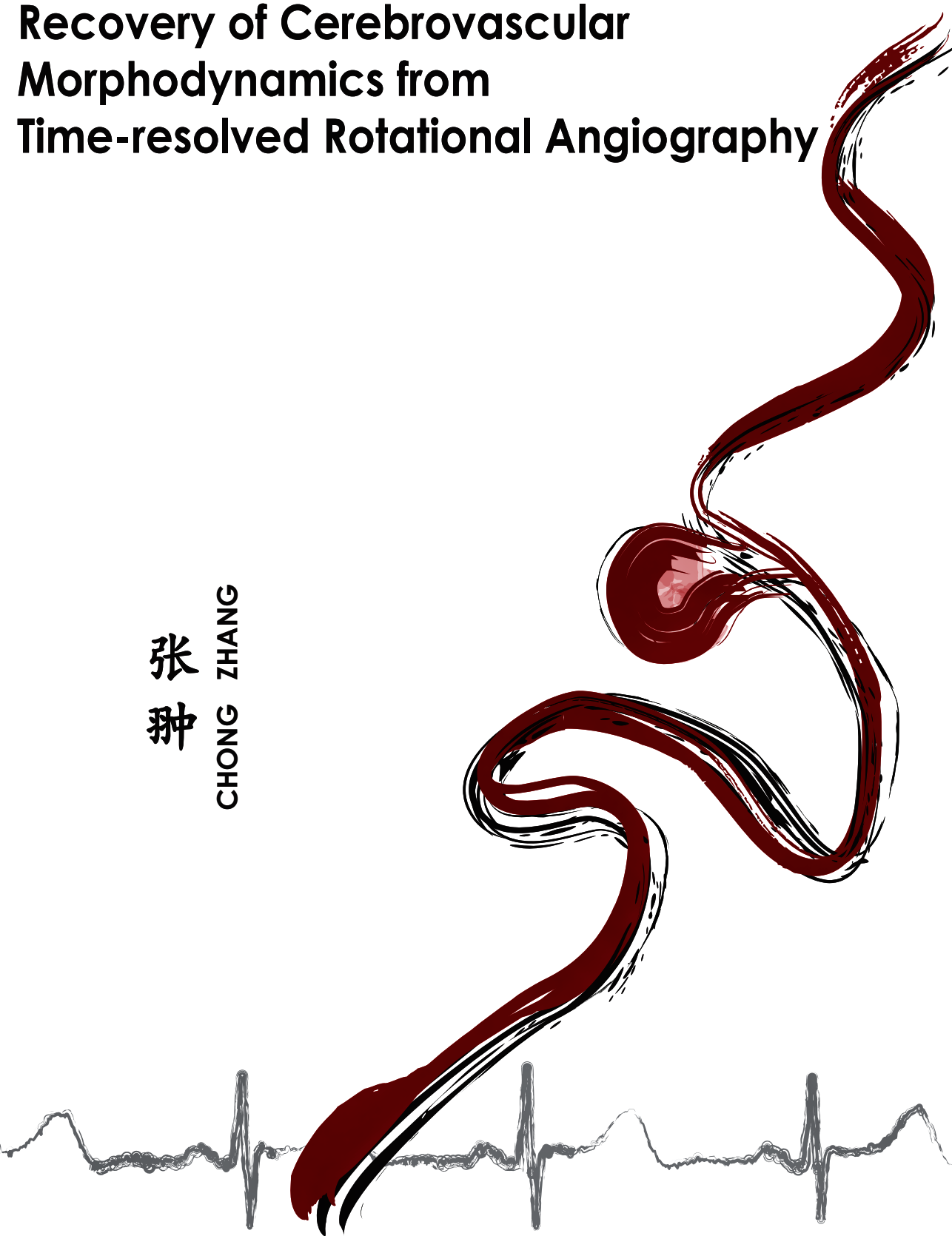

Recovery of cerebrovascular morphodynamics from time-resolved rotational angiography

A thesis submitted by Chong Zhang in partial fulfilment of the requirements for the degree of Doctor of Philosophy and for the European Doctor Mention.

Departament de Tecnologies de la Informació i les Comunicacions
Universitat Pompeu Fabra

2011

Cover design by the author using Adobe Illustrator (version CS5). The background is a fragment of an X-ray cerebral angiography taken from a clinical dataset. The red and black calligraphic strokes symbolically represent the dynamics of the blood moving through the artery and aneurysm. These two colors represent the mixing of blood and contrast agent during the X-ray angiography acquisition. The ECG-like strokes express the heart pumping blood to different arteries, causing the rhythmic change of blood pressure and the consequent vascular wall motion. A motion sequence at different phases represented by vectors on aneurysm wall surface is shown on the back page.

Recovery of cerebrovascular morphodynamics from time-resolved rotational angiography

ISBN: 978-8-469-45625-5
Depósito legal: B-26.232-2011

Typeset in LaTeX 2_ε. Thesis class courtesy of Dr. Avan Suinesiaputra and Dr. Sri-Kaushik Pavani.

Supervisor: Dr. Alejandro F. Frangi
Universitat Pompeu Fabra

Co-supervisor: Dr. Maria-Cruz Villa-Uriol
Universitat Pompeu Fabra

This work was carried out in the Center for Computational Imaging and Simulation Technologies in Biomedicine (CISTIB). This work was partially supported by the CENIT-CDTEAM grant funded by the Spanish Ministry of Science and Innovation (MICINN-CDTI), and partially generated in the framework of the @neurIST Integrated Project, which is co-financed by the European Commission (*IST-027703*), partially funded by the Spanish Ministry of Science and Innovation (MICINN), partially funded by the European Regional Development Fund (ERDF) through the research project STIMATH (*TIN2009-14536-C02-01*) and by Philips Healthcare (Best, The Netherlands).

Financial support for the publication of this thesis was kindly provided by CISTIB.

In memory of my grandfather,
whose love and encouragement shall reside
within my heart forever...

致 我最亲爱的爷爷蒋经笥

Abstract / Resumen / 摘要

Abstract: Over the last decade, there has been a growing interest in assessing cerebral aneurysmal wall motion, because of its potential connections to the biomechanical conditions of the vessel wall, which could eventually aid the prediction of aneurysmal rupture risk. Such quantification could provide a valid surrogate for the vascular wall status and integrity. However, the vast majority of current morphological indices used in the literature to predict growth and rupture in cerebral aneurysms do not take into account the temporal changes that occur during the cardiac cycle. This is because these indices are derived from image modalities that do not provide sufficient temporal and/or spatial resolution to obtain dynamic aneurysm information, which is expected to be similar to or below image resolution. Among currently available vascular imaging techniques, 3D rotational angiography (3DRA) and digital subtraction angiography (DSA) have the highest spatial (and temporal) resolution. Still, for a human operator relying solely on qualitative visual observation, even when using images from these modalities, to objectively analyze the small motion and shape changes of the cerebrovasculature of an individual throughout the cardiac cycle is difficult, if not impossible. Therefore, the availability of a robust morphodynamic analysis tool is needed.

In this context, this thesis focuses on developing techniques to estimate, quantify and analyze cerebrovascular wall motion, particularly aneurysmal wall motion, using such modalities. The main contributions of the thesis are: 1) a first methodology to estimate and model patient-specific cerebrovascular morphodynamics over one cardiac cycle, through a proposed multiple 2D to 3D image registration framework; 2) an extension of this methodology to provide robust and efficient estimates of cerebrovascular wall motion for clinical evaluation and for further biomechanical modeling of the cerebrovascular wall; 3) a patient study that demonstrates the validity of the developed techniques from clinical practice, through an analysis of 3DRA and DSA images. Each of these contributions is published in or submitted to a peer-reviewed international journal.

Resumen: Durante la última década se ha dado un creciente interés en la evaluación del movimiento de la pared vascular en aneurismas cerebrales. Éste hecho ha sido motivado en gran medida por la relación existente entre dicha motilidad y sus condiciones biomecánicas, pudiendo éstas llegar a ser útiles en la predicción del riesgo de ruptura del aneurisma cerebral analizado. De este modo, de ésta cuantificación, se podría llegar a derivar un indicador indirecto del estado e integridad de la pared vascular. Sin embargo, la gran mayoría de los índices morfológicos utilizados en la actualidad para predecir crecimiento y ruptura de aneurismas cerebrales no consideran los cambios que se producen en el tiempo a lo largo del ciclo cardíaco. Esto se debe a que dichos índices se obtienen a partir de modalidades de imagen que no proporcionan suficiente resolución espacial y/o temporal para obtener información dinámica del aneurisma, cuyo rango de variación se espera sea similar o inferior a la resolución de la imagen. Entre las técnicas de imagen vascular disponibles en la actualidad, la angiografía rotacional 3D (3DRA) y la angiografía de substracción digital (DSA) son las que ofrecen la mayor resolución espacial (y temporal). De todos modos, aún utilizando imágenes de estas modalidades, el análisis objetivo de pequeñas diferencias de forma y movimiento en los vasos cerebrales de un individuo a lo largo de un ciclo cardíaco es difícil, si no imposible para un operador humano utilizando únicamente medidas cualitativas guiadas por inspección visual. Por lo tanto, la disponibilidad de herramientas robustas para el análisis morfodinámico de la vasculatura cerebral resulta necesaria.

En este contexto, la investigación de esta tesis se concentra en el desarrollo de técnicas para estimar, cuantificar y analizar el movimiento de las paredes de los vasos cerebrales, con particular énfasis en el movimiento de la pared en aneurismas, utilizando las modalidades indicadas anteriormente. En líneas generales, esta tesis presenta tres contribuciones principales: 1) una primera metodología de estimación y modelado morfodinámico de vasos cerebrales a lo largo de un ciclo cardíaco, utilizando una técnica de registrado de imágenes 2D-3D; 2) una metodología extendida para proporcionar una estimación robusta y eficiente del movimiento de las paredes de los vasos cerebrales para su evaluación clínica y posterior modelado biomecánico de dichas paredes; 3) un estudio sobre una población de pacientes que demuestra la validez de las técnicas desarrolladas en la práctica clínica, a través del análisis en imágenes de 3DRA y DSA. Cada una de estas contribuciones ha sido publicada o se encuentra en fase de revisión en revistas internacionales indexadas.

摘要: 在过去的十年里，人们对脑动脉瘤壁的运动有了越来越大的兴趣，这是因为人们认为这项研究与血管壁的生物力学条件分析有潜在的联系，而后者又有助于进行动脉瘤破裂风险预测的进一步研究。但是，当前大多数主要文献中讨论的脑动脉瘤形态增长和破裂的风险因素并没有考虑心动周期内发生的形态变化。这是因为这些因素是从不同医学图像技术中分析得出的，而这些图像技术不能提供足够的时间和空间分辨率以获得动脉瘤的这种非常小的动态变化信息。在现有的脑成像技术中，三维旋转血管造影（3DRA）和数字减影血管造影（DSA）具有最高的空间（和时间）分

辨率。不过，即使借助于这类图像，仅靠人肉眼来客观地分析整个心周期过程中个体脑血管形状变化是非常困难的，或者说甚至是不可能的。因此，一个可靠的动态形变分析工具具有帮助颅内动脉瘤的术前规划和治疗方案的选择的潜在力。

本论文的研究主要集中于开发算法来估算，量化和分析在3DRA图像中脑血管壁的运动，尤其是动脉瘤壁的运动。总的来讲，本论文的主要贡献有： 1）一个采用多帧2D / 3D图像配准的方法，用于对人脑血管动态信息进行建模；2）一个基于方法一但更为高效完善的算法，以便用于临床评估和进一步的脑血管壁运动生物力学建模；3）一个基于临床病人数据的分析研究，通过对3DRA和DSA影像的多模态相关性分析来验证本论文提出的技术在临床实践中的有效性。以上的每一项贡献都分别在一份被同行评审的国际期刊上发表了或审批中。

Contents

List of Figures

List of Tables

List of Acronyms

1D	One-dimensional
2D	Two-dimensional
3D	Three-dimensional
3D+t	3D plus time
3DRA	Three-dimensional Rotational Angiography
4D	Four-dimensional
ACA	Anterior Cerebral Arteries
AComA	Anterior Communicating Artery
ASG	Anti-Scatter Grid
BA	Basilar Artery
CA	Contrast Agent
CB	Cone-Beam
CBCT	Cone-Beam CT
CeVD	Cerebrovascular Disease
CFD	Computational Fluid Dynamics
CNR	Contrast-to-Noise Ratio
CPU	Central Processing Unit
CT	Computed Tomography
CTA	Computed Tomography Angiography
CVD	Cardiovascular Disease
DRR	Digitally Reconstructed Radiographs
DSA	Digital Subtraction Angiography
ECG	Electrocardiogram
FBP	Filtered Back Projection
FDK	Feldkamp Davis Kress
FFT	Fast Fourier Transform
FOV	Field Of View
GPU	Graphics Processing Units
HU	Hounsfield Units
ICA	Internal Carotid Arteries
II	Image Intensifier

MCA	Middle Cerebral Artery
MR	Magnetic Resonance
MRA	Magnetic Resonance Angiography
MTF	Modulation Transfer Function
PCA	Posterior Cerebral Arteries
PCoA	Posterior Communicating Artery
ROI	Region Of Interest
SD	Standard Deviation
SID	Source to Intensifier Distance
SNR	Signal-to-Noise Ratio
SOD	Source to Object Distance
SPR	Scatter-to-Primary Ratio
UIA	Unruptured Intracranial Aneurysms
VOI	Volume Of Interest

Preface

This thesis marks the fulfillment of my journey on obtaining my PhD degree in Universitat Pompeu Fabra. I would like to thank several people who have contributed to the accomplishment of this thesis.

First of all, I would like to thank my advisor Alejandro Frangi, who introduced me to the medical imaging research field, guided me to carry out research, and provided me the financial support. Maria-Cruz Villa-Uriol was my daily supervisor during the last four and a half years of this thesis work. Her continuous commitment to my work and organizational aspects have been fundamental. I am also very grateful to all other co-authors of the different parts of this thesis, Mathieu De Craene, Jose-Maria Pozo, Ruben Cardenes, Bart Bijnens, Juan Macho, Vincent Costalat, Alain Bonafé, with whom I have had pleasant collaborations and constructive discussions.

I would like to express my sincere gratitude to Prof. Alain Bonafé, Vincent Costalat, and Hans Aerts who offered me the opportunity to have a three-month research stay at CHU Montpellier, Service de Neuroradiologie, Hôpital Gui de Chauliac, Montpellier, France. They provided me the convenience of accessing clinical data and they were always available and helped me understanding many aspects of radiology clinics. Special mention also goes to all members from the department, for their collaborations during my stay.

I would also like to thank Dr. Daniel Rüfenacht and Luca Augsburger from Geneva University Hospitals (HUG), for permitting us to use their aneurysm silicone phantoms, and Dr. Jordi Blasco from Hospital Clínic de Barcelona, Dr. Elio Vivas from Hospital General de Catalunya, and Roel Hermans from Philips Healthcare, Best, The Netherlands, for the 3DRA phantom acquisitions.

A journey becomes easier once you get company. I am grateful to all the past and current colleagues of CISTIB, who together have created a very friendly working environment and have accompanied me for lots of wonderful leisure time.

The research work carried out in this thesis was partially generated within the framework of the Integrated Project @neurIST (IST-2004-027703), financed by the European Commission, partially supported by CDTI CENIT-CDTEAM grant funded by the Spanish Ministry of Industry, partly supported by the Spanish Ministry of Science and Innovation (Ref. No. TIN2009-14536-C02-01), Plan E, and FEDER, and also partially funded by Philips Healthcare (Best, The Netherlands). CISTIB is part of ISCIII CIBER-BBN (CB06/01/0061).

I owe tremendously to my grandmother, whose simple and unconditional love has

always kept me warm throughout my life. I am so deeply appreciative of my parents, who have always supported every single decision or achievement that I have ever made, and will remain so.

1

Introduction

1.1 Cerebral aneurysms

1.1.1 Cerebral aneurysms: a cerebrovascular disease

Cardiovascular diseases (CVD) are currently the number one cause of death in the world. Among CVD, cerebrovascular diseases (CeVD), such as stroke, are the second most common cause. Fig. 1.1 shows a detailed list of the top ten leading causes of death in the world, as published by the World Health Organization in 2008 [71]. This report estimated that 17 million people died from CVD in 2004, representing about 30% of all global deaths. Of these deaths, 7.2 million were due to heart attacks and 5.7 million due to CeVD. In addition, they are the cause of disability for several millions more people. CVD prevalence and costs are projected to remain the same or even increase substantially, as indicated by recent findings [31]. To limit this growing burden, effective prevention strategies are needed.

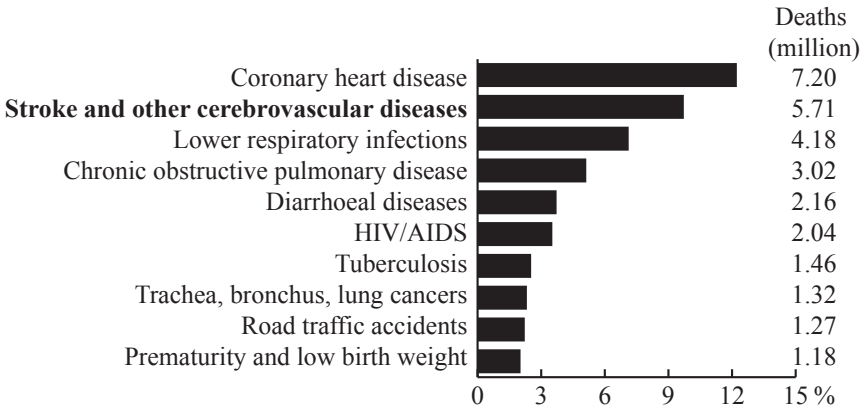

Figure 1.1: The 10 leading causes of death in the world, according to the estimates in "The global burden of disease: 2004 update", published in 2008 [71]. As a reference, the estimated total number of deaths in the world in 2004 was 59 million.

Cerebral aneurysms, the main cause of hemorrhagic strokes, usually form in areas where a blood vessel in the brain weakens, resulting in a bulging (or ballooning) of this part of the vessel wall [14]. They are usually found at or near arterial bifurcations, mostly at the Circle of Willis (Fig. 1.2), the vascular system that irrigates the basis of the brain [14]. Although the prevalence of unruptured cerebral aneurysms is unknown, it is estimated from autopsy studies to be between 1 and 5% in the adult population [70] and as high as 6% [116]. The most serious complication of a cerebral aneurysm is its rupture and the consequent aneurysmal subarachnoid hemorrhage (SAH). This subset of strokes has an incidence of sudden death of 12.4% and a fatality rate ranging from 32% to 67% after the hemorrhage [35, 40, 89, 120].

There are three options for treating intracranial aneurysms: pharmacological therapy, surgical therapy with clip ligation (clipping), and endovascular occlusion

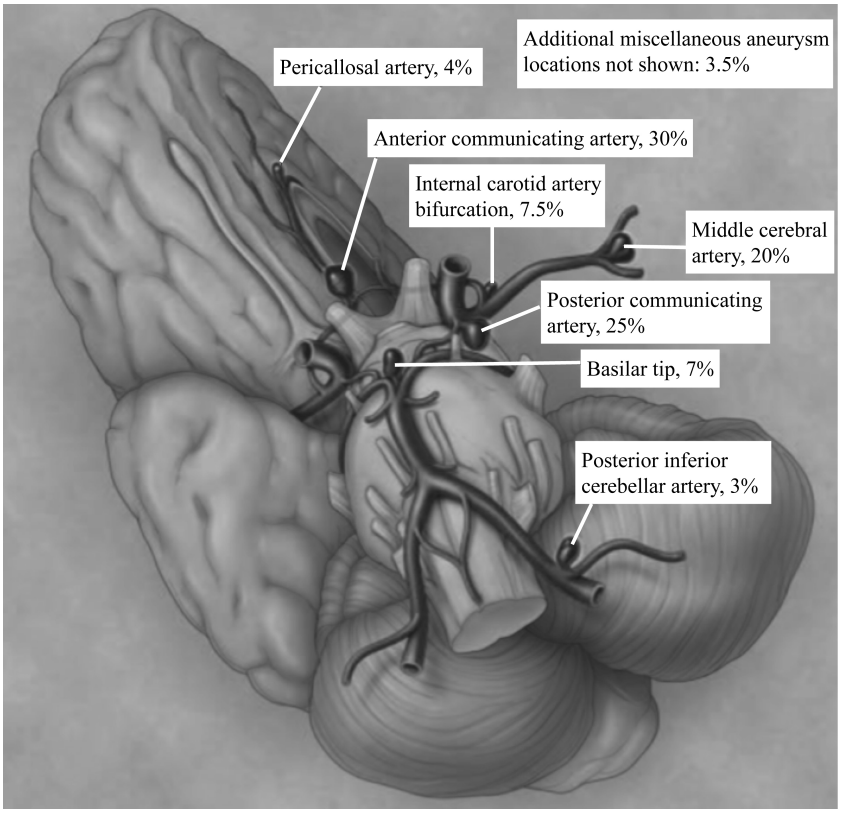

FIGURE 1.2: The most frequent locations of cerebral aneurysms in the intracranial vasculature. Reproduced with permission from [14]. (color version on page C1)

with the use of detachable coils (coiling) or a wire mesh tube either used as a scaffold to support the coils (stenting) or to cut off the blood supply (flow diverter). Although successful clipping is generally associated with definitive protection against rupture, the morbidity and mortality rates associated with clipping an unruptured aneurysm are relatively high [78]. In contrast, endovascular treatment of unruptured aneurysm is safe with less than 1% of mortality rate [97], but they are not cost effective. Thus the risks of aneurysm rupture with respect to its natural history against the risk of morbidity and mortality from an endovascular or surgical repair need to be carefully balanced. Although unresolved controversies remain as to the best treatment option for an individual patient, the outcome for patients treated before an aneurysm rupture is much better than for those treated afterwards.

1.1.2 Imaging options and applications

At present, there are three methods of choice for identifying a cerebral aneurysm and its morphologic features: computed tomography angiography (CTA) after a venous injection, magnetic resonance angiography (MRA), and angiography by direct intra-arterial catheterization (catheter angiography): either 3D rotational angiography (3DRA) or digital subtraction angiography (DSA).

Depending on the stage within the cerebral aneurysm patient care cycle, these imaging modalities play different roles. Catheter angiography presents the highest spatial resolution [25] and is considered as the benchmark [14]. Therefore, it is usually routinely performed during an endovascular treatment. Nevertheless, the requirement of catheterization and contrast agent injection makes it invasive and ionizing to the patient. Because of the less invasive nature of CTA and MRA, these two modalities are used in standard clinical practice at early diagnostic stages as well as for patient screening and monitoring [14].

In the recent years, imaging has also played an important role to enable the personalization of risk assessment and treatment. Research efforts have been devoted to the patient-specific virtual modeling and simulation of this disease. Aspects such as vascular morphology, hemodynamics and structure have been evaluated and included in complex image and simulation-based management pipelines [110, 111]. In this context, the European project @neurIST [7, 110] catalyzed some of these efforts, aiming at the transformation of the management of cerebral aneurysms by providing new insights, personalized risk assessment, and methods for the design of improved medical devices and treatment protocols.

1.1.3 Understanding aneurysm formation, growth and rupture

The clinical management of ruptured and unruptured cerebral aneurysms has not been fully determined, as the exact mechanisms by which cerebral aneurysms initiate, develop, grow, and rupture are unknown. Not all aneurysms rupture. Actually, between a 50% and 80% of them never do [14]; however, the challenge is to discriminate those at risk of rupture from those that will not rupture. Therefore, to gain a better understanding of the natural history of unruptured intracranial aneurysms (UIA), an epidemiological project was undertaken by the International Study of Unruptured Intracranial Aneurysms (ISUIA) Study Group [69, 70]. As a conclusion, size and location were identified to play an important role in predicting rupture risk, especially in patients who did not previously have SAH. Also, to gain a better understanding of the risks associated with aneurysm surgical or endovascular repair, a multi-center, prospective randomized study was carried out in the International Subarachnoid Aneurysm Trial (ISAT), where the safety and efficacy of endovascular coil treatment and surgical clipping for the treatment of ruptured brain aneurysms were compared [62]. The study found that, in patients equally suited for both treatment options, endovascular coil treatment produces substantially better patient outcomes than surgery in terms of survival free of disability at one year.

To date, the main factors that have been investigated are: *morphological factors*

based on the aneurysm and vascular geometry [26, 28, 61, 79]; *physical factors* that relate to physical exercise such as blood flow and contacts with the environment [21, 93]; *biological factors* that take into account biological processes involved in the various stages of aneurysm growth and coagulation [55]; *genetic factors* based on patient genetic phenotyping [90, 91, 125]; and other risk factors such as drugs abuse, smoking, contraceptives, hypertension, alcohol intake, *etc* [34, 42, 99], which are related to the pathogenesis and eventual rupture. Despite the intrinsic complexity of the problem and given the many factors involved [70], an additional difficulty with these studies is that they are usually based on selected patients population. For example, while there are reports indicating that a larger aneurysm is associated with a higher risk of rupture [69, 70, 83], in Japan it has been sporadically reported that small unruptured aneurysms present higher rates of rupture risk [63]. The state of current clinical research on aneurysm rupture risk is therefore rather primitive and controversial, as there are no clinically proven measurements to predict how, when, where, and why a particular type of aneurysm in a particular location of the body will rupture [22, 41].

1.2 Cerebral aneurysm wall motion

1.2.1 Importance of studying aneurysmal wall motion

Although little is known about the pathogenesis of cerebral aneurysms and the subsequent aneurysmal SAH, it is believed to be dependent on the complex interactions of multiple physiological and mechanical factors such as hemodynamics, wall biomechanics and mechanobiology [95]. Unfortunately, patient-specific vessel wall properties cannot be measured *in vivo* with current medical imaging techniques [49], making it difficult to predict further remodeling and assess prognosis in an individual patient. In many situations, an inverse problem approach based on a mathematical model for the biomechanics of the vasculature is a valid surrogate to estimate material and structural parameters [5, 46]. An example of such an approach consists in determining these unknown parameters by applying known boundary conditions on the vessel wall and analyzing its mechanical responses such as vascular wall motion.

Currently, only a few clinical studies are available to support the diagnostic value of examining motion information [30, 37, 43, 45, 74, 106, 124]. Previous studies have demonstrated that the aneurysm wall can vibrate or pulsate due to the fluctuations of flow [98], and that decreased pulsatile aneurysmal wall movement can cause a slight reduction in wall stress [103]. Both flow fluctuation and wall stress are thought to play a role in aneurysm progression and eventual rupture. On the other hand, a recently study [94] claims that the oscillatory rigid rotation observed *in vivo* in cerebral vasculature does not have a major impact on intra-aneurysmal hemodynamic variables, and that parent artery motion is unlikely to be a risk factor for aneurysm rupture. Therefore, it remains relevant to further discuss these controversial stand points. From a biomechanical point of view, recent research has revealed that localized variations in the aneurysmal wall stiffness and thickness are linked to local stress concentrations and changes in aneurysmal shape [17]. Such inhomogeneous distribution of the material properties in the aneurysmal wall may

translate into spatially inhomogeneous wall motion when exposed to the varying dynamic pressures occurring during the cardiac cycle [5, 46]. Moreover, there are studies suggesting that the direct visualization of wall motion abnormalities may be helpful for identifying weak spots in the cerebral vasculature [37, 45]. Therefore, the quantification of wall motion in cerebral aneurysms could be an effective surrogate for vascular wall status and integrity, which could indicate vascular weak spots and potentially aid the assessment of aneurysmal rupture risk. Additionally, it can be of use for providing boundary conditions for computational simulations and as a validation tool for biomechanical modeling of the vessel wall. All this information is thought to be able to help in the selection of the best therapeutic option for patients suffering from various vascular pathologies [111, 112].

However, the vast majority of current morphological risk factors for cerebral aneurysm growth and rupture do not take into account the temporal changes occurring during the cardiac cycle. Some examples of these factors are aneurysm size, aspect ratio or neck angle [6, 26, 28, 40, 41, 53, 61, 65, 69, 70, 72, 79, 83, 86, 104, 105]. This is because these factors are derived from image modalities that do not provide sufficient temporal and spatial resolution to obtain dynamic information about aneurysms, which is expected to fall in the sub-millimeter range (see in Table 1.1 a summary of currently reported motion amplitude ranges). Thus, it represents a challenge in terms of the available image resolution of current clinical imaging techniques. Consequently, for a human operator relying solely on qualitative visual observations, performing an objective analysis of such small motion throughout the cardiac cycle is difficult, if not impossible. As such, dedicated and objective tools in motion assessment are needed.

1.2.2 Imaging techniques for wall motion

Over the past couple of decades, various imaging techniques have been used in wall motion research, such as Doppler ultrasound [114], 2D cine phase contrast MRI [43, 60], 4D-CTA [30, 37, 44, 45], and DSA [18, 74]. Most of them focused on providing qualitative observations and detecting aneurysm wall motion. Only recently a few studies have intended to detect and further quantify motion [43, 45, 60, 67, 74, 106], and even fewer have been able to quantify motion throughout the cardiac cycle [43, 67, 74, 106]. A list of such publications is summarized in Table 1.1. However, no work has reported the use of 3DRA for this challenging research task.

Although 3DRA was not designed to provide dynamic 3D information, we will show why it has the potential to do so. A picture of a commercial 3DRA imaging suite (Allura Xper FD20/10, Philips Healthcare, Best, The Netherlands) is shown in Fig. 1.3. A 3DRA acquisition provides a sequence of 2D X-ray angiograms obtained from rotating views of the C-arm. A static and isotropic high-resolution 3D volumetric image is reconstructed from them. In addition, a physiological signal such as electrocardiogram (ECG) or blood pressure synchronized to the projections can be recorded. Typically, more than 100 projections are obtained during a 4-second scan, at constant time intervals and uniformly distributed over more than 200° along a circular trajectory. Fig. 1.4 illustrates the principle of 3DRA described. Since

TABLE 1.1: Previous work reporting both cerebral aneurysm and artery motion amplitude. M.A.=Max. amplitude; M.A.P.=Max. amplitude in percentage of the aneurysm diameter; M.V.P.=Max. volume change in percentage; n.a.=not available.

Motion	Ref./Year	Modality	Data	# Cases	M.A. (mm)	M.A.P.	M.V.P.
aneurysm	Meyer *et al.* [60]/1993	cine PC-MRI	in vivo	16	0.2-3.3	4-20%	n.a.
	Low *et al.* [52]/1993	-	simulation	1	n.a.	6%	n.a.
	Boecher-Schwarz *et al.* [11]/2000	laser sensor	ex vivo	8	0.1-0.25	1-2.5%	n.a.
	Ueno *et al.* [103]/2002	laser sensor	in vitro	1	0.1	n.a.	n.a.
	Torii *et al.* [102]/2006	-	simulation	1	0.7	14%	n.a.
	Valencia *et al.* [108]/2006	-	simulation	1	0.2-0.35	2-3%	n.a.
	Krings *et al.* [45]/2010	4D-CTA	in vivo	1	2	13.3%	n.a.
	Karmonik *et al.* [43]/2010	cine PC-MRI	in vivo	7	0.16-1.6	n.a.	n.a.
	Oubel *et al.* [74]/2010	DSA	in vivo	10	0.01-0.45	0.1-4.7%	n.a.
	Umeda *et al.* [106]/2011	4D-CTA	in vivo	4	0.7	n.a.	n.a.
artery	Warriner *et al.* [117]/2008	-	simulation	1	0.24-0.25	3.8-4.5%	n.a.
	Nishida *et al.* [67]/2011	4D-CTA	in vivo	10	n.a.	n.a.	3%

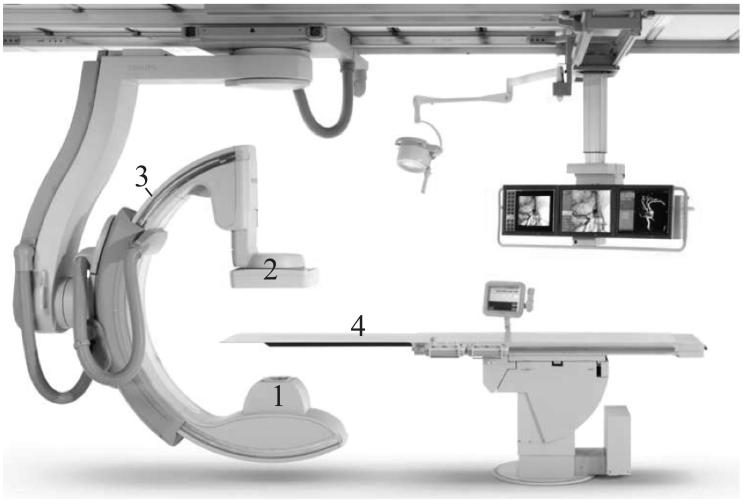

Figure 1.3: A picture of a flat panel 3DRA system Allura Xper FD20 (Philips Healthcare, Best, The Netherlands). 1. X-ray source; 2. Image detector; 3. C-arm that rotates around the patient; 4. Patient table. (color version on page C1)

the acquisition lasts for a few seconds, any vascular motion occurring during the acquisition is captured in the 2D projections. Thus, in principle, 3D aneurysmal motion could be derived from the combined image data obtained from a single standard 3DRA acquisition. In addition, the employment of a single acquisition has the merit of not exposing patient to additional radiation risk and facilitates its clinical take-up.

1.2.3 Motion estimation algorithms

Various techniques have been proposed for estimating motion or reconstructing dynamic 3D structures using projection images acquired from image modalities like 3DRA and cone beam computed tomography (CBCT). Unfortunately, they are not directly suitable for aneurysm motion analysis.

Most of these techniques, e.g., the ones based on dynamic CT [13], use a subset of projections belonging to the same motion state according to a time reference signal, and use this subset to reconstruct the object at that motion state. ECG-gated techniques [64, 80, 88] constitute the most typical approach, using iterative [10] or analytical [20, 88] reconstruction methods. Other methods have employed image registration based techniques to estimate the motion into projection motion-compensated 3D reconstruction process [84] or through projection matching in 2D spaces [9, 10, 109, 126] Recently, a technique [84] has been proposed to incorporate a 4D motion estimation into a projection motion-compensated 3D reconstruction

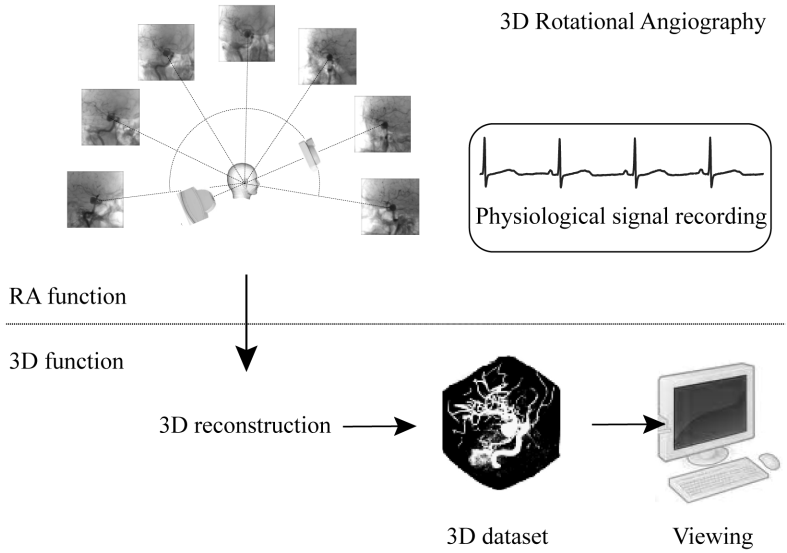

FIGURE 1.4: An illustration of the imaging principle of the 3DRA modality. More than 100 contrast-enhanced images are acquired by rotational angiography during a 4-second scan, at constant time intervals and uniformly distributed over more than 200° along a circular trajectory. A 3D volume automatically reconstructed from these image date can be viewed with real-time volume rendering. During the rotational run, a physiological signal can be synchronously recorded as well. (color version on page C1)

process by comparing the latter to an initial reference reconstruction. In other works [109, 126], continuous respiratory motion during a CBCT acquisition has been estimated by optimizing the similarity between the measured and the corresponding views of a deforming reference volume obtained from CT.

1.3 Aim and objectives of this thesis

It is the main aim of this thesis to present technical solutions for objectively estimating, quantifying and analyzing 3D cerebrovascular wall motion. Ultimately, such techniques should be useful for identifying patients at risk of aneurysmal rupture using their ability to identify weak spots in the vascular wall. These methods ideally should be used in clinical practice without exposing patients to additional radiation, i.e. employing the standard imaging protocol currently in place. In this case, 3DRA is the most suitable existing imaging technique, since it has the best combination of spatial and temporal resolutions and it is part of the clinical management care cycle of patients with a cerebral aneurysm. However, this modality was not originally designed for representing dynamic information of the imaged object. In this thesis,

we aim at retrieving the dynamic 3D morphology of cerebral aneurysms from a single 3DRA acquisition, combined with the recording of a physiological signal. This aim has been translated into the following specific objectives:

- To develop methodologies for the recovery of 3D plus time (3D+t) or 4D models of cerebral aneurysms from 3DRA.
- To provide methods to objectively pursue the quantification and characterization of the estimated motion.
- To evaluate the performance of the proposed techniques and to validate their feasibility of analyzing *in vivo* aneurysmal wall motion.

1.4 Overview of this thesis

In this thesis, we propose two methodologies to estimate 3D aneurysmal wall motion from 2D rotational angiography, and perform a validation study on clinical patient data with the purpose of aneurysmal wall motion characterization. The core contents of this thesis are structured in three chapters.

Chapter 2 describes the first proposed methodology to estimate and model patient-specific cerebrovascular morphodynamics over one canonical cardiac cycle. As opposed to employing typical reconstruction algorithms from projections, 3D morphology of the structure of interest at a given time instant is obtained by registering a sparse set of forward projections of the deformed 3DRA volume to 2D measured projections through a temporal weighting scheme. Motion over the cardiac cycle is represented by a sequence of such deformed 3DRA volume images estimated at multiple time instants in the cardiac cycle.

Chapter 3 aims to provide robust and efficient estimates of cerebrovascular wall motion for a clinical evaluation and for the further biomechanical modeling of the cerebrovascular wall. The algorithm framework described by the first proposed methodology is extended by employing a single 4D B-spline transformation model for the whole motion cycle to guarantee spatial as well as temporal consistency. The registration is optimized by measuring a single similarity metric between the entire measured and forward projection sequences. In the same chapter, a hybrid acceleration method is proposed, using a combination of software and hardware strategies. This method also results in a reduction of memory requirements. Furthermore, for characterizing vessel wall properties, a geometrical measure of aneurysmal wall deformation is obtained through the calculation of strain.

With the techniques proposed in these two chapters, we expect to be able to deal with situations of either focusing on the morphology at specific time instants, or to concentrate on the assessment of the whole motion pattern. Currently we are more interested in understanding the entire motion over the cardiac cycle. The next step would be to demonstrate the feasibility of applying this techniques to patient data, which is presented in Chapter 4. The study estimates and quantifies cerebral aneurysm and vascular wall motion from 3DRA and DSA images. The two

image registration techniques used were the 3D+t technique in Chapter 4 and a 2D+t technique [74]. Wall motion estimates from both modalities are compared to investigate the level of agreement between the motion estimations by the two methods both in terms of their amplitude and their temporal evolution over the cardiac cycle.

Each chapter is self-contained as appeared in the journal publication or submission under review; therefore, some of the basic concepts might appear in various chapters of the thesis.

2

Morphodynamic Analysis of Cerebral Aneurysm Pulsation from Time-Resolved Rotational Angiography

This chapter presents a technique to estimate and model patient-specific pulsatility of cerebral aneurysms over one cardiac cycle, using 3DRA acquisitions. Aneurysm pulsation is modeled as a time varying *B*-spline tensor field representing the deformation applied to a reference volume image, thus producing the instantaneous morphology at each time point in the cardiac cycle. The estimated deformation is obtained by matching multiple simulated projections of the deforming volume to their corresponding original projections. A weighting scheme is introduced to account for the relevance of each original projection for the selected time point. The wide coverage of the projections, together with the weighting scheme, ensures motion consistency in all directions. The technique has been tested on digital and physical phantoms that are realistic and clinically relevant in terms of geometry, pulsation and imaging conditions. Results from digital phantom experiments demonstrate that the proposed technique is able to recover subvoxel pulsation with an error lower than 10% of the maximum pulsation in most cases. The experiments with the physical phantom allowed demonstrating the feasibility of pulsation estimation as well as identifying different pulsation regions under clinical conditions.

The content of this chapter is based on the publication:

Chong Zhang, Maria-Cruz Villa-Uriol, Mathieu De Craene, Jose-Maria Pozo, Alejandro F. Frangi, Morphodynamic analysis of cerebral aneurysm pulsation from time-resolved rotational angiography, *IEEE Transactions on Medical Imaging*, 28(7): 1105-1116, 2009.

2.1 Introduction

Cerebral aneurysms are pathological enlargements of brain arteries commonly located at the circle of Willis [14]. When they rupture, spontaneous subarachnoid hemorrhage usually follows, causing high morbidity and mortality rates [14, 35]. Morphological characterization has been reported to provide indicators for monitoring the growth of intracranial aneurysms, as well as for correlating it with rupture events [26, 61, 79]. However, such techniques only consider static morphological information such as size and aspect ratio. On the other hand, it has been observed that aneurysms pulsate over the cardiac cycle [60, 114, 115] and rupture sites coincide with the areas of pulsation [29, 30, 37, 44]. If such correlation exists, the availability of a robust morphodynamic analysis tool has the potential of impacting treatment selection and preoperative planning of cerebral aneurysms. Nonetheless, a small motion range that can go below the image resolution makes the morphodynamic analysis practically challenging. Dempere *et al.* [18] proposed a motion estimation method from dynamic biplane DSA using 2D nonrigid image registration. Their recent work [75] extended this approach by postprocessing the recovered motion curve in the Fourier domain. Since DSA images are captured from a single point of view, motion was only partially estimated. Various techniques have been proposed for motion estimation and dynamic reconstruction. Most of them, e.g., dynamic CT [13], use a subset of projections belonging to the same motion state according to a time reference signal such as the ECG, and use this subset to reconstruct the object at that motion state. However, they are not tailored to wall motion estimation in cerebral aneurysms.

Movassaghi *et al.* [64] presented in-human 4D coronary artery reconstructions using an ECG-gated 3D tomographic reconstruction from projection images [81]. The promising results counterbalance the strong requirements in the imaging protocol and preprocessing. Schäfer *et al.* [88] reconstructed moving coronary arteries by shifting voxel positions according to a motion vector field. This method is only applicable to voxel driven cone-beam filtered back-projection (FBP) reconstruction approaches [20, 23] with an *a priori* known motion model. To perform gated reconstruction, the authors introduced a weighting factor into the FBP formulation according to the cardiac phase of the projections. Unfortunately, streak artifacts associated to FBP algorithms were not completely eliminated.

Blondel *et al.* [9, 10] computed a 4D B-spline deformation field of coronary arteries. A static 3D centerline model reconstructed at one cardiac phase was used to fit all projection images. Nonetheless, the centerline model is not suitable for aneurysm geometries in providing local deformation. Zeng *et al.* [126] also estimated 4D thorax respiratory motion during one CBCT acquisition using B-spline deformation. The need for two acquisitions (the reference CT and the CBCT projections) does not only increase patient exposure to radiation, but also might lead to misinterpret intrinsic organ motion as respiratory motion.

Several approaches were proposed for performing 2D motion correction and then reconstruct the 3D image from the motion-compensated 2D projections [27, 77]. They have been successfully applied to coronary artery or stent reconstruction. However,

we aim at recovering the 3D motion instead of removing it from the 2D projections. Furthermore, neither constraining motion to be affine [77] nor using the centerline model [27] are suitable options for the analysis of aneurysms. We therefore propose to model the aneurysm pulsation in the 3D space rather than in the space of the individual 2D projections.

In this chapter, the presented methodology models cerebral aneurysm pulsation as a time varying B-spline tensor field. It is applied to a reference volumetric image to estimate the instantaneous deformation at any time point in the cardiac cycle. The optimal B-spline transformation is obtained by matching multiple simulated projections of the deforming volume to the corresponding original projections. The transformation continuity and smoothness not only preserves the image resolution of the 3DRA reference volume, but also enables to recover subvoxel pulsation. A weighting scheme is introduced to account for the relevance of each projection to the estimated time point. The wide coverage of the projections, together with the weighting scheme, ensures motion consistency in all directions. The use of only one standard acquisition performed during an endovascular treatment does not expose patient to additional radiation risk and facilitates its clinical take-up.

The subsequent sections are organized as follows: in Section 2.2, the proposed methodology is explained in detail. Section 2.3 shows the experiments carried out on various digital phantoms for the quantitative evaluation of our method. Section 2.4 reports the results obtained from physical phantoms, to demonstrate the feasibility of our method. Discussion and conclusions are summarized in Section 2.5 and 2.6, respectively.

2.2 Method

During a 3DRA acquisition, a rotational sequence of cone beam X-ray projections are first obtained and then used to reconstruct a 3D volumetric image. In addition, a physiological signal (e.g., ECG or blood pressure) synchronized to the projections can be recorded. Typically, more than 100 projections are obtained during 4 seconds, at constant time intervals and uniformly distributed over more than 200° along a circular trajectory. Thus, the vascular motion occurring during the acquisition is captured in the 2D projections. However, since only a single volume is reconstructed, it does not provide the 3D dynamic morphology.

The objective of our work is to retrieve the time-resolved morphology of the imaged region by combining the 3D volume, the projections and a synchronized physiological signal. First, according to the cardiac cycles in the physiological signal, the projections are reordered to build one normalized cardiac cycle containing all of them (*original projections*). This step is detailed in Section 2.2.1 (Fig. 2.1). Then, at each time point in the normalized cardiac cycle, a 3D-to-multiple-2D image registration procedure is performed (Fig. 2.2). During this step, the 3D volume (*reference volume*) is iteratively deformed (Section 2.2.2) to maximize the similarity (Section 2.2.4) between the original projections and their corresponding simulated projections. The simulated projections are calculated from the deformed volume through a ray casting process

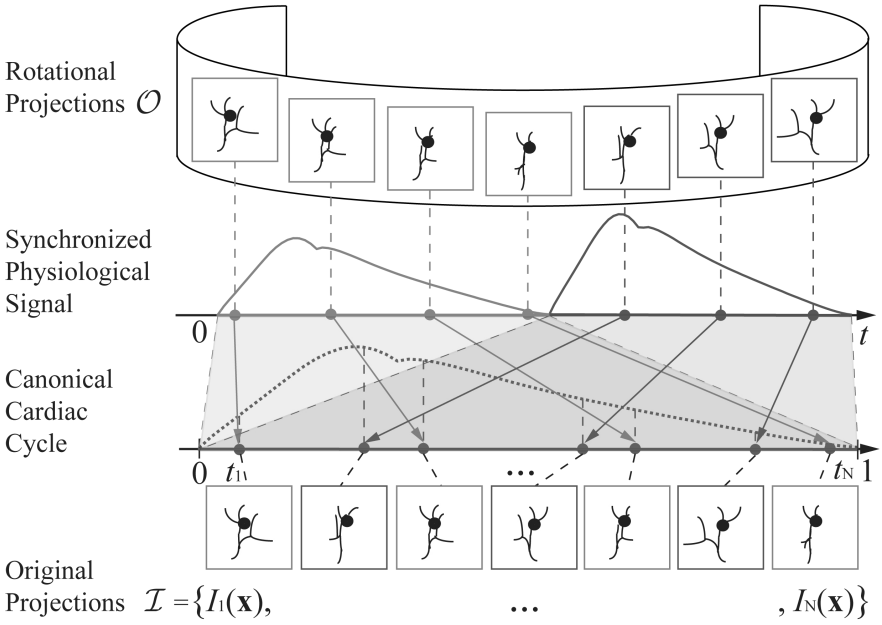

FIGURE 2.1: Creation of a canonical cardiac cycle according to the original rotational projections and the synchronized physiological signal.

(Section 2.2.3). The contribution to the similarity from each pair of original and simulated projections is weighted according to the temporal difference between the original projection and the current estimation.

2.2.1 Creation of a canonical cardiac cycle

Initially, the original projection sequence $\mathcal{O}$ of size N is used to reconstruct the reference volume. As shown in Fig. 2.1, a physiological signal is recorded synchronously with $\mathcal{O}$. Since in practice, the waveform of the physiological signal can vary from cycle to cycle, each cycle of this signal is extracted and its period is then linearly normalized to a time interval [0,1). All images in $\mathcal{O}$ are sorted by their normalized timestamps to build one *canonical cardiac cycle* as

$$\mathcal{I} = \{I_k(\mathbf{x}) \mid k = 1 \dots N \ , \ \mathbf{x} \in \mathcal{S}_k \subset \mathbb{R}^3\} \ ,$$

where the reordered image $I_k(\mathbf{x})$ lies on the corresponding projection plane $\mathcal{S}_k$, and is located within the canonical cardiac cycle at time t_k,

$$0 \leq t_1 \leq \dots \leq t_k \leq \dots \leq t_N < 1.$$

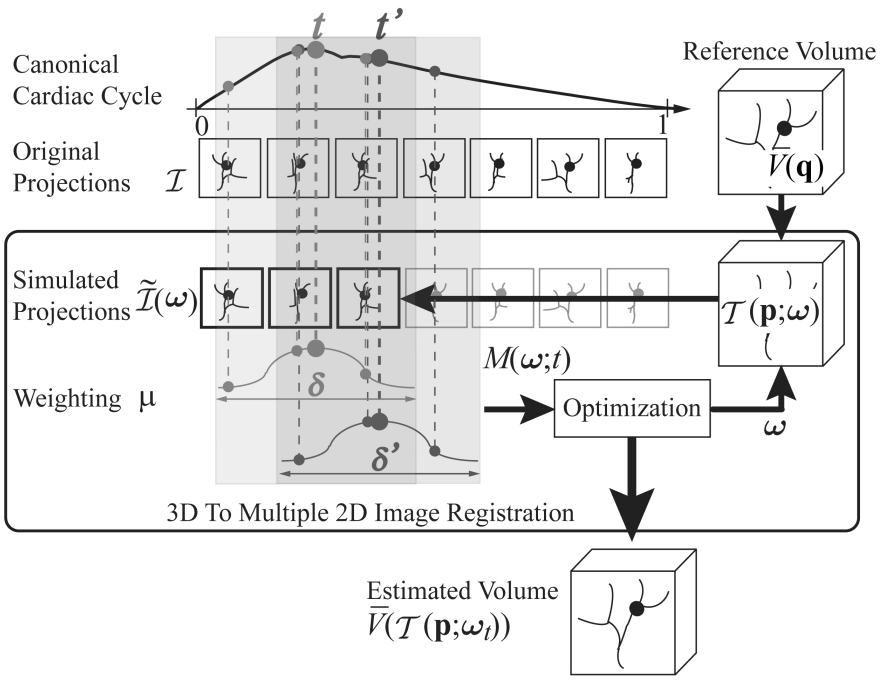

Figure 2.2: The 3D-to-multiple-2D image registration procedure for the canonical cardiac cycle. Two weighting windows are shown to illustrate the weighting scheme at two estimated time points, t and t'.

2.2.2 Deformation model

The motion at a given instant of time t is represented as a deformed reference volume $\overline{V}$:

$$\widetilde{V}(\mathbf{p};t) = \overline{V}(\mathcal{T}(\mathbf{p};\boldsymbol{\omega}_t)),$$

where the transformation $\mathcal{T}\colon \mathbb{R}^3 \mapsto \mathbb{R}^3$ maps a point $\mathbf{p}$ in $\widetilde{V}(\mathbf{p})$ to the point $\mathbf{q}$ in $\overline{V}(\mathbf{q})$, $\boldsymbol{\omega}_t$ denotes the time-varying transformation parameters at t. We have chosen a B-spline based transformation [47, 85], because it is not only smooth and continuous but also computationally efficient due to the local control of the basis functions. The transformation for any set of parameters $\boldsymbol{\omega}$ is given by

$$\mathcal{T}(\mathbf{p};\boldsymbol{\omega}) = \mathbf{p} + \sum_{\mathbf{c}} B\left(\frac{\mathbf{p}-\mathbf{p_c}}{\boldsymbol{\Delta}_\mathbf{c}}\right)\boldsymbol{\omega}_\mathbf{c}, \tag{2.1}$$

where $B(\cdot)$ is the 3D tensor product of 1D cubic B-spline basis functions, defined on a sparse grid of control points $\mathbf{p_c}$, being $\mathbf{c}$ the index of the control points, and $\boldsymbol{\Delta}_\mathbf{c}$ the width of the functions. Because of these short basis functions with limited support,

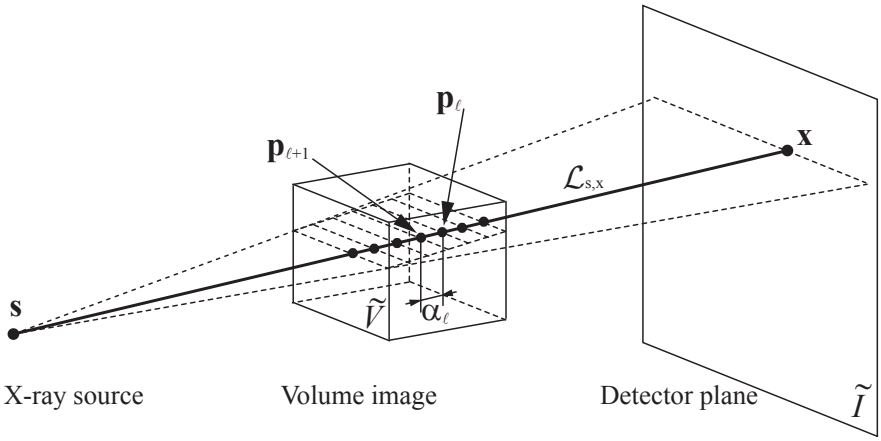

FIGURE 2.3: Overview of the ray casting algorithm to compute the simulated projection $\tilde{I}(\mathbf{x})$.

the B-spline transformation can only represent a subset of all possible deformation fields [47]. However, this limitation of the basis functions also provides an implicit regularization of the transformation.

2.2.3 Generation of simulated projections

In this chapter, a simulated projection $\tilde{I}(\mathbf{x})$ is calculated from $\widetilde{V}(\mathbf{p})$ through a ray casting procedure [38, 96] in order to approximate the X-ray attenuation imaging process [32]. Starting from each pixel $\mathbf{x}$ in the projection, a ray $\mathcal{L}_{\mathbf{s},\mathbf{x}}$ is casted through the volume to meet the X-ray source point $\mathbf{s}$ (Fig. 2.3). The pixel intensity of $\tilde{I}(\mathbf{x})$ is then defined as the integral of the volume intensities $\widetilde{V}(\boldsymbol{\gamma})$ for every point $\boldsymbol{\gamma}$ lying on $\mathcal{L}_{\mathbf{s},\mathbf{x}}$:

$$\tilde{I}(\mathbf{x}) = \int_{\mathcal{L}_{\mathbf{s},\mathbf{x}}} \widetilde{V}(\boldsymbol{\gamma}) d\boldsymbol{\gamma} \approx \sum_{\ell} \alpha_\ell \, \widetilde{V}(\mathbf{p}_\ell) \tag{2.2}$$

where ℓ is the index of the sampled voxel points $\mathbf{p}_\ell$ along $\mathcal{L}_{\mathbf{s},\mathbf{x}}$, and α_ℓ the sampling weight, the distance between two consecutively sampled points $\mathbf{p}_\ell$ and $\mathbf{p}_{\ell+1}$. On each of the original projection planes $\mathcal{S}_k$, such a simulated projection can be generated by ray casting $\widetilde{V}(\mathbf{p}; t)$. The sequence of simulated projections is denoted as:

$$\tilde{\mathcal{I}} = \{\tilde{I}_k(\mathbf{x}) \mid k = 1 \dots N \ , \ \mathbf{x} \in \mathcal{S}_k \subset \mathbb{R}^3\} \ .$$

$\tilde{\mathcal{I}}$ reflects the morphology at time t from various projection views. Note that for each image $\tilde{I}_k(\mathbf{x})$, a valid ray region $\mathcal{R}_k$ is defined so that only those rays intersecting the volume are evaluated. For the rest of the pixels, their intensity value is set to zero.

2.2.4 Similarity measures

During the registration process at an instant of time t in the canonical cardiac cycle, the corresponding deformation parameters $\boldsymbol{\omega}_t$ are determined by matching the simulated projections to the original projections:

$$\boldsymbol{\omega}_t = \underset{\boldsymbol{\omega}}{\operatorname{argmin}} \Big\{ M(\boldsymbol{\omega}; t) = \sum_k \mu(t, t_k)\, D\big(\tilde{I}_k(\boldsymbol{\omega}), I_k\big) \Big\}, \tag{2.3}$$

where $M(\cdot)$ is the metric that sums up a weighted similarity measure between each original and simulated projection pair, $D\big(\cdot\big)$ the similarity metric, and $\mu(\cdot)$ the weighting factor accounting for the temporal proximity between two projections.

2.2.4.1 Similarity measures between two images

As simulated projections are approximations of the original projections, the image intensity ranges are different, therefore mutual information has been used in our work:

$$D\big(\tilde{I}_k(\boldsymbol{\omega}), I_k\big) = -\sum_u \sum_v p(u, v) \log \frac{p(u, v)}{p(u)p(v)}, \tag{2.4}$$

where $p(u)$ and $p(v)$ are respectively the marginal probability distributions of the intensity values of I_k and $\tilde{I}_k$, and $p(u, v)$ the joint probability distributions of these two images. Here u, $0{<}u{<}H$ and v, $0{<}v{<}\tilde{H}$ are the indices of uniformly sized histogram bins along the respective dimensions of the joint histogram.

Histograms are approximated using Parzen windows for the probability calculation [58, 100]. Let $\beta^{(0)}$ and $\beta^{(3)}$ be a zero-order and a cubic B-spline Parzen windows. The joint histogram is then given by

$$p(u, v) = \hat{\alpha} \sum_{\mathbf{x} \in \mathcal{R}_k} \beta^{(0)}\Big(u - \frac{I_k(\mathbf{x}) - i_k^\circ}{\Delta h}\Big) \cdot \beta^{(3)}\Big(v - \frac{\tilde{I}_k(\mathbf{x}; \boldsymbol{\omega}) - \tilde{i}_k^\circ}{\Delta \tilde{h}}\Big),$$

where $\hat{\alpha}$ is a normalization factor that ensures $\sum p(u, v){=}1$, i_k° and $\tilde{i}_k^\circ$ the minimum intensity values, and Δh and $\Delta \tilde{h}$ the intensity bin sizes. The marginal histogram of $\tilde{I}_k$ is computed as

$$p(v) = \sum_u p(u, v).$$

As I_k is independent from the transformation, its marginal probability can be precomputed as:

$$p(u) = \hat{\alpha} \sum_{\mathbf{x} \in \mathcal{R}_k} \beta^{(0)}\Big(u - \frac{I_k(\mathbf{x}) - i_k^\circ}{\Delta h}\Big).$$

2.2.4.2 Weighting temporal proximity

For the kth projection plane $\mathcal{S}_k$, I_k is acquired at t_k, whereas $\tilde{I}_k(\boldsymbol{\omega})$ represents the estimated motion state at t. If t_k is sufficiently close to t, the differences between

the motion state at these two time points should be small, implying the two images should be very similar. Otherwise, large differences should be expected. Hence, I_k should have a reduced impact on determining $\boldsymbol{\omega}$. Thus, the weighting factor $\mu(t, t_k)$ is a symmetric operator centered at t and should satisfy:

$$\left|t - t_1\right| > \left|t - t_2\right| \quad \Rightarrow \quad \mu(t, t_1) < \mu(t, t_2).$$

In this chapter, a cosine power function is used [56]:

$$\mu(t, t_k) = \begin{cases} \cos^{\lambda}\left(\pi \dfrac{t - t_k}{\delta}\right) & , \quad \text{if } |t_k - t| < \dfrac{\delta}{2} \\ 0 & , \quad \text{otherwise.} \end{cases}$$

This function can be shaped easily by the modification of the exponent. With $0<\lambda\leq 2$, very small values at the window boundaries are avoided. For our experiments, $\lambda=2$ was used. In addition, the finite support of this function window width δ reduces the computation only to the projections within the time interval $[t - \delta/2, t + \delta/2]$.

By combining information from the projections at adjacent time points, motion can be estimated at any time point within the cardiac cycle. Note that it also limits the level of detail of the temporal evolution of the estimated motion due to the smoothing effect introduced by interpolating the projections. Therefore, the value of δ should be chosen as a trade-off between the local pulsation variation and the number of projections available within this time interval. However, as pulsation is not known *a priori*, a fixed window width can be chosen for all the selected time points over the cardiac cycle. As shown by our experiments, the presented weighting scheme enforces continuity of the recovered deformation in time, and adequately accommodates for heart rate variations.

2.2.5 Optimization strategy

The success of image registration depends on the optimization of the image matching metric. A wide range of optimization methods can be considered to minimize the metric in (3.3). Since the number of parameters characterizing the transformation is large, and the metric is explicitly differentiable, gradient-based methods are a natural choice. The L-BFGS-B method [133] is used, which searches the optimum according to the gradient and a low-rank approximation of the Hessian of the metric. The analytical computation of the metric gradient is detailed in Appendix.

2.3 Digital phantom experiments

Before analyzing patient data, our method has been validated using digitally simulated aneurysm phantom models, allowing to study the influence of various factors on its performance. Geometry, pulsation, and imaging conditions were simulated to be realistic and clinically relevant. The modeling parameters are summarized in Table 2.3.

Table 2.1: Design parameters for digital phantom studies

Parameters	Type I	Type II
Dome shape	Irregular	Spherical
Dome diameter (mm)	8-12	10
Vessel shape	Toroidal	Cylindrical
Vessel diameter (mm)	4	4
Pulsation waveform	Sinusoidal	Physiological
Pulsation frequency (bpm)	∼90	∼60
Pulsation amplitude range (mm)	0.08-0.48	0.41-0.69
Frame rate (Hz)	25	30
Projection pixel size (mm^2)	0.16^2 or 0.31^2	0.16^2 or 0.31^2
Voxel size (mm^3)	0.3^3	0.3^3

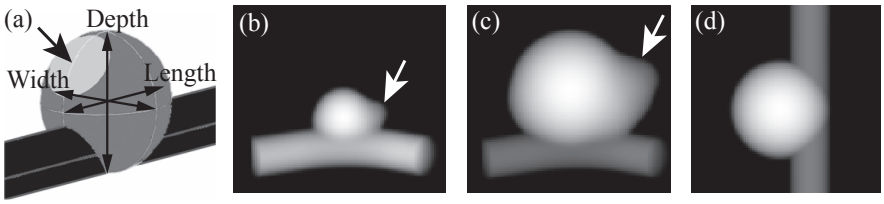

Figure 2.4: (a) An illustration of measures referred to as depth, width, and length. Simulated projections of (b, c) Type I and (d) Type II phantoms. *Arrows* indicate bleb regions.

2.3.1 Experimental design

2.3.1.1 Geometry

Two types of phantoms were created as smooth combinations of primitive geometries such as spheres, cylinders, and tori of different sizes (Fig. 2.4). Type I phantoms presented an emerging bleb on an irregularly shaped dome attached to a toroidal vessel of 4 mm in diameter, whereas Type II phantoms consisted of a 10-mm diameter spherical dome attached to a 4-mm diameter cylindrical vessel. For each phantom, a sequence of geometries was generated to represent the ground-truth pulsation in several cardiac cycles. The phantom geometry smoothly changed according to a predefined pulsation waveform and was sampled at a finite number of time points.

2.3.1.2 Pulsation

For Type I phantoms, periodic sinusoidal waveforms were used to create wall displacements, e.g., Fig. 2.5(a). For Type II phantoms, pulsation was generated from a parametric biomechanical model according to a pressure waveform, the mechanical properties of the wall, and the geometry. In this model, the fluid-dynamic equations describing the haemodynamics inside the vessel are coupled with the structural equations describing the surface pulsation. The equations were solved by finite element analysis using COMSOL Multiphysics V3.4 (COMSOL Inc., Burlington, MA, USA). Details of the modeling can be found in [4]. To the best of our knowledge, *in vivo* measurements of such properties close to cerebral aneurysms are not available in the literature. Therefore, literature values from arteries belonging to the circle of Willis were set to the dome [3, 102]: a thickness of 0.050cm, a tissue elastic modulus of 0.8MPa, and a hypertensive blood pressure range of 100-170 mmHg. Bleb regions (Fig. 2.4) were assigned to have a slightly higher pulsatility, whereas vessel regions were set to be wall compliant. Pulsation amplitude range (0.08-0.69 mm) was less than 7% of the dome diameter, consistent with literature studies: 6% in [52], 0.7 mm (14%) in [102], 0.2-0.35 mm (2-3%) in [108] and 0.24-0.25 mm (3.8-4.5%) of arterial wall motion in [117]. Periodic (WP1) and aperiodic (WP2) pulsation waveforms were considered, and an example is shown in Fig. 2.5(b). For WP2, two cycles, CP1 and CP2, different in amplitude and period, are combined alternatively to create an aperiodic waveform.

2.3.1.3 Simulated volume and projections

To recreate realistic 3DRA imaging, a flat panel system Allura Xper FD20 (Philips Healthcare, Best, The Netherlands) was chosen as a reference. First, a sequence of volume images was generated from the sequence of ground-truth geometries. Voxel intensities were obtained as a function of the signed distance from the voxel to the object surface, usually known as *distance transform*. The result is a binary image with a constant value inside the object and another value outside, but with a blurred band of 0.5 mm around the surface. Each image has approximately 50^3 cubic voxels of 0.3 mm each side. Then, this volume sequence was used to simulate the original projections as described in Section 2.2.3. The physical size of the projection images is $(160\ \text{mm})^2$, being the X-ray source to detector distance and source to isocenter distance 1195 mm and 810 mm, respectively. The rotational acquisition captures more than 100 projections uniformly distributed along a circular trajectory of over 200° at a frame rate of 25-30 Hz. They were simulated with two sets of image resolutions: 1024^2 and 512^2 pixels.

2.3.1.4 Simulated temporal information

The ground-truth volumes and the original projections had two types of temporal relations. Under *ideal conditions*, the phantom pulsates periodically and is projected at exactly the same pulsation states in every cycle. In Fig. 2.5(a), projections are captured during a period comprising 7 cardiac cycles, e.g., the seventh projection

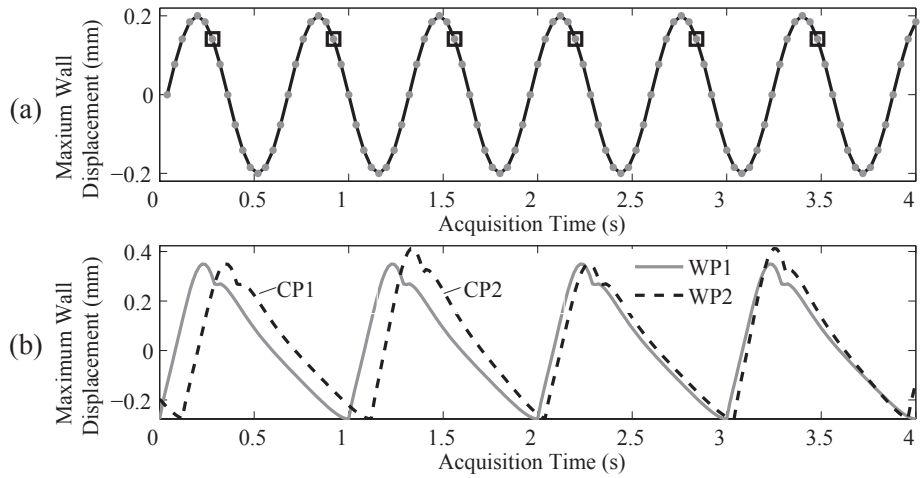

Figure 2.5: Pulsation waveforms expressed as maximum wall displacement. (a) Sinusoidal waveform under ideal conditions, with pulsation amplitude range of 4% of the dome diameter for a 10-mm Type I phantom. Images are captured and repeated at the same time for each cycle, e.g., the seventh images correspond to exactly the same pulsation state (*boxes*); (b) Physiological waveform under: ideal conditions, WP1, and realistic conditions, WP2 (two cycle waveforms, CP1 and CP2, occurring alternatively).

(*boxes*) in each cardiac cycle always has the same timestamp in the canonical cardiac cycle, and therefore reflects the same phantom pulsation state. As a result the ground-truth pulsation in the canonical cardiac cycle is known, allowing to determine the motion estimation errors. Under *realistic conditions*, the phantoms experience cardiac cycle variations both in pulsation amplitude and frequency, such as in Fig. 2.5(b). Such slight variations are likely to happen, limiting our method to recover an averaged morphodynamic behavior due to the use of the weighting scheme.

2.3.2 Results

Once an aneurysm is located, physicians routinely perform manual measurements to evaluate the lesion extent and to plan the most suitable treatment. Typically, aneurysm dome diameters and volume are calculated. Hence, these two measures were chosen to quantify the global pulsation in our studies as well. Fig. 2.6 shows for both types of phantoms diameter and volume variations over time with respect to the reference volumes. Three diameters were measured as the main axes dimensions of the aneurysm, viz. dome depth, length and width, as shown in Fig. 2.4(a). Results indicate that the estimated temporal evolution of the dome volume is more accurate than that of the diameter. Such difference can be explained by a higher sensitivity of diameters to local errors in motion estimation which are less critical in global volume

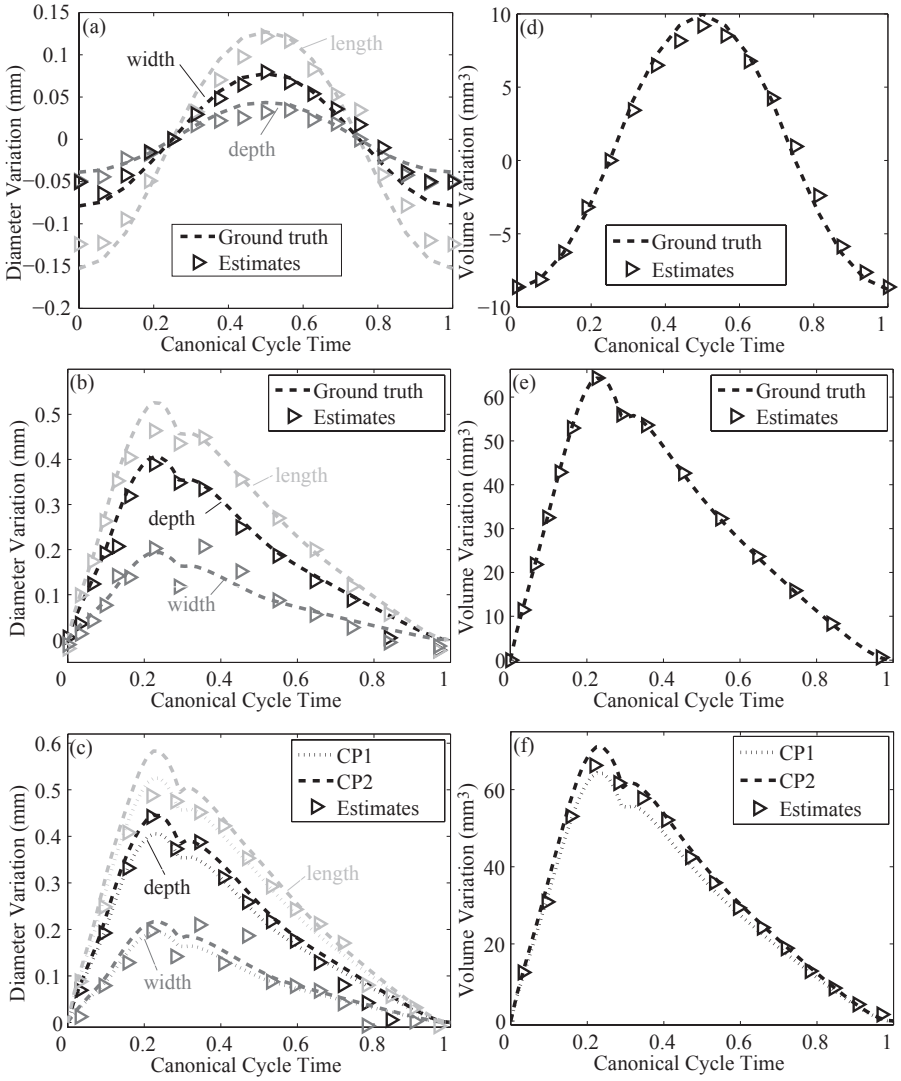

FIGURE 2.6: Instantaneous changes in diameter (*left*) and volume (*right*) measured over time: (a,d) Type I phantom; (b,e) Type II phantom with pulsation pattern WP1; (c,f) Type II phantom with pulsation pattern WP2, composed of two cycle waveforms CP1 and CP2, shown in Fig. 2.5(b).

estimates. Note that for Type II phantoms under realistic conditions (Fig. 2.6(c,f)), our method obtains an averaged approximation of the motion during the whole

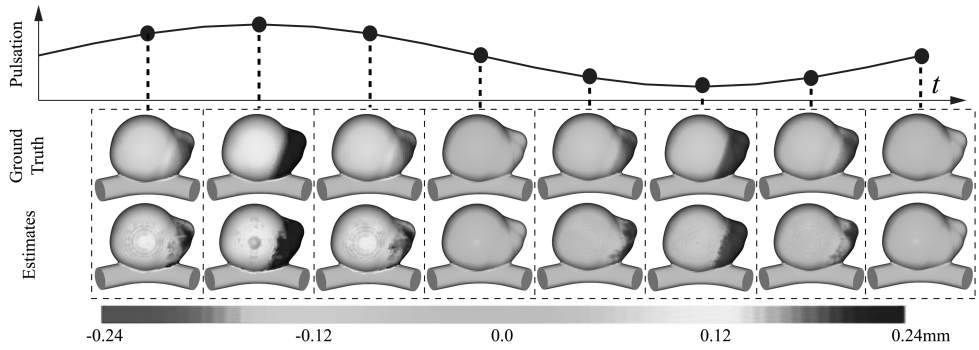

FIGURE 2.7: Instantaneous estimated pulsation amplitude distribution at 8 (*dots*) time points referenced to the ground truth pulsation curve. A 12-mm aneurysm with pulsation of 4% (0.48 mm). Ground truth (*top*) is compared to the results from our method (*bottom*). (color version on page C2)

acquisition.

In fact the pulsation amplitude is expected to change at different locations on the aneurysmal wall [18, 75], indicating weaker regions, which could potentially become rupture sites. In this chapter, the point-to-surface distance was used to approximate local pulsation amplitude. The geodesic active contour [15] segmentation algorithm was used to obtain the aneurysm surfaces. Fig. 2.7 shows for a Type I phantom with 4% pulsation of 12-mm dome (equivalent to a pulsation range of -0.24 to 0.24 mm), the color-coded estimated pulsation amplitude distribution for 8 selected time points in the canonical cycle. Ground-truth color maps indicate that the bleb experiences the largest wall displacements, being in agreement with our estimates. Note that in our experiments, the maximum pulsation amplitudes are smaller than the voxel size. Nonetheless, our method was able to estimate and recover it, mainly due to the transformation properties: continuity and smoothness.

The following experiment was performed to analyze the impact of the weighting window width δ, and to find a criterion of choosing the optimal δ. First, with a large δ, the blurring of larger pulsation variation regions is caused by the effect of averaging more projections. Second, with a smaller δ, less pulsation variation is considered resulting in a more precise estimation, but the less projections are provided, the more probable the partial pulsation estimation. Results for Type II phantoms under realistic conditions using various weighting window widths are reported in Fig. 2.8. With $\delta \leq 10\%$ in general our method is able to capture the pulsation. However, results with $\delta \leq 5\%$ better recover the two-peak pulsation waveform. Note that in our case, even for $\delta = 3.33\%$ there are in average 4 projections per weighting window. Therefore, in practice choosing the value of δ between 5-10% is a good choice, preserving the balance between local pulsation variation and the number of projections available

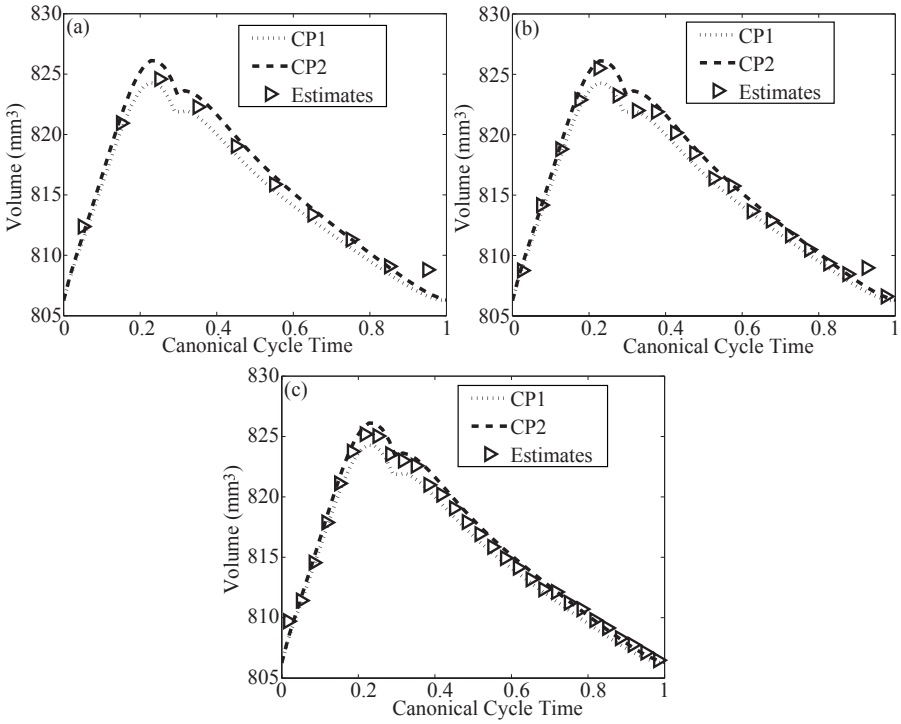

FIGURE 2.8: Instantaneous volume measured over time for Type II phantoms under realistic conditions using weighting window width δ equal to: (a) 10%, (b) 5%, and (c) 3.33% of the canonical cycle.

within this time interval. We chose δ=5% for the remaining experiments in this chapter.

Although ground truth and the estimates are in good qualitative agreement, a more comprehensively quantitative comparison is necessary. Thus, a relative estimation error at time point t in the canonical cardiac cycle is defined as:

$$e(t) = 100 \times \left| \frac{m_r(t) - m_g(t)}{\hat{m}_g} \right|, \tag{2.5}$$

where m_g and m_r represent the pulsation measurements (e.g., volume), $m_g(t)$ the ground-truth measurement at t, $m_r(t)$ the corresponding estimated measurement, and $\hat{m}_g$ the range of variation for $m_g(t)$ over the canonical cycle. As a result, the error e expresses the estimation error as a percentage of the pulsation range.

Fig. 2.9 summarizes the relative error in volume changes, e_V, in boxplots [59] to represent the results for 12 cases of Type I phantoms with diameter 8, 10, and 12 mm, each having maximum pulsation amplitudes of 1, 2, 3, and 4%, respectively. In

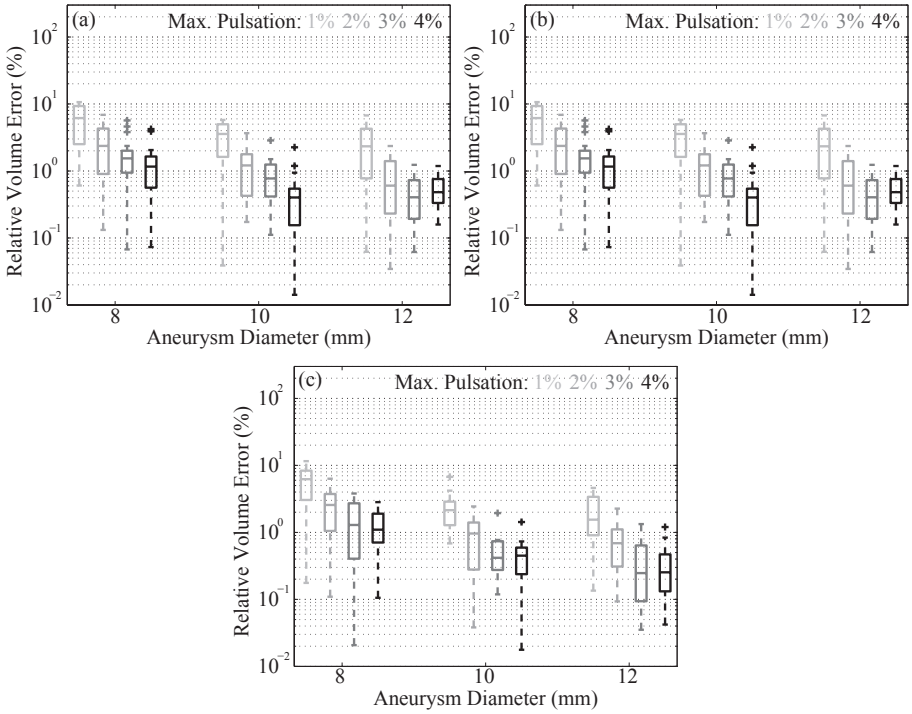

Figure 2.9: Boxplots of the relative volume error e_V at 16 time points over the canonical cardiac cycle under ideal conditions, for Type I phantoms with diameter 8, 10, and 12 mm, and pulsation amplitude range with 1, 2, 3, and 4% of the dome diameter. (a) B-spline control points: 5^3, pixel size (mm^2): 0.31^2. (b) B-spline control points: 8^3, pixel size (mm^2): 0.31^2. (c) B-spline control points: 8^3, pixel size (mm^2): 0.16^2.

all cases, our method was applied to 16 evenly sampled time points using projection image resolutions of $(0.31 \text{ mm})^2$ or $(0.16 \text{ mm})^2$ and a number of B-spline grid control points of 5^3 or 8^3 in a region of about $(15 \text{ mm})^3$. In most cases, the error is less than 10% of the pulsation range. And the larger and the more pulsating is the aneurysm, the smaller the recovered relative volume error. Furthermore, Fig. 2.9(a) and (b) illustrate that the benefit from having more control points is not significant. A possible explanation is that, as the fine grid increases dramatically the number of optimization parameters, the method becomes more sensitive to the noise present in the data. In our studies, the optimization was not able to handle more than 10 control points per axis, 6591 estimated parameters in total. On the other hand, because of the sparse derivative matrix described in Appendix, the computational time does not increase significantly with a larger number of control points. Fig. 2.9(b) and (c) suggest that the resolution of the original and simulated projections can be reduced

without significantly degrading the accuracy of the final estimation. Similar findings have been mentioned in [118]. For this reason, for the remaining experiments with digital phantoms, projection image resolution was fixed to $(0.31\text{ mm})^2$ and a number of B-spline grid control points of 8^3 in a region of about $(15\text{ mm})^3$.

2.3.3 Discussion

As the expected cerebral aneurysmal motion range is very small, e.g., subvoxel, accurately estimating such dynamic morphology is challenging. For this reason, in this section we evaluate the impact of different factors that might affect the motion estimation accuracy.

2.3.3.1 Effects of head movement

Although patients are usually sedated during the acquisition, slight head movements might happen. In our work, head movements were simulated when acquiring each original projection, by adding a 4-degree-of-freedom rigid movement, i.e., 3 translations and a rotation along the gantry trajectory. In the first set of experiments, for each original projection, randomly generated translations within the range of the maximum pulsation amplitude and a rotation within 0.1° were added to the reference volume before projecting it. Fig. 2.10(a) shows the relative volume errors using the same set of phantoms as used in Fig. 2.9. Results suggest that although slight head movements degrade the performance, the accuracy of the method is still satisfactory as most errors are bounded and below 10%. In [24], head movements are observed to be less than 0.5 mm during the first 5 minutes. In the case of a 3DRA acquisition, patient is positioned in same manner but for a shorter time, in a second set of movement simulations, the randomly generated translations and rotation ranges were set to be 0.25 mm and 0.1°, respectively. As shown in Fig. 2.10(b), the error raises dramatically under this condition, since the introduced head movements can be even larger than the pulsation. Therefore it is necessary to guarantee immobility of the patient.

2.3.3.2 Effects of scattering and noise

X-ray projections are measured from photon counts, which are always degraded by scattered photons, and quantum noise dominated by the Poisson effect. In order to study their influence, scattering and noise are simulated and added to the scattering-noise-free projections. Scattering is modeled using convolution filtering to blur the projections. A 2D Gaussian function with a full-width at half-maximum (FWHM) of 75 pixels (i.e., 23.4 mm) and a scatter-to-primary ratio (SPR) of 10% was convolved with the projections [51]. Then quantum noise is simulated using a Box-Muller approximation of a Gaussian distribution, which is representative as the number of photons emitted is sufficiently high [119]. The resultant Gaussian noise has a zero mean and standard deviation of 2.5% of the maximum value of the scattered image signal [121]. In practice, the SPR and the amount of noise might be even larger. Results are shown in Fig. 2.10(c). The performance is slightly degraded by scattering

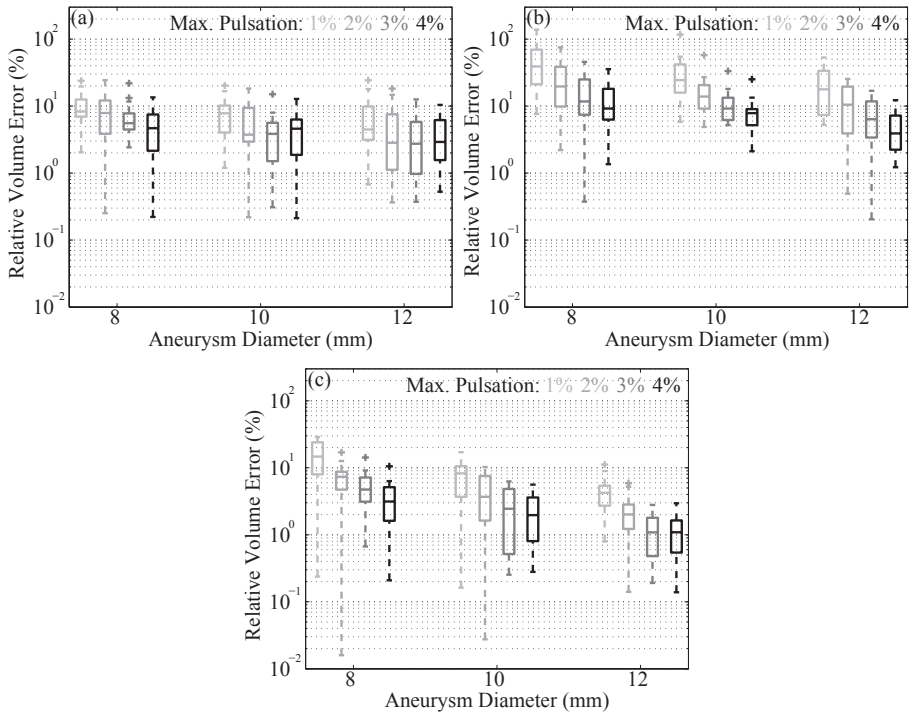

Figure 2.10: Boxplots of the relative volume error e_V at 16 time points over the canonical cardiac cycle for the same phantoms in Fig. 2.9 using: (a) randomly added translations and rotation, within the maximum pulsation amplitude and 0.1°, (b) randomly added translations and rotation, within 0.25 mm and 0.1°, and (c) SPR=10% plus a Gaussian noise with zero mean and standard deviation of 2.5% of the maximum value of the scattered image signal.

and noise, but the error is still less than 10% in most of the cases. Cases with higher pulsation and larger size are less affected, thus providing a similar error range as obtained from scattering-noise-free experiments shown in Fig. 2.9(b).

2.3.3.3 Effects of reference volume selection

In clinical practice, although 3DRA images are filtered to reduce the presence of reconstruction artifacts, they are not completely removed, as shown in Fig. 2.11. Meanwhile, when reconstructed from the projections with changing morphology, the reference volume is expected to represent a smoothly averaged state. Three sets of experiments were performed to study the possible influence by different choices of the reference volume. In the first set, the ground-truth volume at the averaged

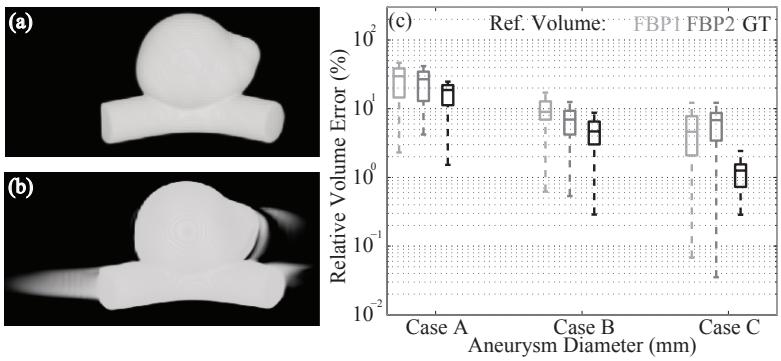

FIGURE 2.11: (a) The ground-truth volume at the averaged state. (b) Volume reconstructed using FBP reconstruction algorithm, showing some undesired artifacts. (c) Boxplots of the relative volume error e_V at 16 time points over the canonical cardiac cycle using three types of reference volumes: FBP1, FBP2, and GT: Case A, diameter 8 mm with 1% pulsation; Case B, 10 mm with 3%, and Case C, 12 mm with 3%.

state was used; in the second set, the reference volume was reconstructed from the simulated projections of the pulsating phantom, using the FBP algorithm [23]; and in the third set, the reference volume was obtained the same way as the second set, but the phantom is not pulsating. We denote these three sets as GT, FBP1, and FBP2, respectively, for the simplification of explanation. Three Type I phantom cases were tested: diameter 8 mm with 1% pulsation (Case A), 10 mm with 3% pulsation (Case B), and 12 mm with 3% pulsation (Case C). The estimated relative volume errors are shown in Fig. 2.11(c). Larger errors were obtained when using reference volumes from the FBP reconstruction, whereas results were not substantially different by using FBP1 or FBP2. However, the error variations introduced by different sizes and pulsation amplitudes are not significant, either. This suggests that the artifacts present in the FBP reconstructions introduce a nonnegligible amount of error in our estimation.

2.3.3.4 Effects of adding realistic background

Besides the studied aneurysm, patient images also contain other attenuated vessels, air, bones, and soft tissues. In order to study their influence, we have blended Type I digital pulsating phantoms into a real patient dataset. Once each phantom was placed in the patient image, the voxels corresponding to aneurysm and vessel were set to a representative vessel intensity value. An example of the blended projections is shown in Fig. 2.12(a). Fig. 2.12(b) shows the relative volume errors using such simulation dataset. Compared with Fig. 2.9(b), the errors are in general larger, and the error variations introduced by sizes and pulsation amplitudes are smaller. Nonetheless, the results indicate that adding the realistic background into the digital

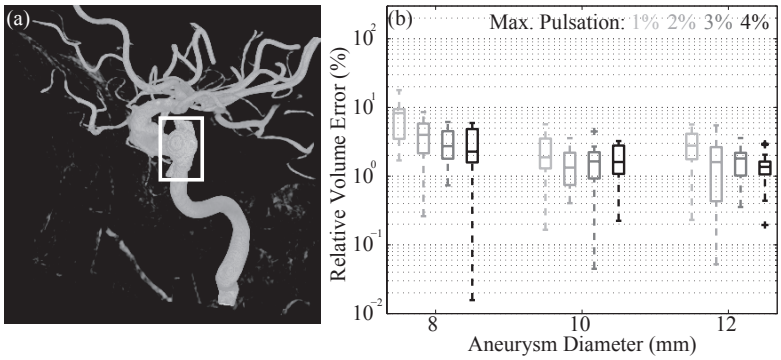

Figure 2.12: (a) A digital phantom blended with realistic background (white frame indicating the aneurysm phantom). (b) Boxplots of the relative volume error e_V at 16 time points over the canonical cardiac cycle for such dataset.

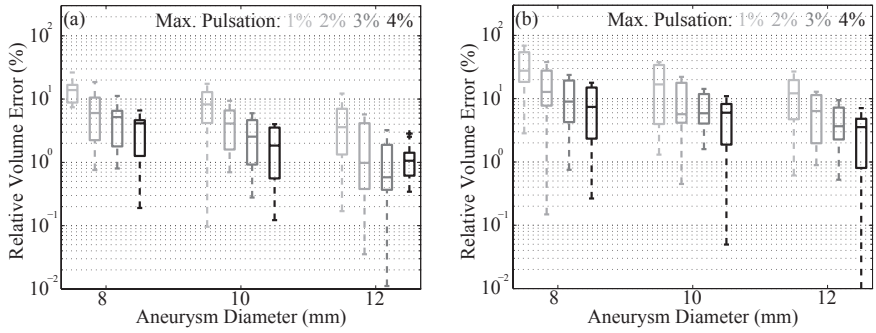

Figure 2.13: Boxplots of the relative volume error e_V at 16 time points over the canonical cardiac cycle for the same phantoms as used in Fig. 2.9 but with the downsampling factor: (a) df=2; (b) df=3.

phantom experiments does not significantly degrade the performance, as the errors in most cases are below 10%.

2.3.3.5 Effects of angular resolution of the projections

It is found that the accuracy and robustness of a 3D-to-multiple-2D image registration method do not depend solely on the method itself but also on the number of projections [101]. We have investigated this factor by downsampling the number of original projections and using only the subsampled set. The downsampling factors (df) used in our experiments were 2 and 3. As this factor indeed determines the density

TABLE 2.2: Design parameters for physical phantom studies

Parameters	Values
Dome shape	Spherical
Dome diameter (mm)	10
Vessel shape	Cylindrical
Vessel diameter (mm)	4
Pulsation waveform	Pseudo physiological
Pulsation frequency (bpm)	90
Pulsation amplitude range (mm)	unknown
Frame rate (Hz)	30
Projection pixel size (mm^2)	0.155^2
Voxel size (mm^3)	0.295^3

of the projections along the rotational gantry trajectory, we refer to it as angular resolution of the projections. Fig. 2.13 summarizes the relative volume errors on these experiments for 12 cases of Type I phantoms. As can be seen from Fig. 2.13(a) and (b), reducing the number of projections by a factor of 2 slightly increases the error. But it remains below 10% in most of the cases. Fig. 2.13(c) shows that the errors are mostly below 20% when reducing the number of projections by a factor of 3. These experiments indicate that the performance increases when the angular resolution of the projections is higher.

2.4 Physical phantom experiments

The method has also been tested in a real clinical environment, using a nonrigid silicone phantom under pulsatile flow conditions. One obstacle is to evaluate the accuracy due to the absence of ground truth information. Results are evaluated firstly by visual inspection comparing the simulated projections from the estimated volumes to the corresponding original projections. And secondly, they are compared to Doppler ultrasound flow waveforms obtained in the experimental setup.

2.4.1 Data acquisition

A silicone side-wall aneurysm phantom was used (Fig. 2.14). It has a 10-mm-diameter spherical aneurysm dome and a 4-mm-diameter cylindrical vessel. The phantom was water-filled and connected to a customized pulsatile pump, a continuous flow pump (Elastrat, Geneva, Switzerland), and a liquid tank to create a continuous and pulsatile fluid circulation. The box containing the phantom was also filled with water to simulate realistic X-ray attenuation. The pulsatile pump produced a human-

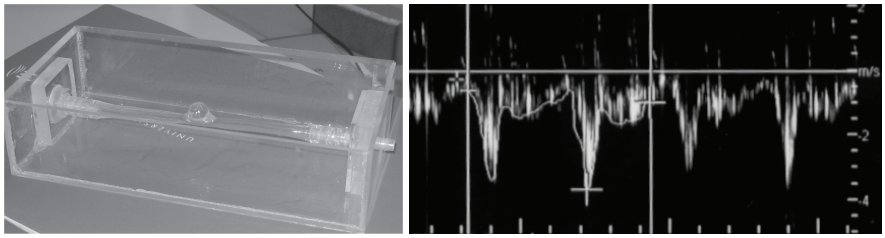

FIGURE 2.14: The silicone side-wall aneurysm phantom (*left*) and the Doppler ultrasound velocity waveform at the parent vessel inlet (*right*).

like pulsatile flow, as shown in Fig. 2.14. As a result, the phantom presented visible wall motion.

Experimental data were acquired using a flat panel system Allura Xper FD20 (Philips Healthcare, Best, The Netherlands). In total 121 rotational projection images were captured with a frame rate of 30 Hz, over 200° along the gantry trajectory. Constant injection of contrast agent Iomeron 400 (Bracco Imaging SpA, Milan, Italy) was performed during the acquisition at a rate of 3 mL/s. X-ray source and detector positions were recorded for each projection, allowing the spatial relationship between the reconstructed reference volume and each projection to be known. The reference volume has 256^3 cubic voxels of 0.295 mm each side. The original projections have a dimension of 1024^2 with pixel size of $(0.155\ \text{mm})^2$. Table 2.2 summarizes the parameters of the phantom geometry, pulsation, and imaging conditions.

2.4.2 Experiments and results

A number of *B*-spline control points (8×8×8) were set to a region of about $(11\ \text{mm})^3$ in size, containing the aneurysm dome. The pulsatile pump signal frequency was set to 90 bpm, and the acquisition frame rate was 30 Hz. Thus during each pulsation cycle, projections were acquired at the same 20 instants of time within the cycle, which means the experiments were performed under ideal conditions. This allows validating the results at each ground-truth pulsation state by comparing the projections of the estimated 3D volumes to the corresponding original ones.

Fig. 2.15(a) and (d) show from two viewpoints the X-ray projections of one acquisition under pulsatile flow conditions. In (b) and (e), the regions of checkerboard images presenting the aneurysm dome are shown, where each checkerboard image is composed of the X-ray projection and its corresponding simulated projection of the reference volume. A clear mismatch on both dome and vessel boundaries can be observed. Whereas in (c) and (f), similar checkerboard images are shown from the estimated volumes. Such checkerboard comparison shows that our method was able to correct the misalignment caused by pulsation.

Fig. 2.16(a) shows the estimated volume variations. Similar results were ob-

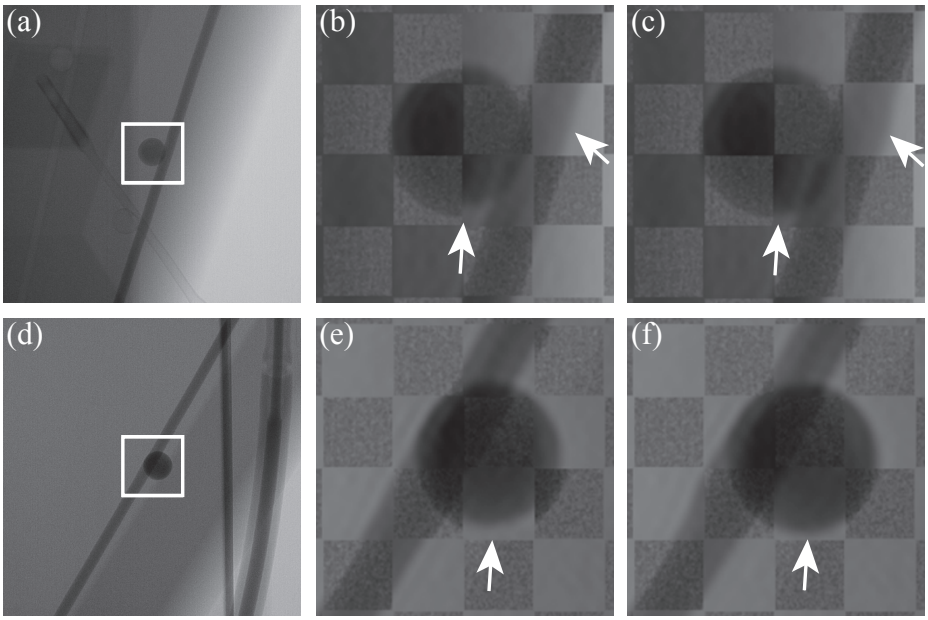

FIGURE 2.15: (a,d) X-ray projection images, each with a white frame indicating the regions shown in (b,c) and (e,f), respectively. Checkerboard comparisons of the original and simulated projections: (b,e) before applying our method and (c,f) afterwards.

tained using two downsampling factors: df=1,2. This is in agreement with the digital phantom experiments, as shown in Section 2.3.3.5. Differences at the peak should be explained by the lack of information to constrain the deformation in certain directions. Along with the volume variations, the Doppler ultrasound velocity waveform measured at the aneurysm parent vessel inlet was also shown. It should be noted that, apart from the phase delay due to the coupling between the fluid flow and wall displacement [117], the velocity was not synchronized with the data acquisition, thus a waveform shift possibly exists. Nonetheless, the volume variation waveform qualitatively presents a similar pattern to the velocity waveform, which is in agreement with the findings in [52, 117]. An advantage of measuring volume is that, the global movements are not reflected in volume changes, resulting in only the deformation of the aneurysm phantom. Fig. 2.16(b) shows at four out of 20 estimated time points the instantaneous wall displacements with respect to the reference geometry. It can be observed that wall displacements are larger at the flow impingement area. In addition to dome expansion and contraction, the phantom experiences a tilting movement towards the flow direction as well.

Fig. 2.17 plots for each point on the segmented surface of the reference volume its color-coded pulsation amplitude range over the cardiac cycle, together with its

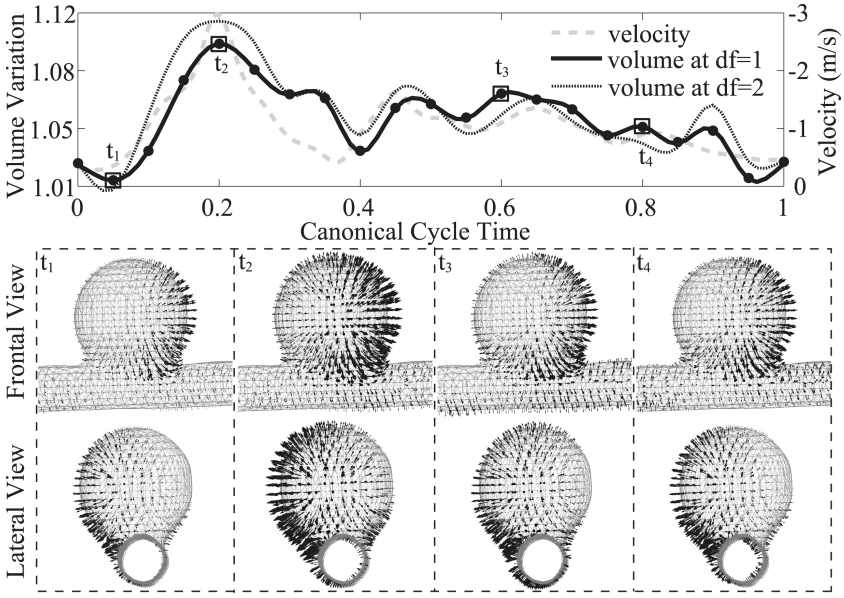

Figure 2.16: (a) The obtained volume variations with two downsampling factors df=1,2, along with the Doppler ultrasound velocity waveform. (b) Four (*boxes*) out of 20 (*dots*) estimated time points presenting the instantaneous wall displacements with respect to the reference geometry. (color version page C2)

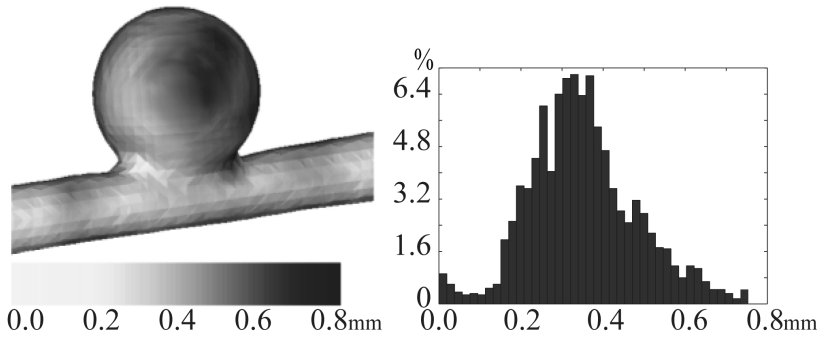

Figure 2.17: Color-coded displacement range over the cardiac cycle for each point on the surface, and the histogram of the displacement range. (color version page C2)

histogram of the deformed region. Only a small region has higher pulsatility, which can be observed from the color-coded map. Note that the rest of the deformed region

has an averaged pulsation range of around 0.3mm, part of which could be accounted for a global rigid movement.

2.5 Discussion

To validate the proposed methodology, experiments with digital and physical phantoms were performed. The phantoms presented aneurysms with pulsation ranges consistent with literature values. The imaging conditions matched what standard 3DRA imaging suites offer nowadays.

Experiments with digital phantoms were performed under controlled conditions, allowing to evaluate the sensitivity of our method to various factors. Results under ideal conditions showed estimation errors below 10% of the maximum pulsation, which in general presented subvoxel wall displacements not exceeding two voxels. In terms of algorithm parameters such as control grid size and weighting window width, similar results have been obtained. In terms of imaging conditions, different projection image resolutions provided similar estimation results; scattering and quantum noise degraded slightly the performance (maximum error of 20%) for smaller pulsation and aneurysm size cases (e.g., 8 mm with 1% maximum pulsation); FBP reconstruction artifacts decreased the performance, in general below the 10% except for the smaller pulsation aneurysms; angular resolution of the projection data is preferred to be higher. In case of disturbances from the imaged object such as head movement, estimation error increased to 20% with small perturbations. The presence of background objects raised slightly the estimation errors.

Experiments with the physical phantom allowed to demonstrate the feasibility of pulsation estimation under clinical conditions using anthropomorphic aneurysm replicas. The mismatches due to pulsation between the original projections and the simulated projections of the reference volume were corrected in the estimated volumes. In addition, the volume variation waveform presented a similar pattern compared to measured Doppler ultrasound velocity waveforms. Further validation could consider studying the mechanical relationship between the pressure/velocity and dynamic aneurysmal wall compliance.

A challenge for the method to be applied in large population studies and routine clinical practice is the computational cost. The high computational effort is partially compensated for by the current implementation, as mentioned in Appendix. It takes on average 10-15 minutes for one selected time point using a Pentium 4-3GHz PC, which requires further speed-up. The computing bottleneck is generating the simulated projections and computing the pixel-wise similarity metric. This could be potentially solved by either implementing them into hardware or using parallel computing.

Cerebral aneurysms could be more irregular in shape than the ones used in the experiments and little is known about their exact pulsation pattern and behavior at rupture. Therefore, the anatomical structure and pulsation waveforms used in these experiments might represent a simplified approximation of reality. Quantification of the accuracy of our method on patient data and large population studies must

be performed in the future. Methodological improvements under realistic acquisition settings might include the development of density-variable B-spline grids so that local deformation in small blebs can be optimally captured.

2.6 Conclusion

The objective of this chapter was to develop a methodology able to characterize patient-specific pulsatility of cerebral aneurysms over the cardiac cycle using 3DRA acquisitions. As a result, a registration-based technique has been proposed to recover motion from a reference 3D volumetric image and a set of 2D rotational projections synchronously acquired with a cyclic physiological signal. A number of experiments with digital and physical phantoms did illustrate the feasibility of estimating aneurysmal motion during the cardiac cycle.

Advantages of the presented technique can be detailed as follows: first, it does not require exposing patients to additional radiation as it uses the standard acquisition performed during an endovascular treatment. Second, compared to traditional algorithms of reconstruction from projections, it preserves the high spatial resolution of the 3DRA volume in spite of using a sparse set of projections because of the continuity and smoothness of the deformation model. In addition, its general formulation could be used to estimate motion of other organs.

2.7 Appendix: gradient of the registration metric

The gradient of the metric in (3.3) with respect to the parameters $\boldsymbol{\omega}$ can be expressed as:

$$\frac{\partial}{\partial \boldsymbol{\omega}} M(\boldsymbol{\omega}; t) = \sum_k \mu(t, t_k) \frac{\partial}{\partial \boldsymbol{\omega}} D\big(\tilde{I}_k(\boldsymbol{\omega}), I_k\big).$$

For the mutual information metric (2.4),

$$\frac{\partial}{\partial \boldsymbol{\omega}} D\big(\tilde{I}_k(\boldsymbol{\omega}), I_k\big) = \frac{\partial D\big(\tilde{I}_k(\boldsymbol{\omega}), I_k\big)}{\partial p(u,v)} \cdot \frac{\partial p(u,v)}{\partial \boldsymbol{\omega}},$$

where

$$\frac{\partial p(u,v)}{\partial \boldsymbol{\omega}} = \frac{1}{\Delta\tilde{h} \cdot N_k} \sum_{\mathbf{x} \in \mathcal{R}_k} \beta^{(0)}\Big(u - \frac{I_k(\mathbf{x}) - i_k^\circ}{\Delta h}\Big) \cdot \frac{\partial \beta^{(3)}(\hat{v})}{\partial \hat{v}}\bigg|_{\hat{v} = v - \frac{\tilde{I}_k(\mathbf{x};\boldsymbol{\omega}) - \tilde{i}_k^\circ}{\Delta\tilde{h}}} \cdot \Big(-\frac{\partial \tilde{I}_k(\mathbf{x};\boldsymbol{\omega})}{\partial \boldsymbol{\omega}}\Big),$$

N_k is the number of pixels in the valid ray region $\mathcal{R}_k$, and

$$\frac{\partial}{\partial \boldsymbol{\omega}} \tilde{I}_k(\mathbf{x}; \boldsymbol{\omega}) = \alpha(k, \mathbf{x}) \sum_\ell \nabla \overline{V}\big(\mathcal{T}(\mathbf{p}_\ell; \boldsymbol{\omega})\big) \cdot \frac{\partial}{\partial \boldsymbol{\omega}} \mathcal{T}(\mathbf{p}_\ell; \boldsymbol{\omega}),$$

where $\nabla\overline{V}$ denotes the spatial gradient of the volume.

Observing that, for B-spline transformations the Jacobian matrix $\partial\mathcal{T}(\mathbf{p}_\ell;\boldsymbol{\omega}) \,/\, \partial\boldsymbol{\omega}$ is a sparse matrix related to the order of the B-spline function, allowing to significantly speed up the computation. Furthermore, the evaluation of the metric and its gradient can be speeded up by just computing it within the valid ray region $\mathcal{R}_k$ for each projection.

3

Dynamic Estimation of Three-Dimensional Cerebrovascular Deformation from Rotational Angiography

The objective of this study is to investigate the feasibility of detecting and quantifying 3D cerebrovascular wall motion from a single 3DRA acquisition within a clinically acceptable time, and computing from the estimated motion field for the further biomechanical modeling of the cerebrovascular wall. The whole motion cycle of the cerebral vasculature is modeled using a 4D *B*-spline transformation, which is estimated from a 4D to 2D+t image registration framework. The registration is performed by optimizing a single similarity metric between the entire 2D+t measured projection sequence and the corresponding forward projections of the deformed volume at their exact time instants. The joint use of two acceleration strategies together with their implementation on graphics processing units are also proposed so as to reach computation times close to clinical requirements. For further characterizing vessel wall properties, an approximation of the wall thickness changes is obtained through a strain calculation. Evaluation on *in silico* and *in vitro* pulsating phantom aneurysms demonstrated an accurate estimation of wall motion curves. In general, the error was below 10% of the maximum pulsation, even in the situation when substantial inhomogeneous intensity pattern was present. Experiments on *in vivo* data provided realistic aneurysm and vessel wall motion estimates, whereas in regions where motion was neither visible nor anatomically possible no motion was detected. The use of the acceleration strategies enabled completing the estimation process for one entire cycle in 5-10 minutes without degrading the overall performance. The strain map extracted from our motion estimation provided a realistic deformation measure of the vessel wall. Our technique has demonstrated that it can provide accurate and robust 4D estimates of cerebrovascular wall motion within a clinically acceptable time, although it has to be applied to a larger patient population prior to possible wide application to routine endovascular procedures. In particular, for the first time, this feasibility study has shown that *in vivo* cerebrovascular motion can be obtained intra-procedurally from a 3DRA acquisition. Results have also shown the potential of performing strain analysis using this imaging modality, making thus possible for the future modeling of biomechanical properties of the vascular wall.

The content of this chapter is based on the publication:

Chong Zhang, Maria-Cruz Villa-Uriol, Mathieu De Craene, Jose-Maria Pozo, Juan Macho, Alejandro F. Frangi, Dynamic estimation of three-dimensional cerebrovascular deformation from rotational angiography, *Medical Physics*, 38(3): 1294-1306, 2011.

3.1 Introduction

Cerebrovascular diseases in general cause changes to the architecture of blood vessels in the brain by making them narrow, stiff, deformed, or uneven. The pathogenesis of these diseases is believed to be dependent on the complex interactions among multiple physiological and mechanical factors such as hemodynamics, wall biomechanics and mechanobiology [95]. Unfortunately, patient-specific vessel wall properties cannot be measured *in vivo* with current medical imaging techniques [49]. In many situations, an inverse problem approach based on a mathematical model for the biomechanics of the vasculature is a valid surrogate to estimate material and structural parameters [5, 46]. An example of such approach consists of determining these unknown parameters by applying known boundary conditions on the vessel wall and analyzing its mechanical responses such as vascular wall motion. Tracking this motion should also allow embedding wall compliance as a boundary condition for hemodynamic simulations [18]. Besides, other studies suggest that even the direct visualization of wall motion abnormalities may be helpful for analyzing pathological features of the cerebral vasculature [37, 45]. Therefore, quantifying vascular wall motion and deformation has the potential of impacting treatment selection and preoperative planning of cerebrovascular diseases. However, since such motion is in general expected to be in a sub-millimeter range [43, 45, 74], it represents a challenge in terms of the available image resolution of current clinical imaging techniques.

Various techniques have been proposed for estimating motion or reconstructing dynamic 3D structures using projection images acquired from image modalities like 3DRA and CBCT. ECG-gated techniques [64, 80, 88] constitute the most typical approach, where a reduced set of projections linked to a particular cardiac phase is used to reconstruct a volumetric image using iterative [10, 127] or analytical [20, 88] reconstruction methods. Recently, a technique [84] has been proposed to incorporate a 4D motion estimation into a projection motion-compensated 3D reconstruction process by comparing the latter to an initial reference reconstruction. However, the estimated motion could be limited by the 3D reconstruction error even before performing the 3D/3D registration. In other works [109, 126], continuous respiratory motion during a CBCT acquisition has been estimated by optimizing the similarity between the measured and the corresponding views of a deforming reference volume obtained from CT. However, their techniques need additional motion constraints such as an *a priori* motion model or a regularization term. Also, their need of two acquisitions increases patient exposure to radiation, limiting their clinical applicability.

We aim to retrieve the dynamic 3D morphology of a structure of interest from a single 3DRA acquisition (e.g. cerebral aneurysm or a vessel segment). 3DRA is routinely performed in clinical practice during endovascular interventions. One standard acquisition provides a sequence of 2D rotational X-ray angiographies and an isotropic high-resolution 3D volumetric image reconstructed from them. A physiological signal synchronized with the projections can also be recorded. In a previous work [130], we proposed a method to estimate the 3D morphology of the structure of interest at a given time instant by registering forward projections of the deformed 3DRA volume to a sparse set of 2D measured projections through a temporal weighting scheme.

However, since this technique only represents the spatiotemporal motion through independent 3D morphology estimation at discrete time points, it fails to address the intrinsic temporal consistency or continuity of motion. In addition, the estimated morphology can be compromised by the residual motion introduced by forcing the forward projections at a specific time instant to match the measured projections in its temporal vicinity. In general, this problem is also common for ECG-gated methods.

In this chapter, instead of representing the motion over time by independent 3D transformations as proposed in [130], we employ a single 4D *B*-spline transformation model for the whole motion cycle. It is estimated from a 4D to 2D+t image registration framework. The basic idea of the transformation model is to deform an object by manipulating an underlying mesh of control points, resulting in a smooth and continuous deformation of the reference image at any time of the motion cycle. Thus, an estimate of arbitrarily small displacement or deformation can be achieved through the interpolation from the movements of the control points. Meanwhile, the registration is optimized by measuring a single similarity metric between the entire measured projection sequence and the corresponding forward projections of the deformed volume at their corresponding exact time instants. This improves the temporal consistency without introducing blurring, as well as the robustness to image noise and artifacts such as contrast agent induced intensity inhomogeneity. Performing the motion estimation from the projection space improves the accuracy of the motion estimate as the pixel resolution is higher in the 2D+t measured projections than in the 3D image. On the other hand, computational cost is high for the simultaneous processing of such high-resolution temporal sequences of 3D images, 2D measured and forward projections. We therefore introduce the joint use of two acceleration strategies: a precomputation at the forward projection generation stage and an object-adaptive region-of-interest (ROI) for the forward projection update and the metric computation. Since less data have to be processed, these strategies also result in a reduction of memory requirements. Preliminary results and the overall registration framework were previously published as in [128]. Here a detailed method description is presented, with the integration of the acceleration strategies implemented on graphics processing units (GPU) [132]. An extended validation is performed on *in silico*, *in vitro* phantoms, and for the first time, on *in vivo* patient data. In this chapter, we also explore whether strain as estimated from the motion field from imaging data can be applied to the personalization of modeling of the vascular wall biomechanical properties.

3.2 Material and methods

3.2.1 Motion estimation algorithm

The motion estimation algorithm presented in this chapter consists of three steps. First, in order to overcome the limited spatial coverage from each of the separate motion cycles, the measured projections are reordered and built into one canonical motion cycle, according to a synchronized physiological signal such as ECG. Second, a 4D-to-2D +t image registration is performed to obtain a single spatiotemporal

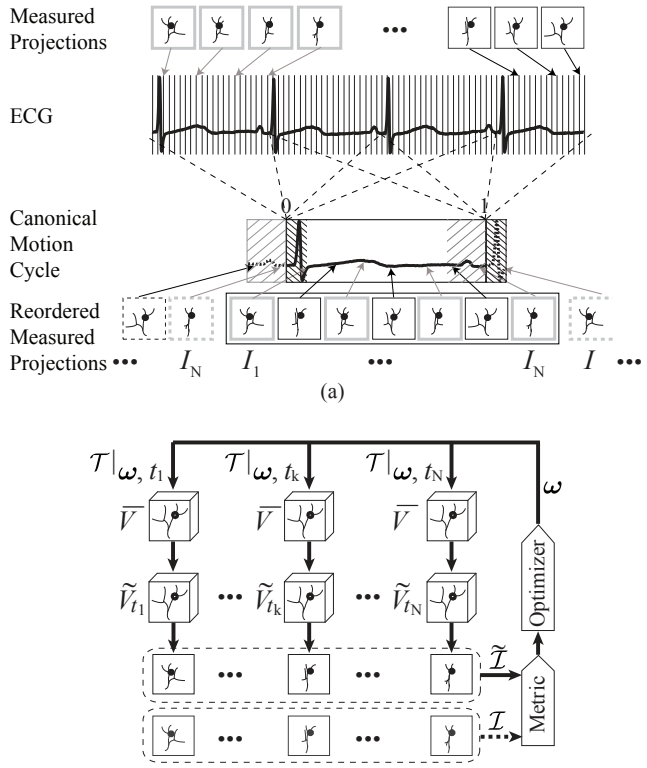

FIGURE 3.1: (a) Each motion cycle in the N measured projections sequence is normalized to have a unitary duration, according to a physiological signal such as ECG. And the time for each projection is normalized to the full length of its corresponding cardiac cycle. Thus all projections fall within a [0,1) interval. A reordered measured projections sequence can then be obtained based on this normalized time to form one canonical motion cycle. (b) An overview of the 4D-to-2D+t image registration framework, where one metric measuring the similarity between the measured and forward projection sequences, $\mathcal{I}$ and $\tilde{\mathcal{I}}$, is used to estimate a 4D continuous and smooth transformation model parameterized according to $\boldsymbol{\omega}$ over space and time.

transformation field over the whole canonical motion cycle. Third, after obtaining the optimal transformation parameter, instantaneous 3D images of the analyzed morphology at any desired time instant can be extracted by applying the 4D transformation to the reference volume image.

3.2.1.1 Canonical motion cycle

During the rotational run, the total angular coverage of the measured projections for one cardiac or motion cycle is 40-50°. Such viewing range may not be informative about the 3D motion along certain directions. This drawback could be potentially compensated for by providing an a priori motion model as in [109]. An alternative is to add a pseudo-periodicity constraint term to the optimization function as in [126]. However, the optimization process is complicated by the need of determining empirically the weight for such regularization. We overcome this limitation by reordering all the projections (spanning 4-5 cardiac cycles) to build one canonical motion cycle. This step is carried out as described in [130] and as illustrated in Fig. 3.1(a). We first normalize the period of each cycle to have a unitary duration according to a physiological signal such as ECG, which is recorded synchronously together with the projections. The time for each of the N measured projections is normalized to the full length of its corresponding cardiac cycle. Hence, all projections fall within the [0,1) interval and are then sorted by this normalized time to build one canonical motion cycle as $\mathcal{I} = \{I_{t_k}(\mathbf{x}) \mid k = 1 \dots N\}$, where $I_{t_k}(\mathbf{x})$ represents the measured projection and at the normalized time t_k ($0 \leq t_k \leq t_{k+1} < 1$). In practice, images acquired at similar cardiac phases in the canonical cycle are approximately separated by a 40-50° angular shift per cycle. By the use of this compounding strategy, the projection spatial viewing angle range is enriched at any temporal vicinity. In addition, the temporal resolution can be considered to be approximately increased by a factor corresponding to the number of cycles during the acquisition.

3.2.1.2 4D-to-2D+t image registration

The entire measured projection sequence is simultaneously processed to estimate a 4D continuous and smooth transformation model parameterized over space and time. A single metric captures the similarity between projection sequences instead of considering separate similarities between individual projections.

As shown in Fig. 3.1(b), motion throughout the canonical cycle is represented by a transformation $\mathcal{T}$ parameterized by $\boldsymbol{\omega}$. Thus, the 3D instantaneous motion at time t is given by deforming a reference volumetric image $\overline{V}$:

$$\widetilde{V}_t(\mathbf{p}) = \overline{V}(\mathcal{T}(\boldsymbol{\omega}, \mathbf{p}, t)), \tag{3.1}$$

where $\mathbf{p}$ is a point in $\widetilde{V}_t$. In this chapter, a B-spline based transformation [85, 107] is used. The displacement of $\mathbf{p}$ is represented by a 4D tensor product of cubic B-spline functions (i.e. $\beta(\cdot)$ in the temporal dimension and $B(\cdot)$ the 3D tensor of $\beta(\cdot)$ in the spatial dimensions), defined on a sparse control points grid $(\mathbf{p_c}, t_\tau)$:

$$\mathcal{T}(\boldsymbol{\omega}, \mathbf{p}, t) = \mathbf{p} + \sum_{\tau,\mathbf{c}} \beta\left(\frac{t - t_\tau}{\Delta_\tau}\right) B\left(\frac{\mathbf{p} - \mathbf{p_c}}{\boldsymbol{\Delta}_\mathbf{c}}\right) \boldsymbol{\omega}_{\tau,\mathbf{c}}, \tag{3.2}$$

where $\boldsymbol{\omega}$ is an array of the control grid coefficients, acting as parameters of the B-spline, $\mathbf{c}$ the spatial index and τ the temporal index, $(\boldsymbol{\Delta}_\mathbf{c}, \Delta_\tau)$ the width of the

functions in each dimension. This transformation model ensures both temporal and spatial consistency and smoothness without compromising the local motion recovery due to its local control property. More importantly, an estimate of small displacement or deformation can be achieved through the underlying interpolation between the control points. Note that to keep the continuity at both ends of the cycle ($t_{\tau_{min}}$=0 and $t_{\tau_{max}}$=1), we need to impose a pseudo-cyclic condition $\boldsymbol{\omega}_{\tau_{min},\mathbf{c}} = \boldsymbol{\omega}_{\tau_{max},\mathbf{c}}$. A simple implementation is to extend the range of the transformation model on the temporal axis at both ends, as illustrated in Fig. 3.1(a).

For each I_{t_k}, a corresponding digitally reconstructed radiograph (DRR), $\tilde{I}_{t_k}$, is calculated to simulate the X-ray angiography through a ray casting process [96]. For the rotational angiography (RA) sequence, their projection geometry is known for each projection, including the X-ray source position, the projection detector position, and the rotational orientation. We denote by $\tilde{\mathcal{I}}$ the entire DRR sequence, which is iteratively modified to match the measured projection sequence $\mathcal{I}$ for an optimal estimation of $\hat{\boldsymbol{\omega}}$:

$$\hat{\boldsymbol{\omega}} = \underset{\boldsymbol{\omega}}{\operatorname{argmin}} \left\{ M(\boldsymbol{\omega}, \mathcal{I}, \tilde{\mathcal{I}}) \right\}, \tag{3.3}$$

where M is the similarity metric between two mapping regions. Mutual information [54, 113] is used as the metric. Since the registration matches simultaneously all the projections, sampled points from the entire sequence are considered as within one region, forming a single histogram. Therefore, instead of having one independent metric for each projection pair, M describes the similarity between the two sequences $\mathcal{I}$ and $\tilde{\mathcal{I}}$. Histograms are approximated using Parzen windows for the probability calculation [58]. The use of one metric measuring the similarity between projection sequences makes the registration more robust against local intensity variations (e.g noise and inhomogeneous contrast mixing) than considering similarities between individual projections separately. Note that due to the higher spatial resolution in measured projections compared to the volumetric image, performing the motion estimation from the projection space improves spatial accuracy of the recovered motion field. In our case, a displacement equivalent to one pixel translates into approximately 0.3 voxel. The L-BFGS-B algorithm [133] is used as the optimizer, due to its ability in handling a very large number of parameters.

3.2.2 An efficient implementation

Dealing simultaneously with such high-resolution 4D image, 2D measured projections and DRRs, requires excessive memory and long computation time. For the method to be practically applicable, reducing both of them without degrading the performance is desirable. Two strategies are jointly used in order to process the data of interest at each iteration during the registration process. The fact that both computation and memory costs scale with the amount of processed data makes these strategies efficient. They are further implemented on GPU so as to facilitate the clinical use of our technique at a reasonable execution time. The main idea of the GPU

implementation method is summarized in Appendix3.7 and a detailed description can be found in [132].

3.2.2.1 DRRs precomputation

In 3DRA images, the structure of interest (e.g. an aneurysm or a vessel segment) is in the order of millimeters, occupying a reduced region in the image (see an example in Fig. 3.2(a)). Thus, during the motion estimation process, the transformation can be applied only to a volume of interest (VOI) while the rest of the volume remains unmodified. Provided that the actual motion present outside the VOI is smaller than or of the same magnitude as the motion in the VOI, it will not affect significantly the estimated motion. The reason is that due to the use of a sparse *B*-spline control-points grid, any motion outside may only influence one projection in a particular direction while the motion of each control point is the result of several projections. However, in order to simulate realistic X-ray projections, voxels of the entire volume must be integrated at each iteration to update the DRRs. In order to avoid redundant computation, for each pixel $\mathbf{x}$, the corresponding ray is split into two parts: inside and outside the VOI. The constant outside part is precomputed, and at each iteration only the inside part is integrated and updated to the sum of both parts. An illustration is shown in Fig. 3.2(a) for a VOI containing an aneurysm. The speedup factor using such pre-computation is the ratio between the ray segment length crossing the entire volume and that of the VOI. The memory reduction rate is also expected to scale with this factor.

3.2.2.2 Object-adaptive region-of-interests

A common approach to accelerate the metric computation is to subsample the images. Uniform subsampling is not the most efficient method, and special attention should be paid to reduce the calculation of the metric and its derivatives by sampling, for example the object of interest [87] or its edges [8]. We follow this strategy by encouraging dense sampling of image regions that strongly influence the metric. Since morphology changes of the aneurysm or vessel wall are reflected on the contrast enhanced lumen boundaries, two object-adaptive sampling regions are introduced: the projected object ($\mathrm{S_{OR}}$) and the projected boundary ($\mathrm{S_{BR}}$). Consequently, the typical projected VOI, denoted as $\mathrm{S_{VR}}$, for the computation of the metric are replaced by the sequences of pixels from the sampling regions $\mathrm{S_{OR}}$ or $\mathrm{S_{BR}}$. An illustration of these regions is shown in Fig. 3.2.

There are many techniques automatically delineate such regions. Note that the accurate definition of the sampling regions in 2D is not crucial for our method, as our interest is to quantify 3D morphological changes. And since a reference image is available in 3D, we first obtain one approximated 3D shape of the region using a threshold-based method, and then define the region by simply projecting it on each projection. A unique property of a 3DRA volume is that, looking at the histogram of this 3D image, there is a sharp differentiation of the contrast agent (CA) filled regions (i.e. aneurysms and vessels) from the background. This results in clearly

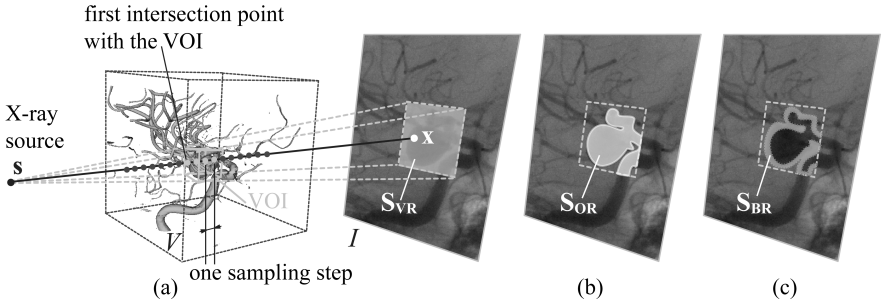

FIGURE 3.2: (a) An illustration of the DRRs computation process. For each pixel $\mathbf{x}$, the corresponding ray is split into two parts: inside and outside the VOI. The constant outside part is precomputed, and at each iteration only the inside part is integrated and updated to the sum of both parts. The sampling region S_{VR} contains the projected VOI. We introduce here two object-adaptive sampling regions: (b) the projected object region S_{OR} and (c) the projected boundary region S_{BR}.

separated classes with the CA filled regions mapped to high voxel value range and the background to low voxel value range [12, 80]. Meanwhile, on the contrast filled boundaries in the projection images, in general a region of progressive intensity change exists. This is mainly due to the changes in length of the X-ray traversing the contrast-filled region on the boundaries, resulting in a continuous change of the accumulated attenuation. Consequently, this results in a similar pattern in the 3D reconstructed volume. Based on this observation, the S_{OR} is calculated for each projection as follows. First, a boundary value of the studied object is selected by identifying the CA filled regions from the histogram. Second, on the corresponding ray for a specific pixel, as long as there is one sampled point having larger intensity than this boundary value, the pixel is considered to be part of the S_{OR}. The obtained region is comparable to the projected "shadow" of a 3D object from thresholding. Similarly for the S_{BR}, we first obtain two of these regions from different threshold values, by repeating the process of the S_{OR} region for two thresholds. One overestimates (i.e. higher threshold) and the other underestimates (i.e. lower thresholds) the contrast filling region. The S_{BR} region is obtained by subtraction of the two resulting regions. These boundary identifying values or thresholds in the histogram can be obtained empirically or using e.g. Otsu's method [73]. Note that this gradually changing intensity pattern on the boundaries between the contrast-filled region and the background also helps the recovery of a subvoxel displacement estimated through the deformation of the reference image. The reason is that such an intensity function follows a smooth transition that gives information on the boundaries at a finer scale than the voxel grid, i.e. subvoxel resolution.

3.2.3 Strain map computation

A number of mechanical and anatomical parameters can be used to characterize the morphological and dynamic wall properties of the vasculature. We consider the strain map extracted from the non-rigid wall motion estimation as a simplified but adequate way towards characterizing the vascular wall tissue. Such quantities provide a measure of the relative deformation to which the arterial wall is exposed.

We study the distension of the vascular wall, which is related to the changes in wall thickness. This relationship is more evident, for instance, under the volume-preserving assumption as in [5], where the radial Cauchy strain is used. Specifically, it is computed from triangular meshes that are extracted from the estimated volume images. Assuming the volume of the material is preserved, the changes of the area A_{tr} for each triangle are inversely proportional to the changes in wall thickness L_w: $A_{tr} \times L_w = A_{tr}^{'} \times L_w^{'}$. Thus the radial Cauchy strain ε_c is calculated as:

$$\varepsilon_c = \frac{\Delta L_w}{L_w} = \frac{-\Delta A_{tr}}{A_{tr}^{'}}$$

where $\Delta L_w = L_w^{'} - L_w$ and $\Delta A_{tr} = A_{tr}^{'} - A_{tr}$. This means that the strain value is positive if the material is stretched, or negative if it is compressed.

3.3 Validation

3.3.1 Experimental data

Our method has been currently applied to cerebrovascular wall motion with a particular emphasis on cerebral aneurysm pulsation. We present here experiments on *in silico* and *in vitro* aneurysm models, and also *in vivo* patient data.

In silico: Twelve cases of digital aneurysm phantom models were created with dome diameters of 8, 10, and 12 mm and parent vessel diameter of 4 mm. They also have an emerging bleb on the dome. The phantom motion was modeled as smooth geometry changes according to a sinusoidal pulsation waveform and was sampled at a finite number of time points. According to the values on *in vivo* data presented in recent studies [43, 45, 74], maximum pulsation amplitudes were set to be 1%-4% of the dome diameter (i.e. 0.08-0.48 mm). A sequence of volume images with an isotropic spacing of 0.3 mm was generated from the sequence of ground-truth geometries. Voxel intensities were obtained as a function of the signed distance from the voxel to the object surface. The result is an image with a constant value inside the object and another value outside, but with a blurred band of 0.5 mm around the object boundary. Afterwards, this ground-truth volume sequence was used to generate the synthetic measured projections with 0.16 mm spacing. In order to simulate other attenuated vessels, air, bones, and soft tissues, we embedded the phantom images into a 3DRA patient image that serves as background. An illustration is shown in Fig. 3.3(a). Once each phantom was placed within the patient image, the voxels corresponding to aneurysm and vessel were set to a typical intensity value of the CA filled regions.

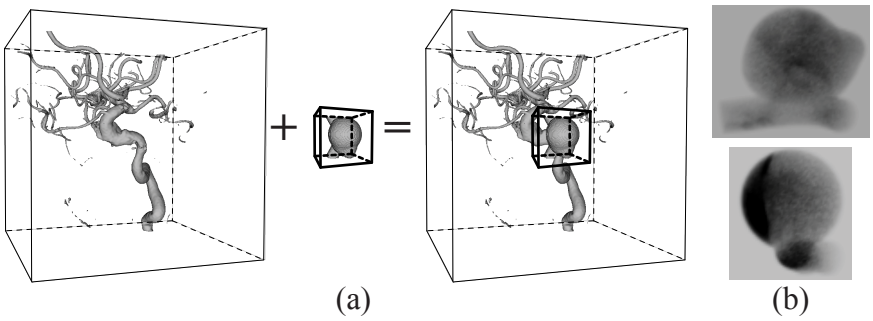

FIGURE 3.3: (a) An example of an *in silico* phantom image, where the phantom model is embedded into a 3DRA patient image. (b) Projections with contrast inhomogeneity synthesized based on a RA patient data with strong blood turbulence.

In addition, in this chapter we simulated spurious projection intensity variations in order to analyze the sensitivity of our method and compare with other techniques. Such intensity inhomogeneity is in general caused by the contrast filling following the blood flow. However, the instantaneous local inhomogeneity might be caused by multiple factors. In order to simulate realistic intensity variations, we sampled the RA image intensities from a patient data where the aneurysm dome presented substantial nonuniform intensities including strong blood turbulence. For the phantom dome region in each measured projection, an image patch of the same shape was taken from the dome of the patient case and mapped directly to the phantom image (Fig. 3.3(b)).

In vitro: A silicone side-wall aneurysm phantom model (Elastrat, Geneva, Switzerland) was used. The model has a spherical dome with 10 mm diameter and a straight cylindrical parent vessel with 4 mm diameter. It was placed in a rectangular container with dimensions comparable to a human head. The container was water-filled to mimic the attenuation of head tissue. In addition, two other phantoms with straight tubes were also placed in the container to simulate background. The phantom was water-filled and connected to a customized pulsatile pump, a continuous flow pump (Elastrat, Geneva, Switzerland), and a liquid tank to create a continuous and pulsatile flow circuit (Fig. 3.4(a)).

The image acquisitions were performed using an Allura Xper FD20 scanner (Philips Healthcare, Best, The Netherlands) equipped with a 220 mm detector field of view (diagonal dimension) allowing a coverage of 75 mm of a cubic volume during a single rotation. For these acquisitions, the injection protocol consisted of 18 mL of iodinated contrast material (Iomeron 400, Bracco Imaging SpA, Milan, Italy) with a flow rate of 3 mL/s. RA imaging was performed at a frame rate of 30 Hz during contrast injection, with a 2 s delay. These settings of the model and the imaging conditions give a realistic amount of scattering, beam hardening and noise. An example RA image of the *in vitro* phantom is shown in Fig. 3.4(b). In total, 121 images were acquired (1024^2

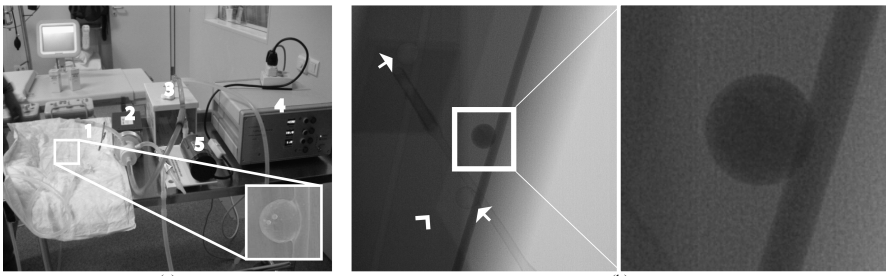

FIGURE 3.4: (a) *In vitro* phantom experiments setup: 1. the silicone side-wall aneurysm; 2. the customized pulsatile pump; 3. the liquid tank; 4. the pulsatile signal generator; 5. the continuous flow pump. (b) An example X-ray angiography of the *in vitro* phantom. The phantom was placed in a water-filled rectangular container (*arrow head*) with dimensions comparable to a human head. Two additional aneurysm phantoms with straight tubes (*arrows*) were also placed in the container, to act as background.

pixels with $(0.154\ \text{mm})^2$/pixel) spanning $\sim 210^\circ$ along the gantry trajectory, from which a 3D volume of 256^3 voxels ($(0.3\ \text{mm})^3$ per voxel) was reconstructed. X-ray source and detector positions were recorded for each projection, allowing the spatial relationship between the reconstructed reference volume and each projection to be known. The scanning procedure and the imaging parameters of the system followed a standard clinical protocol, which were also used for the *in vivo* cases presented below. Detailed values are summarized in Table. 3.1.

Three acquisitions were performed at different pump piston movement settings, resulting in three phantom pulsation states: large pulsation (LP), small pulsation (SP), and non-pulsation (NP). Although exact aneurysm pulsation amplitudes were unknown, the pulsation range was in accordance with the expected range from visual inspection.

In vivo: 3DRA acquisitions from two patients with cerebral aneurysms were analyzed in this chapter. Both examinations were collected at Rothschild Foundation Paris, using an Allura Xper FD20 scanner (Philips Healthcare, Best, The Netherlands). For these examinations, the injection protocol consisted of 24 mL of contrast agent (Iomeron 350, Bracco Imaging SpA, Milan, Italy) with a flow rate of 4 mL/s, with a 2 s delay. Patients were under general anesthesia during the whole examination. We have estimated motion at various locations as indicated in Fig. 3.5. Three types of motion were visually observed from these regions: aneurysm wall motion, vessel wall motion, and catheter tip displacement. For patient #1, aneurysm motion could not be confirmed from the RA sequence, but we observed it from an available DSA sequence. For patient #2, aneurysm motion was not visible in the RA sequence, but we did observe vessel motion and longitudinal displacements of the catheter.

For all the experiments tested on these data, we chose a VOI of approximately

TABLE 3.1: 3DRA imaging settings for the *in vitro* and *in vivo* data, using the Allura FD20 imaging system.

Parameters	Unit	Value
Tube Voltage	KV	78-89
Tube Current	mA	180-280
Exposure Time	ms	6-8
Detector Dose	nGy/fr	∼200
Detector Format	cm	22, 27
Focal Spot Size	mm	0.4
Source-To-Isocenter Distance	mm	∼810
Source-To-Detector Distance	mm	∼1195
Geometric Magnification	-	∼1.475
Rotation Range	°	∼210
Number of Projections	-	121
Frame Rate	fps	30
Pixel Spacing	mm	0.154
Voxel Spacing	mm	0.3
Contrast Injection Time	s	6
Contrast Injection Rate	mL/s	3-4
Iodine Density	mg/mL	350-400
Collimator Filter (Alu)	mm	1.0
Collimator Filter (Cu)	mm	0.1
Anti-Scatter Grid	lp/cm	80

50^3 voxels. The number of sampled pixels in the sampling regions S_{VR}, S_{OR} and S_{BR} at each projection view were in the order of 5000, 3000 and 500, respectively. The B-spline control point grid spacing was about 1.5 mm for the spatial dimension, and 10-12.5% of the canonical motion cycle for the temporal dimension.

3.3.2 Accuracy evaluation

In order to quantitatively evaluate the accuracy of the estimated motion, a set of deformed 3D volume images at discrete time points was extracted according to the estimated 4D transformation. A relative error was measured at each time point t as a percentage of the pulsation range,

$$e(t) = \big(m_r(t) - m_g(t)\big)/\hat{m}_g \times 100\%, \tag{3.4}$$

where $m_g(t)$ is the ground-truth pulsation measurement (e.g., volume changes) at t, $m_r(t)$ the corresponding estimated measurement, and $\hat{m}_g$ the variation range of $m_g(t)$ over the canonical cycle.

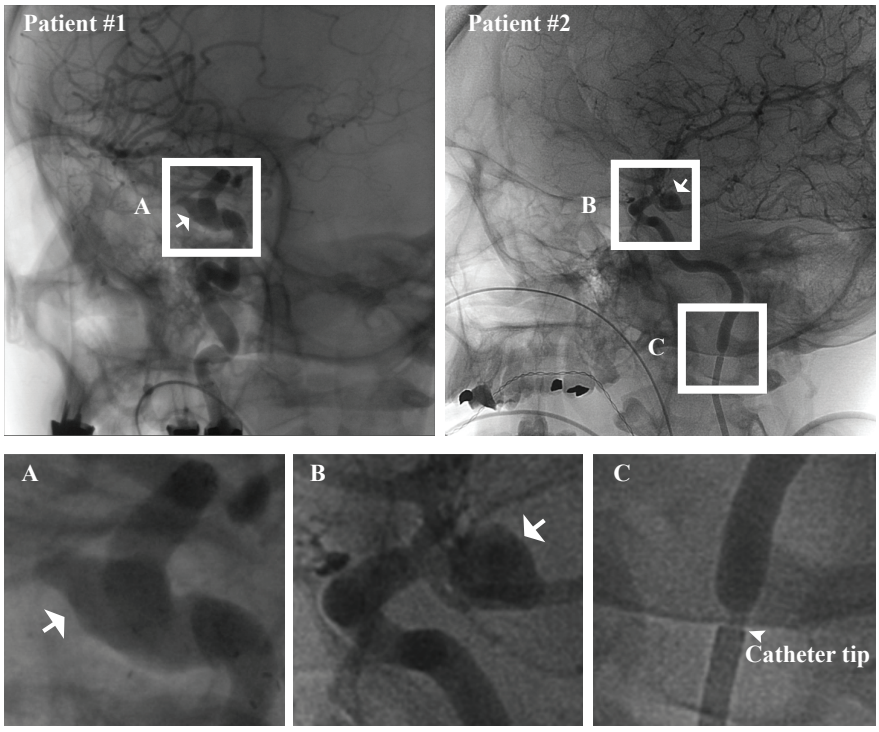

Figure 3.5: Details of *in vivo* datasets, indicating with *arrows* the aneurysms and with an *arrow head* the catheter tip. Data from two patients were used in this work, where our method has been applied to different regions: (A) aneurysm with visible motion; (B) aneurysm without visible motion; (C) vessel segment with visible motion, and the imaged catheter (lower part) with longitudinal displacement.

In terms of volume change measurements, they were calculated using a method similar to the one as in [33], by transforming a binary mask image using the deformation field and subsequently summing up the intensities. The partial volume of the boundary voxels was calculated by dividing the sum of the interpolated intensities by the interval length.

3.4 Results

3.4.1 *In silico* aneurysm wall motion

For each case, we extracted 16 volume images at equally distributed time points along the canonical motion cycle. As the ground-truth is known for these phantom data, a quantitative accuracy evaluation is possible. In the presented experiments,

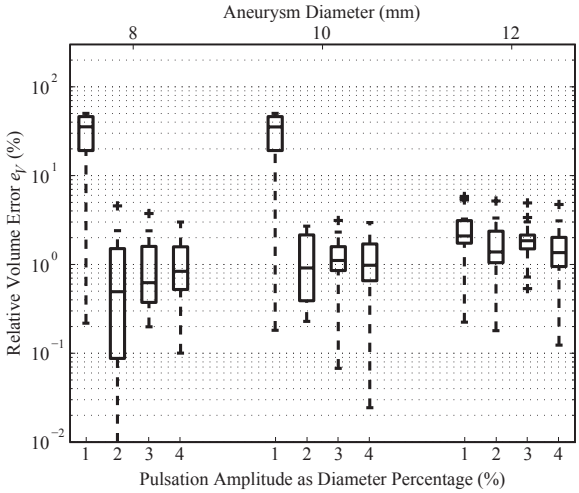

FIGURE 3.6: Boxplots of e_V at 16 equally distributed time points for 12 *in silico* phantom cases of different diameter (8, 10, and 12 mm) and maximum pulsation range (1%-4%).

we used the relative error in volume changes, e_V, calculated according to Eq. 3.4. Except for two cases in which the maximum pulsation was below 0.1mm (being the 8mm and the 10 mm dome with 1% maximum pulsation), the relative error in volume changes, e_V, was below 10%, as can be seen in Fig. 3.6.

In the example shown in Fig. 3.7, e_V and the computational time are plotted for the same number of registration iterations. In this experiment, we investigated the effects of using a combination of three different schemes: sampling region, angular resolution along the C-arm gantry trajectory, and the GPU implementation. The angular resolution of the measured projection sequence was downsampled by a factor of 1 to 4. Results show similar accuracy (e_V <5% up to three quartiles) achieved from the three sampling regions combined with an angular resolution downsampling factor up to 3. Therefore, given the fact that less projections can be used, it can be speculated that this also enables discarding the use of a few undesirable projections, e.g. the ones with severe artifacts. No significant differences were obtained when DRRs were generated using either the CPU or GPU implementation. The slight GPU/CPU discrepancies can be attributed to the difference in data type specifications between the processors [36]. Due to the speedup introduced at the GPU-based DRR generation stage, the image registration process can be reduced by an additional factor of up to 2x with respect to the corresponding CPU-based implementation. Therefore, the estimation results for the complete motion cycle can be obtained in 5-10 minutes when using S_{BR} on the GPU DRR implementation using a downsampling factor of 3.

Fig. 3.8 shows the color maps of the wall displacements and the radial Cauchy

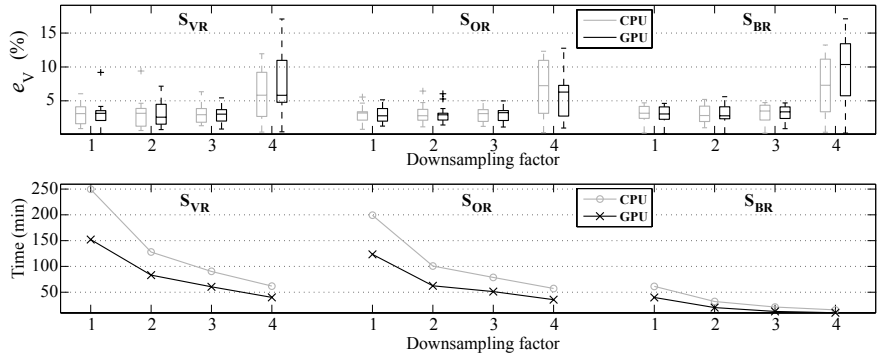

FIGURE 3.7: Performance evaluation on the use of a combination of three different schemes in terms of estimation error e_V and computational time. The three schemes are: sampling regions (S_{VR}, S_{OR}, S_{BR}), angular resolutions along the C-arm gantry trajectory (downsampling factor being 1-4), and the GPU implementation. Results were obtained from an *in silico* phantom with 12 mm diameter and 3% pulsation (i.e. maximum amplitude of 0.36 mm).

strain estimated at the maximum and minimum pulsation states of an *in silico* phantom with diameter of 12 mm and pulsation of 3% (i.e. maximum amplitude of 0.36 mm). In regions with similar surface curvatures like the dome, the strain field presents a similar pattern to the displacement field, whereas in regions with higher curvatures, such as the bleb and the neck, the strain scales faster. This suggests that the strain field might enhance more efficiently regions having a different deformation pattern as strain is less insensitive to passive motion but focuses on differential motion.

3.4.2 *In vitro* aneurysm wall motion

For the three pulsation states under evaluation, we obtained larger motion in the LP case, smaller motion but with a similar pattern in the case of SP, and no motion for the NP case. We show here the results of the LP case in Fig. 3.9. As the ground-truth is unknown, the results are qualitatively presented. In Fig. 3.9(a-b), a measured projection is compared with its corresponding DRR calculated from the reference volume and from our estimated volume. From the visual inspection in the projection space, our technique demonstrates its ability in correcting the misalignment between the measured projection and the DRR. In Fig. 3.9(c-d), color maps show the wall displacement amplitude and the strain at the time point with the largest motion. An inhomogeneous wall displacement distribution is observed and is especially concentrated on a lateral side of the aneurysm dome. This is caused by a slight axial tilting of the phantom tube position during the acquisition. This is in agreement with the reduced effect in terms of strain distribution observed at the same location, since part of the displacements came from a global movement.

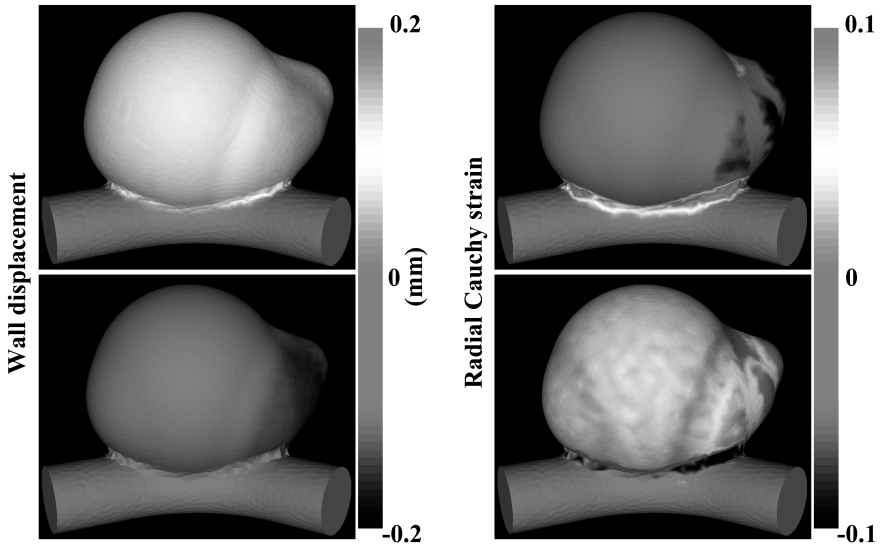

FIGURE 3.8: Wall displacement amplitude and radial Cauchy strain at the maximum (*top*) and minimum (*bottom*) deformation states for an *in silico* phantom with diameter of 12 mm and pulsation of 3% (i.e. maximum amplitude of 0.36 mm). (color version page C3)

3.4.3 *In vivo* cerebrovascular motion

Our estimation recovered the visually observed aneurysm motion from patient #1 and vessel motion from patient #2. For patient #2, aneurysm motion was neither observed nor recovered. Fig. 3.10 and Fig. 3.11 summarize the recovered motion from patients #1 and #2, respectively. The color maps show the displacements and the radial Cauchy strain at the end-systolic (ES) phase, which coincided with the cardiac time of the measured projections where maximum motion was visually observed. This phase represented also the time of the maximum motion estimated from our technique, as can be seen in the displacement curves over time in both figures. These curves show that the aneurysm in patient #1 and the vessel motion in patient #2 presented a similar pattern with respect to the cardiac phases indicated by the ECG signal. Spatially, for instance in Fig. 3.10, the motion was clearly observed in the projections only in a small area of the aneurysm dome, which coincides with the maximum estimated wall displacement region using our technique. Also, we observed that, in Fig. 3.11 the upper part of the vessel (i.e. internal carotid artery) did not show any visible motion. This is consistent with the fact that this particular vessel segment, i.e. the petrous segment, is surrounded by stiff bony structures preventing any motion at this location.

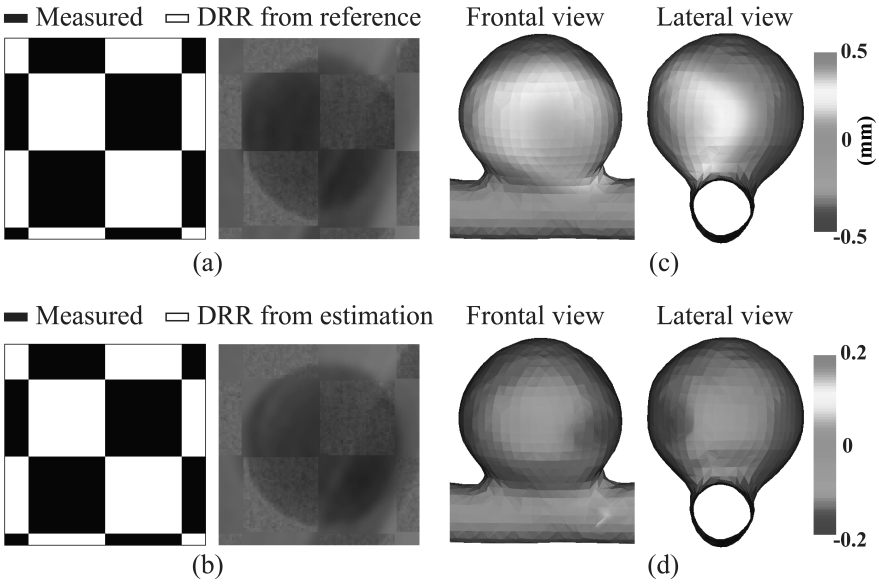

FIGURE 3.9: Results from *in vitro* LP phantom: (a,b) Example of checkerboard images for the *in vitro* phantom comparing respectively the measured projection with the equivalent DRR computed from the reference volume and our estimation. The color maps of the wall displacement amplitude (c) and the radial Cauchy strain (d) for the frontal and lateral views at the instant presenting the largest displacement. (color version on page C3)

3.4.4 Catheter displacement

From the measured projections for patient #2, we observed substantial longitudinal displacement of the catheter, corresponding to the catheter tip moving vertically along the direction of the vessel and following the blood flow. To further verify the feasibility of our method in recovering general motion other than vascular wall motion from a rotational angiography acquisition, we have applied it to the imaged catheter region and recovered the displacement of the catheter tip. Results are shown in Fig. 3.12. The color maps show respectively the displacements (Fig. 3.12(a)) at 10 equally sampled time instants over the cardiac cycle. And the catheter tip displacement (along the vessel longitudinal direction) is plotted with the ECG signal in Fig. 3.12(c). The cardiac phase when the maximum value of this movement occurred was similar to the maximum vessel motion phase (Fig. 3.11(d)). This confirms that the catheter moved back and forth according to the pulse of the blood flow. We have also plotted the calculated strain maps at the catheter surface in Fig. 3.12(b). As the strain represents deformation instead of rigid movement, it should be ideally zero everywhere and for all time instants. As expected, at the lower and homogeneous part of the catheter, zero radial displacements and strain

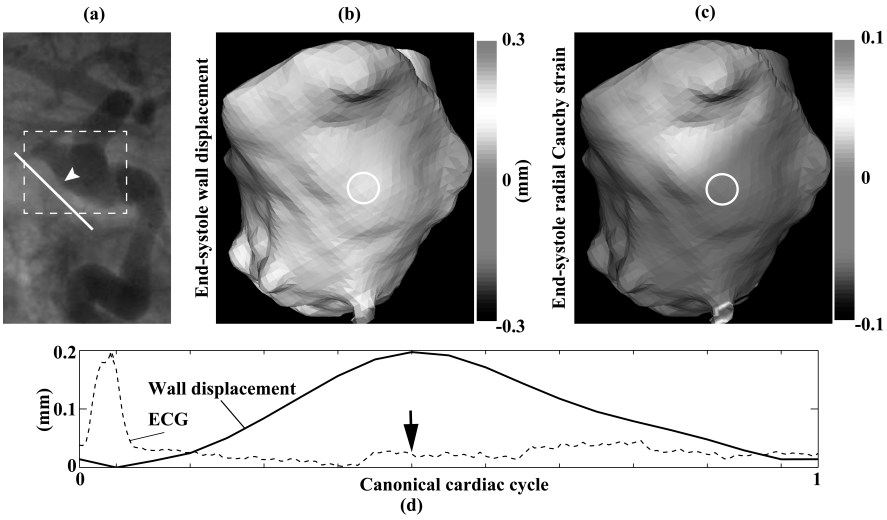

FIGURE 3.10: Results of aneurysm wall motion in patient #1. (a) A close view indicating the region where our motion estimation method has been applied (*dashed frame*) in an X-ray angiography. (b) The color map (*line* in (a) indicating the viewing plane) of the displacements around the end-systolic (ES) phase (indicated by the *arrow* in (d)). (c) The radial Cauchy strain at the same phase as in (b). (d) Aneurysm wall displacement amplitude over the cardiac cycle at the location indicated by the *arrow head* in (a) and the *circles* in (b,c). (color version page C3)

values were obtained. However, they were not zero everywhere at the catheter tip. A first explanation for such behavior of the results is that the catheter used during the intervention had a flexible tip and therefore was prone to deformation. Second, the estimated vessel motion was "propagated" to its immediate vicinity, the catheter tip, since the *B*-spline transformation provides a spatially smooth estimate of the displacement field. And third, at the catheter tip, larger inhomogeneity of the contrast agent mixing are expected, which in turn might affect our intensity-based registration method.

3.5 Discussion

In silico pulsatile aneurysm phantom results have demonstrated that the estimation error was below 10% in recovering motion in the sub-millimeter range, e.g. in the order of a voxel, even from images with substantial intensity inhomogeneity. *In vitro* aneurysm phantom experiments have allowed verifying that our method is able to detect whether an aneurysm pulsates or not. However, in a clinical environment, due to the lack of ground-truth motion information, we were not able to

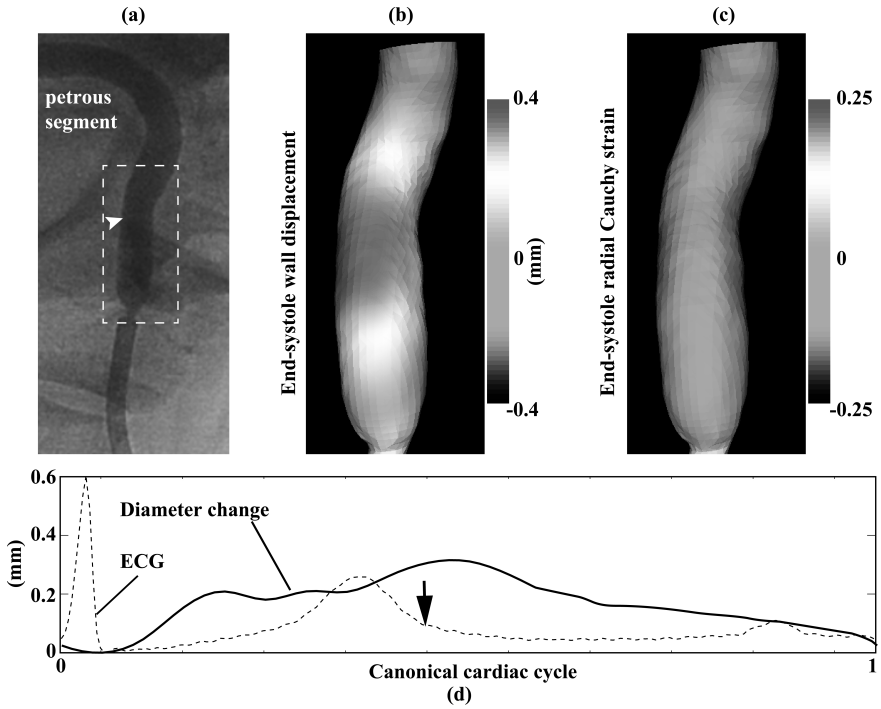

FIGURE 3.11: Results of vessel wall motion in patient #2. (a) A close view indicating the region where our motion estimation method has been applied (*dashed frame*) in an X-ray angiography. (b) The color map of the displacements around the end-systolic (ES) phase (indicated by the *arrow* in (d)). (c) The radial Cauchy strain at the same phase as in (b). (d) The vessel diameter change over the cardiac cycle at the location as indicated by the *arrow head* in (a). (color version on page C4)

validate quantitatively the performance of the method. Nonetheless and for the first time, experiments carried out on *in vivo* patient data presenting visible aneurysm and vascular wall motion as well as catheter tip movement, have demonstrated the feasibility of our method for motion detection and recovery from RA. In regions where motion or deformation is impossible from an anatomical point of view, such as the petrous segment and the catheter, the results were consistent with the expected zero motion. In summary, although ground-truth was unknown for the *in vitro* and the *in vivo* data, our results were qualitatively accurate. Given the realistic modeling of spatial and temporal imaging conditions as well as the morphology and motion range, the performance of our method on *in silico* data can be expected, to a certain extent, to be translatable to patient data acquired in a clinical situation.

To facilitate the translation of this technique into clinical practice, we proposed

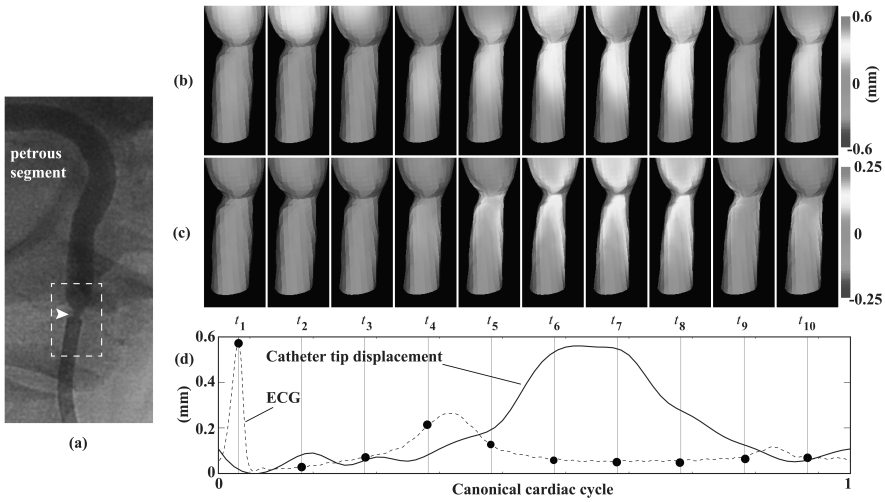

FIGURE 3.12: Results of catheter tip movements in patient #2. (a) A close view indicating the region where our motion estimation method has been applied (*dashed frame*) in an X-ray angiography. The color maps of the estimated catheter movements (b) and the strain (c) at ten selected time points. (d) The catheter tip (*arrow head* in (a)) longitudinal displacement plotted together with the ECG signal. (color version on page C4)

the joint use of two acceleration strategies together with their implementation on graphics processing units. This has demonstrated a successful memory management and speedup for processing large 3D and 2D datasets from 3DRA acquisitions. These improvements allowed completing the motion estimation process for one entire cycle in 5-10 minutes without degrading the overall performance. More specifically, we obtained a 3-4x speedup from the precomputation of surrounding vascular structures outside the VOI, and a 10x from the use of S_{BR}. With respect to the CPU implementation, an additional speed improvement of up to 2x was achieved by integrating the GPU generated DRRs in the motion estimation framework.

Since the object-adaptive ROIs are calculated based on two selected voxel values as described in Section 3.2.2.2, the potential influence of these intensity values on the estimation is discussed here. Experiments were performed on an *in silico* phantom (dome diameter of 12 mm and maximum pulsation of 3%) embedded in a 3DRA patient image. Voxel intensities of the phantom dome were set to be constant inside (i.e. a value belonging to the CA filled region), and to be smoothly changing on the boundary, depending on the distance from the voxel to the ideal wall surface. Results are demonstrated on four S_{BR} regions (denoted as R1-R4), chosen from different combinations of four sub-ranges equally spanning the intensity range of the phantom. The lower boundary intensity value of R1 was chosen to be higher than the actual boundary and thus was inside the phantom. That means, in R1 the aneurysm wall

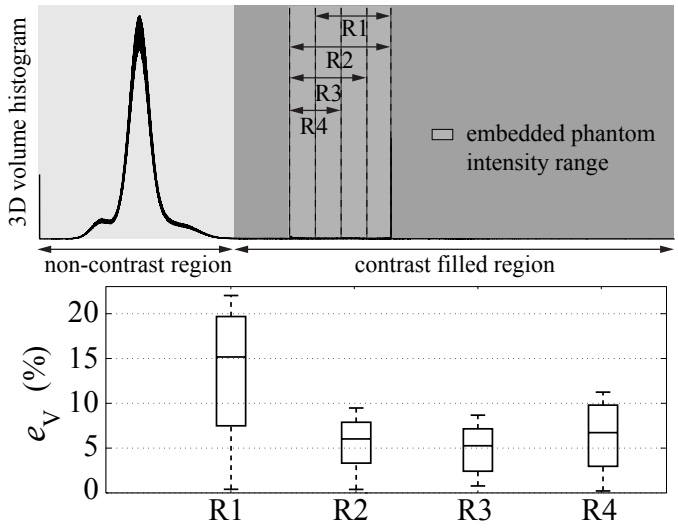

FIGURE 3.13: Comparison of the accuracy using four different S_{BR} regions (denoted as R1-R4), chosen from different combinations of four sub-ranges equally spanning the intensity range of the phantom. Results in this figure were obtained from an *in silico* phantom embedded in a 3DRA patient image (see an illustration in Fig. 3.3(a)). The phantom has a diameter of 12 mm and the maximum pulsation of 3% (i.e. maximum amplitude of 0.36 mm).

was not included, while in R2 to R4 the actual aneurysm wall was always included but with the inner boundary identified by three different values spanning the aneurysm intensity range. Detailed distributions of these four regions are illustrated on the histogram of the reference volume image, as shown in Fig. 3.13. Their corresponding relative estimation error e_V values are also plotted in the figure. Results suggest that the choice of the voxel intensity values for the boundary region does not affect much the estimation accuracy, when the expected wall motion region is within the chosen S_{BR}. In the case of R1, larger errors were obtained because this region excludes the intensity range of the aneurysm wall by focusing on too high intensities.

In the following, we discuss the performance comparison between a previous technique [130] for 3D independent motion estimation at specific time points (denoted as ALG1) and our proposed 4D motion cycle estimation technique (denoted as ALG2). In general, similar accuracy values could be expected using both techniques, since the plot shown in Fig. 3.7 presented comparable error values as reported in [130]. In terms of computational efficiency, the time spent for a full 4D motion estimation in this chapter is comparable to what is needed for computing only one 3D estimation at a specific time point using ALG1. In the situation with large intensity variations

in the contrast-enhanced regions in the projection images, such as inhomogeneous contrast mixing, our method or ALG2 is however expected to be more robust than ALG1. Results shown in Fig. 3.14 were obtained from the simulated inhomogeneous contrast-filled images, as described in Section 3.3.1. The relative volume error e_V was below 10% using ALG2, whereas using ALG1 it was on average 50% or even larger. This large difference is due to the fact that ALG1 failed to recover the motion from such input images. This can be visually observed in Fig. 3.14 from the surface of the ground-truth shapes at two example time instants overlaid with the estimations (i.e. maximum and minimum shape extension). Constrast inhomogeneity in this case induces an overestimation of the phantom motion using ALG1 in comparison with ALG2. This suggests that our 4D estimation is more robust to large image intensity inhomogeneity, both temporally and spatially. Additionally, a slightly higher accuracy was obtained using the projected boundary region S_{BR}. This could be possibly due to the exclusion of inner regions with inhomogeneous intensities, reducing the noise influence to the registration.

As the expected cerebral aneurysm wall motion range is very small, the impact of other possible physiological motion that might affect the motion estimation needs to be discussed. The most intuitive one is respiratory motion, however in our application its impact is negligible. First, from the clinical examination protocol point of view, the respiratory induced motion in the head is not likely to happen, given that the patient lies still, either under general anesthesia or when instructed to hold their breath for a few seconds during the 3DRA acquisition (in our case 4 s), with the head in an immobilizing headrest. Second, from our methodology point of view, we use projections from one canonical cardiac cycle that are built from multiple cardiac cycles, and we model this cycle by a 4D smooth and continuous transformation. The method assumes pseudo-periodicity in such a way that acts as a filter forcing the reconstructed motion to be just one canonical cycle. This, in effect, helps to reinforce motion induced by blood pressure changes occurring over the cardiac cycle, and meanwhile, produces an averaging of other physiological motion that does not occur with the cardiac cycle, such as respiratory motion. In fact, it works in a similar way as how standard 3DRA reconstructions ignore the existence of any kind of motion. This reference reconstruction is reliable because the potential motion is small in comparison with the size of the reconstructed objects. In our case, the estimated pseudo-periodic vascular motion should be reliable while the spontaneous irregular non-periodic motion is small in comparison with the periodic motion. These reasons can also justify the ignorance to the possible irregular variation (or large deviations) of the cardiac cycles. Recently, after following over 30 cerebral aneurysm embolization interventions we have found an intrascan heart beat variability below 1.5% on average and not exceeding 4%. This variability is small enough to be averaged or compensated by our method. Other movements throughout the rotational run that might also have an influence is related to highly attenuated structures, e.g. bones or the skull. In this case, the possibility and the amount of this motion variation are negligible, as the bone movement can be considered to be global and very small. Specifically because the skull is covering all the imaged region, its material and motion can be assumed to be homogeneous. Furthermore, this effect is minimal under our methodology

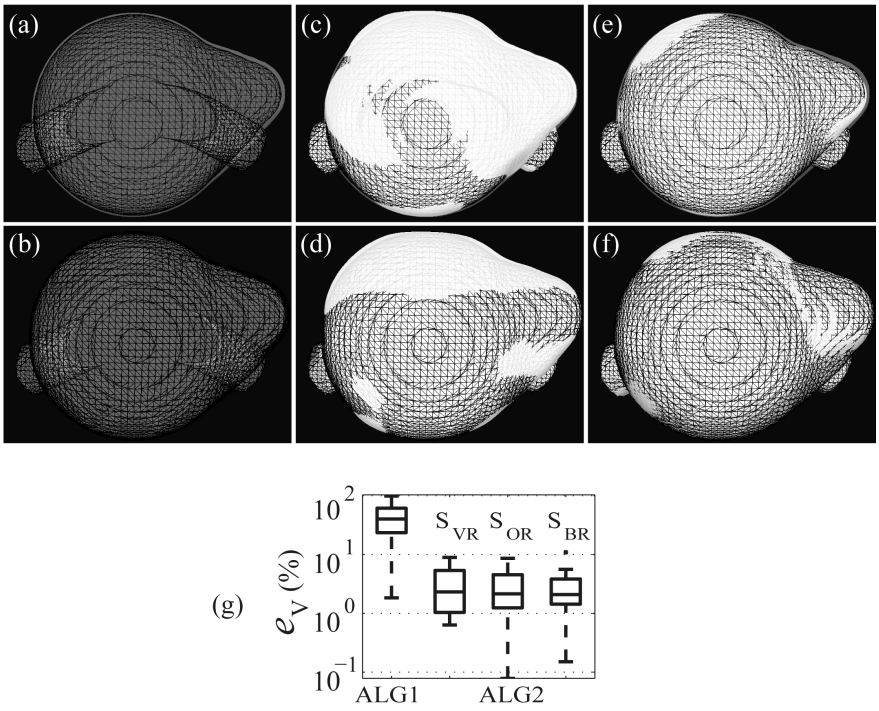

Figure 3.14: Results comparing the influence of inhomogeneous contrast filling on the method in [130] (denoted as ALG1) and our present technique (denoted as ALG2), using an *in silico* phantom with diameter of 10 mm and pulsation of 4% (i.e. maximum amplitude of 0.4 mm). Results at two instants are shown graphically: (a,c,e) minimum pulsation and (b,d,f) maximum pulsation. The ground-truth shape (*wireframe*) at each time instant is overlaid with: (a,b) the reference, (c,d) the estimation using ALG1, and (e,d) the estimation using ALG2. (g) Comparison of e_V between ALG1 and ALG2 with the three sampling regions: S_{VR}, S_{OR}, and S_{BR}. (color version on page C4)

framework, since the ray traverses through a highly contrast-enhanced object, and the projection intensity is mostly determined by the accumulated attenuation of the contrast-enhanced vessels. Therefore, the potential projection intensity variation caused by the movement of bones for a specific projection pixel can be ignored in principle. This also confirms that our acceleration strategy, the precomputation outside the region of interest is a reliable approximation. However, in the case that a substantial amount of any of the aforementioned motion occurs during the acquisition, the reliability of the estimated vascular motion could be decreased.

In general for X-ray imaging applications, the variations of intrinsic detector performance parameters could probably play a role in the image quality, as has been studied intensively in [39, 48, 76, 82, 122, 123]. These parameters can provide

characteristics that consider the complete imaging system performance, including the effect of focal spot blurring, magnification and scatter. They have more pronounced effects for general applications with less image contrast [82] or small structures like stent struts (e.g. 0.1 mm or lower) [48, 76] using a microangiographic fluoroscopic imaging system [76, 123]. In our case, the studied objects like selective CA enhanced vascular structures are imaged with high dose and are highly contrasted. Also object size is expected to be in a larger magnitude. Admittedly, the intrinsic spatial extent of the detector limits the motion recovering of our technique to a certain range. But the use of a sparse set of B-spline control points means that the estimated motion of each control point is determined by many points along the object surface and boundary. This enables us to obtain a realistic estimation of the wall motion whose magnitude is equivalent to small fractions of the total system mean imaging aperture or unsharpness. Meanwhile, note that this limited resolution of currently existing systems is expected to be improved in the future, which will enable our method to estimate even smaller motion. This factor is reflected in the results shown in Fig. 3.6 on *in silico* phantom experiments. In this figure, at least for two phantom cases (8mm and 10 mm with 1% motion for both), we were not able to recover correctly the motion. Further resolution improvements and thus motion estimation with small magnitude could be expected when geometric unsharpness effects can be minimized either through a reduction of the focal spot size or a reduction of the magnification. However, the options for a reduction of the aforementioned two factors are limited. As this study serves to show the feasibility of 4D aneurysm wall motion estimation from rotational angiography, a more detailed analysis of the impact of these factors on the estimation accuracy and robustness will be addressed in future work and is beyond the scope of this chapter.

The experimental results also emphasize the feasibility of performing strain analysis from the estimated motion, making thus possible the use of this information for further estimating elastic properties of the vascular wall, using for example an inverse problem approach [5]. Note that the strain map was not obtained through tracking individual points or tissue on the vascular wall. Thus, our approach for strain calculation through quantifying apparent motion from images implies that the correspondences over time are approximations of the same physical point.

3.6 Conclusions

This chapter has presented a technique to recover 4D cerebrovascular wall motion that is in the order of sub-millimeter, from a single 3DRA acquisition within a clinically acceptable computation time. Using this technique, the recovered motion is temporally and spatially smooth, which also improves the robustness of the estimation to noise and intensity inhomogeneity. The subsequent strain calculation based on our motion estimation provides further progress towards the biomechanical modeling of the cerebrovascular wall. Our technique also provides the possibility of detecting vascular wall abnormalities through direct visualization of motion over time. It is highly desirable to have a technique that offers accurate and robust *in vivo* estimates

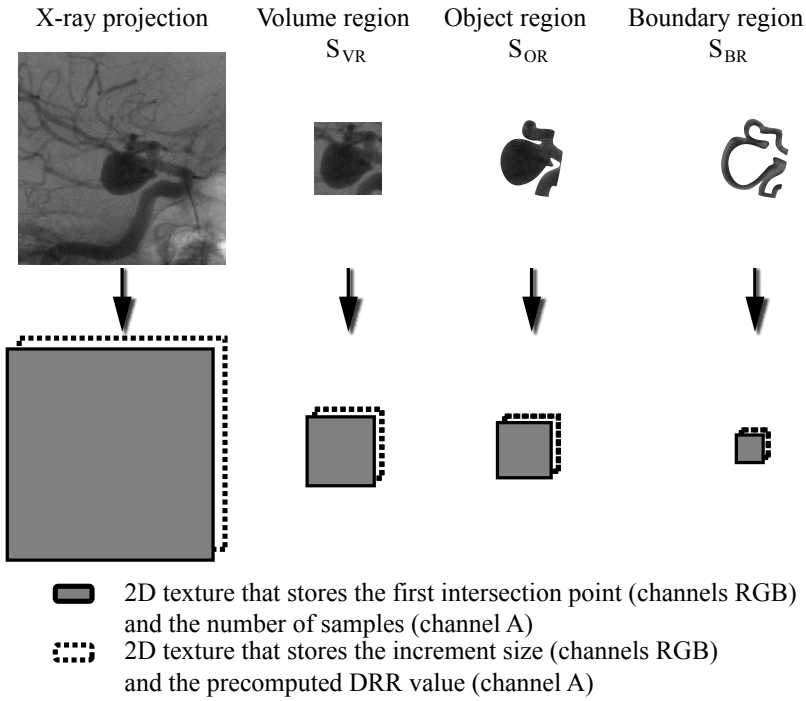

FIGURE 3.15: An illustration of how information is repacked for the final DRRs computation for the proposed three structures of interest (S_{VR}, S_{OR} and S_{BR}) into 2D textures of decreasing sizes.

of such motion. In order to translate our method into a clinical setting, future research efforts should be paid to validate our method on a larger number of patient data sets.

3.7 Appendix: GPU implementation of DRRs generation

To further speedup the method, the DRRs generation combined with the acceleration strategies is implemented on GPU and is integrated into the image registration process. We briefly describe the main idea of the method here. Unlike traditional GPU-based DRR generation methods [19], our implementation also integrates the two previously introduced strategies, thus benefits from both the GPU parallelization and the resultant memory reduction from these strategies.

The method was implemented using the Cg (C for graphics) toolkit [57] and on the pixel shader units of a NVIDIA GeForce 8600 GT graphics card with 512 MB of memory, hosted by an Intel ® Core™2 Quad CPU Q6600 2.40 GHz with 4 GB of memory. DRR pixel data are stored as stream data in the format of textures, and fed to the GPU fragment units so that each fragment works in parallel on a

single pixel. Each texture element can store up to four components, or the RGBA channels, as they are originally used to represent the red, green, blue, and alpha intensities of a color for rendering. In order to reduce redundant calculations, we compute first a number of parameters that are constant when updating the DRRs during each iteration. As we equidistantly sample points on the ray (Fig. 3.2(a)), only the first intersection point on the volume and the sampling step vector are needed, the remaining points can be derived in a straightforward manner. In total, eight constant parameters are needed for each pixel to calculate the DRRs: the first intersection point, the sampling step, the number of sampled points and the pre-computed DRR value. Since we only calculate the pixel values within the ROIs (S_{VR}, S_{OR}, or S_{BR}), these eight constant parameters to calculate the pixel values in the ROI are re-packed into two 2D rectangular textures of smaller sizes than the original projections (see an illustration in Fig. 3.15). They are used in a GPU procedure that only performs the main loop over the VOI at every registration iteration. This way, the GPU fragment code remains short to maintain the stream processing advantage with respect to its equivalent CPU calculations.

4

In-vivo Quantification of Cerebral Aneurysm Wall Motion from 3DRA and DSA

The investigation of cerebral aneurysm pulsation and vascular motion is currently challenging due to the intrinsically small motion range evaluated. This study aims at quantifying and comparing *in vivo* vascular motion estimated from 3DRA and DSA. Standard 3DRA and 30fps-DSA (with projection image resolution of 0.1mm in physical space) were used for estimating and quantifying cerebrovascular wall motion using two techniques based on image registration. Of the thirteen patients studied with saccular aneurysms, eight showed visible motion on DSA images. Wall displacements were measured at various corresponding locations on the 2D and 3D estimates. These measurements from both modalities were compared in terms of spatial range and temporal pattern. Average aneurysmal or vessel wall displacements ranges were 0.043 to 0.26 mm (3DRA) and 0.069 to 0.25 mm (DSA), respectively. There was a linear relationship (R^2=0.81) between the average estimated motion range over the cardiac cycle from these two modalities. A statistically significant correlation between both estimations on the average displacement curves over the cardiac cycle were found in 8 of the 14 measured regions. Generally, peak wall motion took place towards the end-systole and beginning of diastole. It is feasible to measure *in vivo* vascular motion with small amplitude from 3DRA and DSA using our registration-based techniques. A good spatial and temporal agreement was found between them. Such consistency suggests that the applied techniques on these modalities may be useful for quantifying cerebrovascular wall motion.

The content of this chapter is based on the publication:

Chong Zhang, Maria-Cruz Villa-Uriol, Ruben Cardenes, Vincent Costalat, Alain Bonafé, Alejandro F. Frangi, In-vivo quantification of cerebral aneurysm wall motion from 3DRA and DSA, submitted, 2011.

4.1 Introduction

The vast majority of current morphological indices used in the literature to predict growth and rupture in cerebral aneurysms [53, 69, 79, 104] such as aneurysm size, aspect ratio, neck angle, etc, do not take into account the dynamics of the vascular wall that occur during the cardiac cycle. This is because the recovery of 3D cerebral aneurysmal and vascular motion is challenging as they fall into the submillimiter range [11, 43, 45, 60, 67, 74, 106, 131]; current imaging protocols are not ready to quantify such small motion with the required spatio-temporal resolution.

While there are only limited clinical studies supporting the diagnostic value of motion data, early observations in patients have suggested the importance of examining motion information. In Steiger et al. [98], an *in vivo* hemodynamic stress study in saccular aneurysms has demonstrated that the aneurysmal wall can vibrate or pulsate, induced by the fluctuations of flow which, in a long term, contribute to aneurysm progression and eventual rupture. It has been also suggested in an *in vitro* study by Ueno et al. [103] that a decreased pulsatile aneurysmal wall movement can cause a slight reduction of the wall stress, which in turn might prevent the rupture. Meanwhile, recently in Sforza et al. [94] the authors claim that the *in vivo* oscillatory rigid rotation observed in cerebral vasculature does not have a major impact on intra-aneurysmal hemodynamic variables, and that the rigid motion of the parent arteries is unlikely to be a risk factor for aneurysm rupture. However, their simplified computational fluid dynamics simulation conditions used for this study should be taken into account when interpreting these results and the derived conclusions. Therefore, this topic remains relevant to be further studied. From a biomechanical point of view, recent research has demonstrated that localized variations in the aneurysmal wall stiffness and thickness are linked to local stress concentrations and changes in aneurysmal shape [17]. Such inhomogeneous distribution of aneurysmal wall properties may translate into inhomogeneous wall motion when exposed to varying dynamic pressures occurring during the cardiac cycle [5, 46]. Moreover, there are also studies suggesting that the direct visualization of wall motion may be helpful for analyzing pathological features of the cerebral vasculature [37, 45]. Therefore, quantitative aneurysmal wall motion could become a surrogate of vascular wall status and integrity, which could indicate vascular weakness and potentially aid the assessment of aneurysmal rupture risk.

Recent advances in imaging technologies have enabled observing aneurysmal motion with a relatively large amplitude has been observed on *in vivo* patient data using various modalities [30, 37, 43, 45, 74, 106, 124, 131]. Among them, 3DRA and DSA provide the highest spatial resolution resolution [25] and can be used intraoperatively. However, for a human operator relying solely on qualitative visual assessment, performing an objective analysis of such small motion throughout the cardiac cycle is difficult, if not impossible. As such dedicated tools in motion assessement are needed. The aim of this study was two-fold. First, to demonstrate the feasibility of quantifying wall motion, from *in vivo* data, using 3DRA through our previous 3D method [131] and using DSA through Oubel et al.'s [74] 2D method. Second, to evaluate between the estimated motion from both modalities.To the authors' knowledge, there are no

reports that quantify and correlate intracranial aneurysm and vessel motion during a cardiac cycle from 3DRA and DSA images.

4.2 Materials and methods

4.2.1 Patient selection

All patient data were collected in Neuroradiologie GDC - CHU Montpellier, France, between August and November 2010. The institutional review board gave approval for this retrospective patient study. During this period, in total 56 saccular aneurysms from 55 patients were scheduled for an aneurysm embolization. Those who underwent pretreatment 3DRA and 30fps-DSA acquisitions were of interest to us. In addition, the ECG was also recorded synchronously with these acquisitions. Therefore, the number of cases that had all the three types of data properly recorded was 13, which were included in this study. A first direct visualization of the DSA sequences was performed by three trained engineers (CZ, MV and RC) and two neuroradiologists (VC and AB). According to the majority of the observers, 10 of these patients presented visible aneurysm wall motion (AWM), parent vessel wall motion (VWM), or both. The wall motion analysis was performed on eight of these patients, excluding those not presenting visual motion, with irregular heart rate (patient #4) or overlapping with other high-contrasted objects (patient #1). Detailed information for all patients is summarized in Table 4.1. And the analyzed 3DRA and DSA images of the eight patients are shown in Fig. 4.1 and 4.2.

4.2.2 Acquisition protocol

All the acquisition procedures of the presented data were performed when the patient were under general anesthesia on a biplane angiographic unit (Allura Xper FD20/10; Philips Healthcare, Best, the Netherlands), following an institutional protocol. Patients were also intubated and mechanically ventilated. After surgical preparation of the femoral artery to gain access for the catheter and its subsequent insertion, a 3DRA scan was firstly acquired. Afterwards, the interventional neuroradiologist examined the 3D reconstruction from various angles and decided one or two view(s), where the morphology could be best visualized for planning the treatment, i.e. an ideal separation between the neck and parent artery. A 30fps-DSA acquisition was then obtained from the selected view, called the working projection view. Both recordings also included the ECG synchronized with the projections. The time lapse between these two acquisitions was in general within 5 minutes. The heart rate of the patients varied between 47 bpm and 90 bpm with an average intrascan and interscan variability below 2% (except for patient #4).

Both rotational and DSA projection images were obtained with a high frame rate of 30 fps. The active imaging field of the detector was set to 22 cm, which gave a possible combination of the largest field of view and highest pixel resolution, being 0.154 mm per side. An iodinated contrast agent (CA) was continuously injected (Ioméron 350, Bracco Imaging, France) to flow rates of up to 5 mL/s during the data

TABLE 4.1: Patient population

Patient population. Patients that showed visible vascular motion in DSA sequences were marked in bold. In the last two columns, the number of observers who observed motion is listed. (Hyp.=hypertension; H.R.=heart rate; Var.=Maximum heart rate change during the 3DRA and DSA acquisitions; Y=yes, N=no; U=Unruptured, R=Ruptured; LMCA/RMCA = Left/Right Middle Cerebral Artery, LPCoA/RPCoA = Left/Right Posterior Communicating Artery, LACA/RACA = Left/Right Anterior Cerebral Artery, ICA=Internal Carotid Artery.)

#	Sex/Age	Size (mm)	Location	Status	Hyp.	H.R. (bpm)/Var. (%)	AWM	VWM
1	F/46	$4.62 \times 4.83 \times 3.90$	LMCA	U	N	72.73/0.52	Y (3/5)	Y (3/5)
2	**M/58**	$\mathbf{6.48 \times 6.50 \times 4.54}$	**RMCA**	**U**	**N**	**82.76/2.07**	**Y (5/5)**	**Y (5/5)**
3	F/50	$5.80 \times 6.40 \times 4.25$	RMCA	R	Y	73.77/0.71	N (1/5)	N (2/5)
4	M/55	$2.39 \times 4.11 \times 3.56$	LACA	U	N	49.50/25	N (1/5)	Y (3/5)
5	**F/48**	$\mathbf{7.32 \times 5.47 \times 6.91}$	**LMCA**	**U**	**N**	**64.75/0.66**	**Y (3/5)**	**Y (4/5)**
6	**F/68**	$\mathbf{8.45 \times 9.20 \times 7.45}$	**LPCoA**	**Y**	**Y**	**59.21/0.87**	**Y (5/5)**	**Y (4/5)**
7	F/49	$6.83 \times 5.77 \times 6.09$	RACA	U	N	67.92/0.82	N (2/5)	N (1/5)
8	**F/38**	$\mathbf{7.97 \times 7.37 \times 7.08}$	**LMCA**	**U**	**N**	**47.24/1.48**	**N (2/5)**	**Y (4/5)**
9	**F/57**	$\mathbf{5.93 \times 2.65 \times 6.33}$	**LMCA**	**U**	**N**	**64.81/0.18**	**N (2/5)**	**Y (3/5)**
10	**F/26**	$\mathbf{3.10 \times 3.04 \times 2.99}$	**RACA**	**U**	**N**	**52.63/1.78**	**Y (3/5)**	**Y (4/5)**
11	**F/56**	$\mathbf{7.95 \times 3.80 \times 6.18}$	**RACA**	**R**	**N**	**90.09/1.39**	**Y (3/5)**	**Y (4/5)**
12	**F/38**	$\mathbf{6.41 \times 5.36 \times 4.63}$	**RPCoA**	**R**	**N**	**72.51/6.45**	**Y (5/5)**	**Y (5/5)**
13	M/87	$4.38 \times 6.31 \times 4.94$	LICA	R	N	69.36/0.50	N (1/5)	N (2/5)

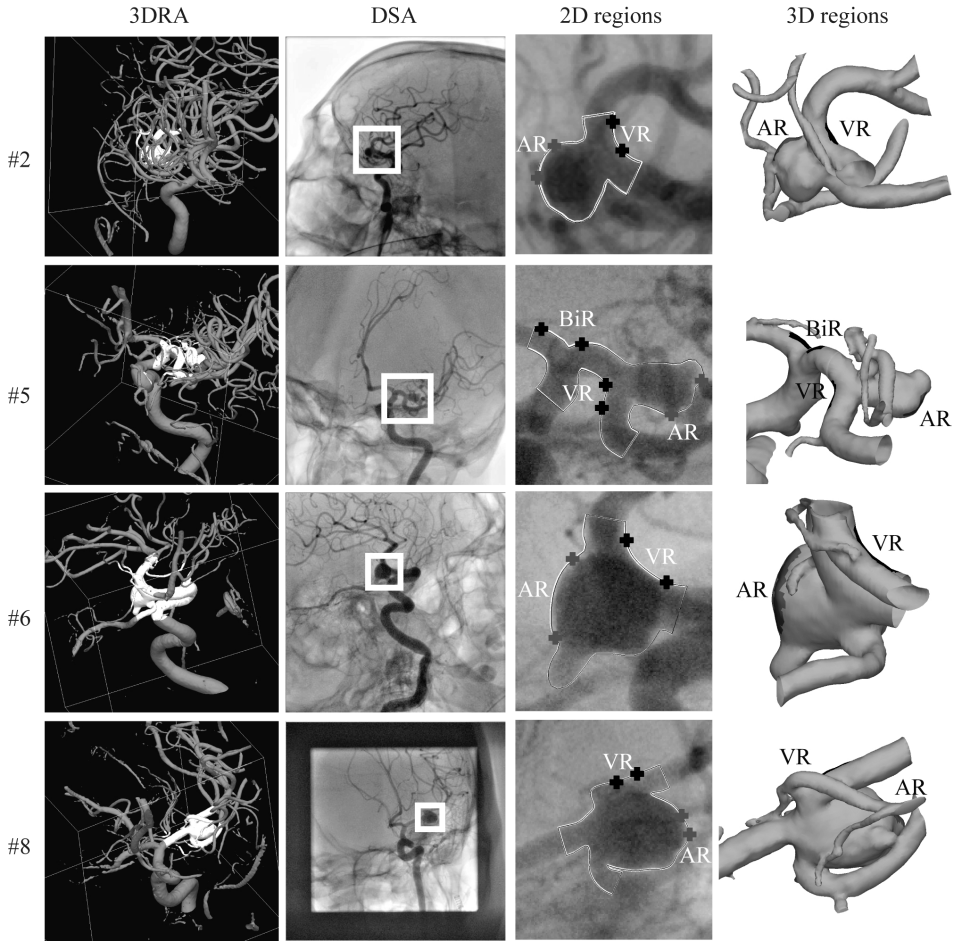

Figure 4.1: Patients #2,5,6,8: (from *left* to *right*) 3DRA data with the studied region of interest highlighted in different colors: aneurysm region (AR), vessel region (VR) and bifurcation region (BiR); one DSA image; measurement regions on 2D contour delineations (*crosses* indicate the region on the contour); measurement regions on 3D surface. (color version on page C5)

acquisitions. For all the patients in this study, the tip of the catheter was placed in the internal carotid artery. For the 3DRA imaging, 2D projections of the CA filled vessels were acquired during a continuous rotation of the C-arm over an angular span of 200° in the axial plane. To ensure proper filling of the entire vascular tree, the CA injection was started 2 or 3 s before the actual scan. The overall amount of CA used for a single rotational acquisition was 24 mL (for 2 s delay) or 35 mL (for 3 s delay).

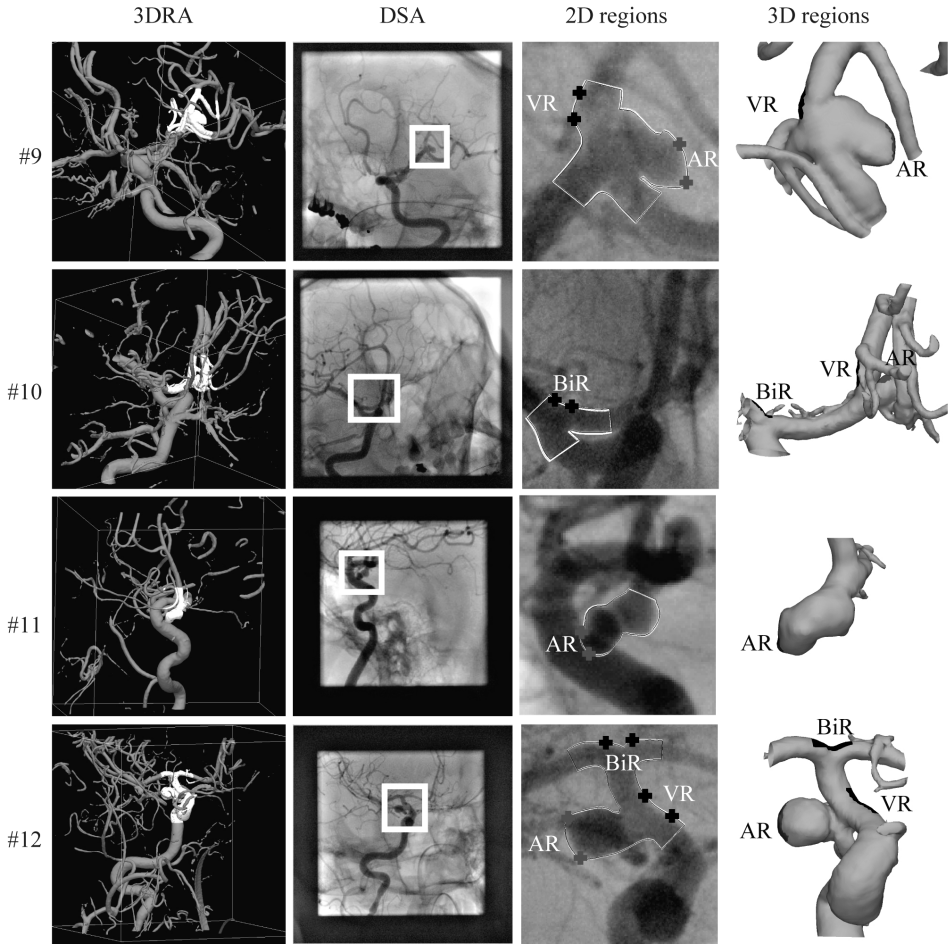

FIGURE 4.2: Patients #9,10,11,12: (from left to right) 3DRA data with the studied region of interest highlighted in different colors: aneurysm region (AR), vessel region (VR) and bifurcation region (BiR); one DSA image; measurement regions on 2D contour delineations (crosses indicate the region on the contour); measurement regions on 3D surface. (color version on page C5)

The average tube current and voltage were 261 mA and 99 kV, respectively. As for the DSA imaging, the C-arm of either the FD20 or the FD10 detector was fixed to the working projection view. The overall amount of CA used for a single DSA acquisition was 10 mL for 2 s without delay. The average tube current and voltage were 160 mA and 90 kV, respectively.

4.2.3 Wall motion estimation

For DSA images, 2D aneurysm wall motion was estimated using the technique presented in [74]. This 2D/2D registration method uses free-form deformations with *B*-spline interpolation functions and mutual information as metric. For each DSA sequence, depending on the heart rate, at least images from one full cycle were contrast enhanced. Thus, we selected one cycle that was at the middle of the acquisition, avoiding the contrast wash-in and wash-out effects. For the image frames from the selected cycle (ranging between 23 and 38 frames), a reference frame, i.e. closest to the R-peak of the ECG signal, was selected and registered to the other frames, obtaining a deformation field for each of the other frames.

For 3DRA images, 3D aneurysm wall motion was estimated using the technique presented in [131]. Detailed description of this technique is beyond the scope of this article. Briefly, motion of one canonical cardiac cycle of the cerebral vasculature was modeled using a 4D *B*-spline transformation, which was estimated from a 4D to 2D +t image registration framework. The registration was performed by optimizing a single similarity metric between the entire 2D+t measured projection sequence and the corresponding forward projections of the deformed volume at their exact time instants. At each selected time point of the cardiac cycle, a 3D volume could be obtained by deforming the reference 3DRA volume. A sequence of such estimated 3D volumes at different time instants thus can provide the 3D wall motion information.

4.2.4 Wall motion quantification

4.2.4.1 3DRA vs DSA estimation on individual patients

The aneurysmal wall in the reference DSA frame was manually delineated on the CA enhanced boundaries. Such delineation was performed on an in-house software GIMIAS (v1.3.0) [1]. For each 2D sequence, first, several landmarks were put in the reference frame along the boundaries of the studied object, i.e. aneurysm dome or vessels. These landmarks were further fitted into a spline line for the delineation. This reference contour was then propagated to the rest of the frames in the sequence by applying the estimated deformation field to it. The displacement for a boundary point was calculated by a point-to-line distance from the point at reference frame time to the contour at the selected time point.

For each volume in the 3D +t estimated sequence, a 3D surface was further extracted by thresholding using the Marching Cubes algorithm [50]. 3D displacements on the wall were calculated by a point-to-surface distance from each point on the reference surface to the one at the selected time instant.

In order to provide a fair comparison for the wall motion quantified from the estimation using the two techniques, spatial and temporal correspondences should be established between 2D+t DSA and 3D+t 3DRA images. That means, motion measurements, in our case, the wall displacement, should be taken at the same spatial locations and the same cardiac cycle time instants. Since the technique for 3DRA images is able to provide 3D instantaneous volume at any time of the cardiac cycle, the time instants for extracting the volume sequence were chosen to match the DSA frame

times at the selected cycle. The measuring locations on the 3D surface were chosen to be also projected on the boundaries in the DSA views. In order to examine local motion behavior, different regions on the wall were measured: aneurysm region (AR), adjacent vessel region (VR), and internal carotid artery (ICA) bifurcation region (BiR). The criterion for the selection of regions was to only use locations around the aneurysm where motion was more pronounced and clearly identified on both 2D contours and 3D surfaces. For example, boundaries that had overlapped vessels in 2D were discarded due to the uncertainty on the 3D surface. Therefore, not all regions were available for every patient. Fig. 4.1 and 4.2 show the selected measuring regions for each patient. In order to eliminate the difference in the measured magnitude between the two imaged space, the displacement measurements on DSA images were corrected by a geometrical magnification factor to a comparable magnitude as 3D measurements, which represents the physical size. The temporal correlation of the measurements on each region between DSA and 3DRA was calculated using the Pearson correlation coefficient (statistical significance was established with p-value$<$ 0.05).

4.2.4.2 Statistical analysis on motion pattern

To assess the correlation between measurements on different modalities, a linear regression analysis was performed between average displacements over the cardiac cycle for each region from 3DRA and DSA estimations. Bland-Altman plots were performed to assess the agreement between measurements on these two modalities. In a Bland-Altman analysis, the difference between two measurements is plotted against their average for each patient. Calculating the mean difference and the standard deviation (SD) of difference allows one to quantitatively assess how close the measurements from two different methods are to each other and how scattered they are collectively. Mean values are presented with 95% confidence intervals that were calculated for each mean SD difference value.

In [11, 68], animal or *ex vivo* experiments have shown that aneurysm pulsation follows variations in intra-aneurysmal pressure, potentially with some delay. The wall motion pattern over the cardiac cycle was also studied with our *in vivo* data. In order to establish correspondences between the motion and the cardiac events, a temporal synchronization was needed, because of the heart rate variability between patients as well as the desynchronization of the different phases of the cycle. In our case, since ECG was the only available type of physiological signal, a landmark-based piecewise linear warping was applied to ECG. After the temporal synchronization, motion curves of all the patients were mapped accordingly to the normalized timescale.

4.3 Results

4.3.1 3DRA vs DSA estimation on individual patients

The mean and SD of wall displacements measured at AR, VR and BiR over the cardiac cycle were shown as error bar plots in Fig. 4.3 and 4.4. Regions where

Table 4.2: Pearson correlation coefficient of the temporal average displacement estimates between 3DRA and DSA. Statistical significant correlation is marked in bold (p-value< 0.05).

#	Aneurysm (AR)	Vessel (VR)	Bifurcation (BiR)
2	**0.836**	**0.652**	n.a.
5	n.a.	n.a.	**0.676**
6	0.265	**0.841**	n.a.
8	0.142	0.0270	n.a.
9	**0.471**	0.145	n.a.
10	n.a.	n.a.	0.331
12	**0.545**	n.a	n.a.
13	**0.644**	**0.616**	0.247

no motion was visually observed are highlighted with a black frame. Those with a dark grey background had a statistically significant correlation between the DSA and 3DRA estimation curves. The correlation was evaluated on the temporal curve of the average displacement in each region using the Pearson correlation coefficient, as summarized in Table 4.3.1. For patient #5, the 3DRA estimation did not show any motion in AR and VR, although motion was visually detected in these regions. For patient #10, we were not able to properly delineate the contours in AR and VR from the DSA views due to vessel overlapping and inhomogeneous CA filling. In these cases, the measurements were also discarded for the correlation analysis. Thus, from the 8 patients presenting visible motion, we were able to measure estimated motion from both modalities in 14 regions. From these, 8 regions showed a statistically significant correlation between the two estimations on the average aneurysm/vessel displacement curves over the cardiac cycle.

For the presented cases, the average aneurysmal/vessel wall displacement over the cardiac cycle ranged from 0.043 mm to 0.26 mm and from 0.069 mm to 0.25 mm in 3DRA and DSA estimations, respectively. Table 4.3 lists the average and SD of motion range of each region from the 3DRA and DSA estimations. We have observed that, in general, a statistical significant correlation can be found for regions showing larger motion. And their values were similar to or larger than 0.1 mm. This value was in accordance with the projection pixel resolution (0.154 mm) after the correction of geometrical magnification (in our case about 1.5), that is, one pixel value represents about 0.1 mm in the physical space. When the motion was smaller than the imaging resolution, the correlation between the estimations from 3DRA and DSA was not clear.

4.3.2 Statistical analysis on motion pattern

The correlation between the 3DRA and DSA estimated average displacements over the cardiac cycle in all regions for all patients was analyzed by linear regression (Fig. 4.5), and there was a linear relationship ($R^2 = 0.81$). In the Bland-Altman

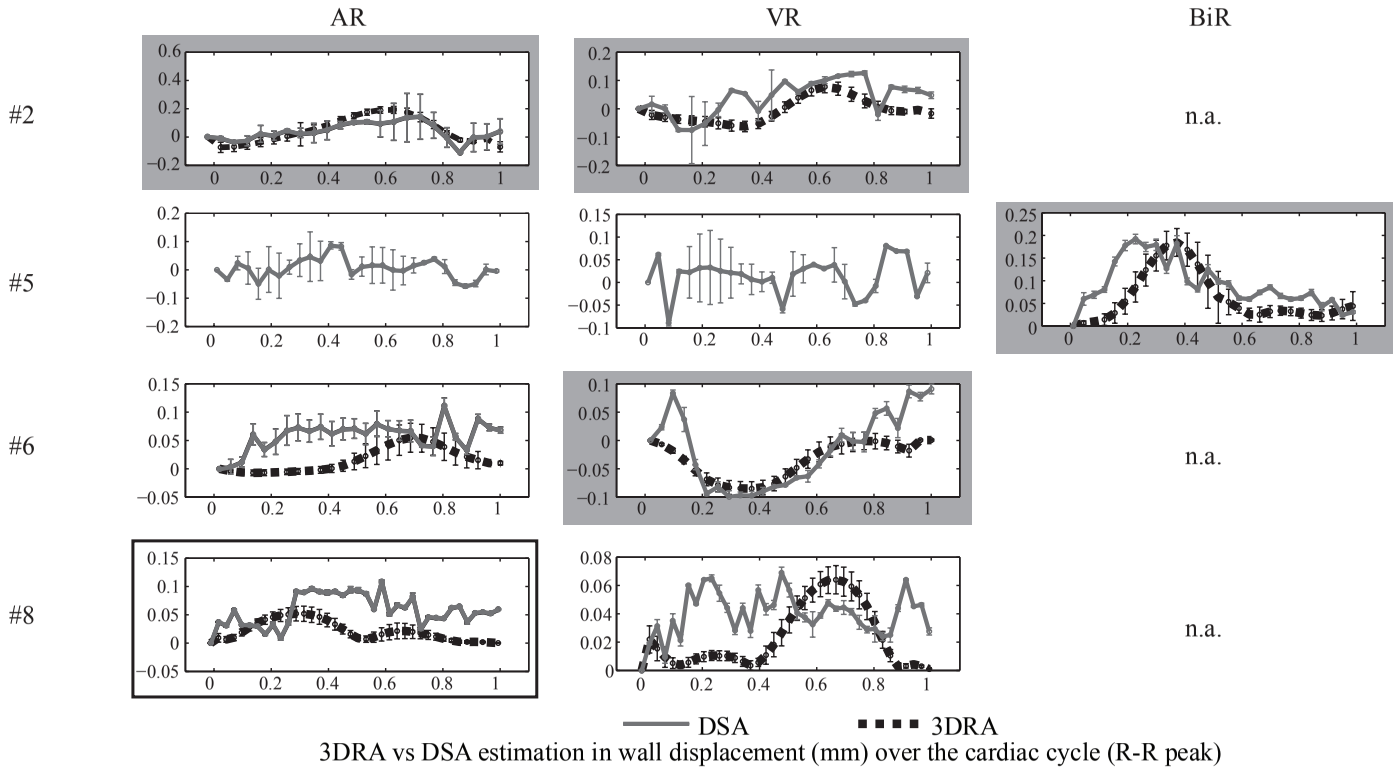

FIGURE 4.3: Wall displacements for patients #2, 5, 6, 8. Measurements were performed at AR, VR, and BiR. The error bar plots show the average and standard deviation of displacements at these regions over the cardiac cycle. The regions where no motion was visually observed are shown with a black frame, while the ones with a dark grey background, indicate a statistical significant correlation between curves.

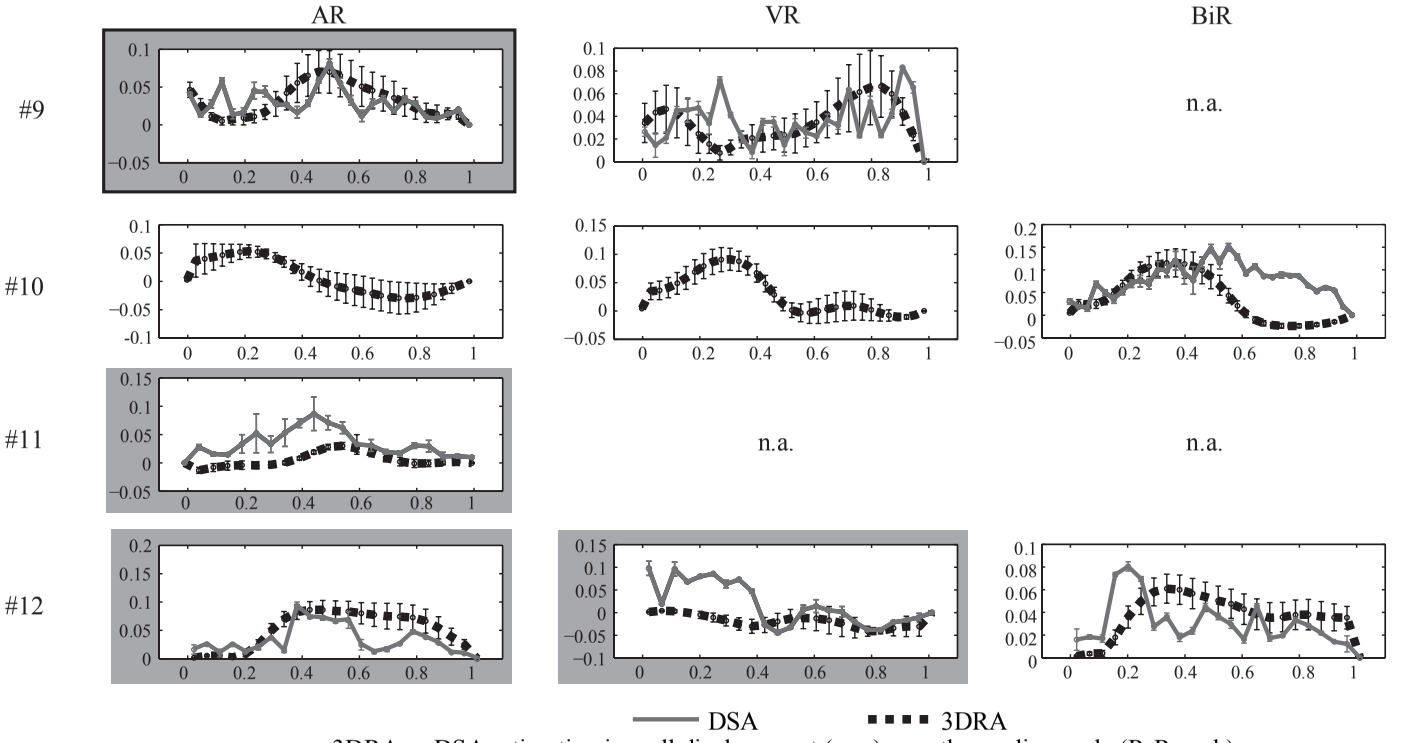

FIGURE 4.4: Wall displacements for patients #9, 10, 12, 13. Measurements were performed at AR, VR, and BiR. The error bar plots show the average and standard deviation of displacements at these regions over the cardiac cycle. The regions where no motion was visually observed are shown with a black frame, while the ones with a dark grey background, indicate a statistical significant correlation between curves.

TABLE 4.3: Mean and SD of the spatial average wall motion amplitude during the cardiac cycle. Measurements marked in bold have showed a statistical significant correlation of temporal average displacement estimates between 3DRA and DSA (see Table 4.3.1).

#	Aneurysm (AR) (mm)		Vessel (VR) (mm)		Bifurcation (BiR) (mm)	
	3DRA	DSA	3DRA	DSA	3DRA	DSA
2	$\mathbf{0.26 \pm 0.025}$	$\mathbf{0.25 \pm 0.062}$	$\mathbf{0.14 \pm 0.017}$	$\mathbf{0.20 \pm 0.022}$	n.a.	n.a.
5	n.a.	0.14 ± 0.035	n.a.	0.17 ± 0.024	$\mathbf{0.22 \pm 0.029}$	$\mathbf{0.19 \pm 0.0070}$
6	0.062 ± 0.013	0.11 ± 0.015	$\mathbf{0.086 \pm 0.011}$	$\mathbf{0.19 \pm 0.0090}$	n.a.	n.a.
8	0.052 ± 0.0080	0.11 ± 0.0030	0.064 ± 0.0060	0.069 ± 0.0030	n.a.	n.a.
9	$\mathbf{0.070 \pm 0.016}$	$\mathbf{0.081 \pm 0.0040}$	0.066 ± 0.017	0.083 ± 0.0050	n.a.	n.a.
10	0.083 ± 0.018	n.a.	0.10 ± 0.016	n.a.	0.14 ± 0.013	0.15 ± 0.0080
12	$\mathbf{0.043 \pm 0.0050}$	$\mathbf{0.087 \pm 0.011}$	n.a	n.a	n.a.	n.a.
13	$\mathbf{0.086 \pm 0.013}$	$\mathbf{0.093 \pm 0.0040}$	$\mathbf{0.045 \pm 0.015}$	$\mathbf{0.14 \pm 0.0050}$	0.061 ± 0.010	0.081 ± 0.0030

plot, mean values are presented with 95% confidence intervals calculated for each mean SD difference value. The mean difference between both measurements was -0.03 mm (SD, 0.037 mm). Therefore, 3DRA measurements were smaller than the DSA measurements by 0.03 mm on average. This suggested a close agreement, but there was also a relatively large variability in measurements indicated by the SD of 0.037 mm. These differences are at most one order of magnitude lower than the pixel resolution, being about 0.1 mm (indicated as thinner dashed line in Fig. 4.5).

Fig. 4.6 plots for each region, in all patients, the curves of average 3DRA estimated wall displacements after the application of temporal synchronization. The landmarks used were: R-peak, end S-wave, peak T-wave, end T-wave, beginning of P-wave, beginning of the QRS complex, and R-peak. Measurements from DSA estimation are not presented because they had an expected direct relationship with the 3DRA ones and lacked the temporal continuity caused by the independent registrations from one frame to another. In this figure, the motion curves were divided into two groups according to the measuring locations: right before, or at and after the ICA bifurcation, considering the potential phase delay due to the coupling between the fluid flow and wall displacement. The motion amplitude ranges were similar in both groups. Most of the peak motion occurred towards the end-systole and beginning of diastole, as indicated by ECG. It seems that for the regions measured right before or at the ICA bifurcation (Fig. 4.6 (b)), the peak motion occurred between the peak T-wave and the end T-wave. For the regions after the ICA bifurcation such as anterior and middle cerebral arteries (Fig. 4.6 (c)), it occurred at the beginning of diastole between the peak T-wave and the beginning of P-wave. This motion peak shift was in general in agreement with the order of the flow arrival time at these locations. However, there was a variability in the peak motion phases. One possible explanation for this is that, because the motion waveform is expected to follow the pattern of the intra-aneurysmal pressure waveform, which does not have a direct relationship with the ECG waveform, especially in patients with hypertension.

4.4 Discussion

We have recovered and quantified cerebral aneurysm and vascular wall motion using two image registration techniques for 3DRA and DSA images, respectively. Wall motion estimated from these two modalities has been compared in terms of spatial range and temporal pattern. Results have demonstrated the feasibility of quantifying wall motion with both 3DRA and DSA imaging (ranged between 0.04 mm to 0.26 mm) on 8 out of the 13 studied patients. This small range made the visual observation difficult and thus explains the existence of large inter-observer variability. The fact that there was no consensus among the five observers in their visual assessment of motion/no motion demonstrates the underlying challenge if motion analysis and points to the need of dedicated tools in motion assessment.

There was a linear relationship (R^2=0.81) in estimated wall displacement range between 3DRA and DSA in the presented patient data. Significant correlation on the average displacement curve was found in 8 of the 14 measured regions, and in

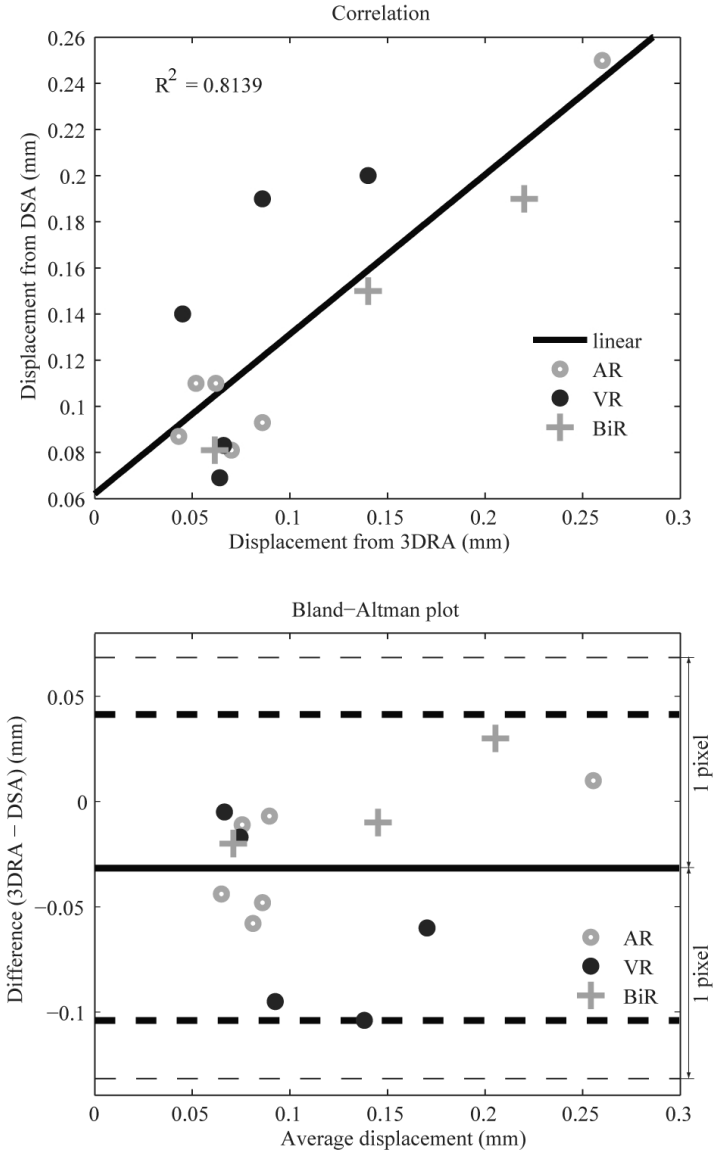

FIGURE 4.5: (*Top*) Linear correlation between average spatial motion range from 3DRA and DSA estimations ($R^2 = 0.81$). (*Bottom*) Bland-Altman plot showing the agreement between these measurements.

general their spatially-averaged motion ranges were similar to or larger than 0.1 mm,

i.e. similar to the image resolution. Remarkably, most of the peak motion occurred towards the end-systole and the beginning of diastole.

The intrinsically small motion range makes goal challenging and thus this study has several limitations. First, since the 2D technique for DSA images does not guarantee temporal consistency or continuity, the estimated motion was in general noisier than the estimation from the 3D+t technique for 3DRA images. This introduced a systematic error when analyzing the correlation between the motion obtained from both techniques. Second, the displacement measurements required a subjective selection of the measuring locations from 2D and 3D views, introducing possible sources of bias into both measurements. Third, the current imaging resolution limited the collection of patient data with wall motion. Apart from the imaging difficulties, another limiting condition was that, under general anesthesia the biomechanical behavior of the vascular wall must have been certainly lower compared to a conscious state and less prone to pulsation. This limits the number of patients with visible motion. Therefore, although we managed to collect a small amount of patient data, this number in the current study was not sufficient for rendering descriptive statistics of general motion patterns.

4.5 Conclusion

Our findings demonstrate a good spatial and temporal agreement between the wall displacements estimated from 3DRA and DSA. This consistency suggests that both motion recovery techniques may be useful for quantifying cerebrovascular wall motion. Comparably, motion estimated by the registration technique applied to 3DRA images is expected to provide more comprehensive information owing to its 3D nature as opposed to the 2D projective nature of DSA and the temporal continuity of the motion recovery algorithm. Also, it uses routinely acquired images, making it more practical for clinical application. On the other hand, the technique applied to DSA images could be beneficial for a quick analysis or for online inspection of motion during several cycles.

To our knowledge, this is the first study demonstrating the feasibility of quantification of cerebrovascular and aneurysmal wall motion in vivo from 3DRA and DSA. This study has also provided a first evaluation of regional wall motion *in vivo* with submillimiter precision and dynamic resolution. Characterization of aneurysmal wall motion in a larger patient series to understand its relationship with shape, bleb location, flow pattern and rupture events, etc., remains the subject of further investigation. Additionally, the combination of wall motion recovery with pressure measurements may be used for estimating the mechanical properties of the vascular wall *in vivo*.

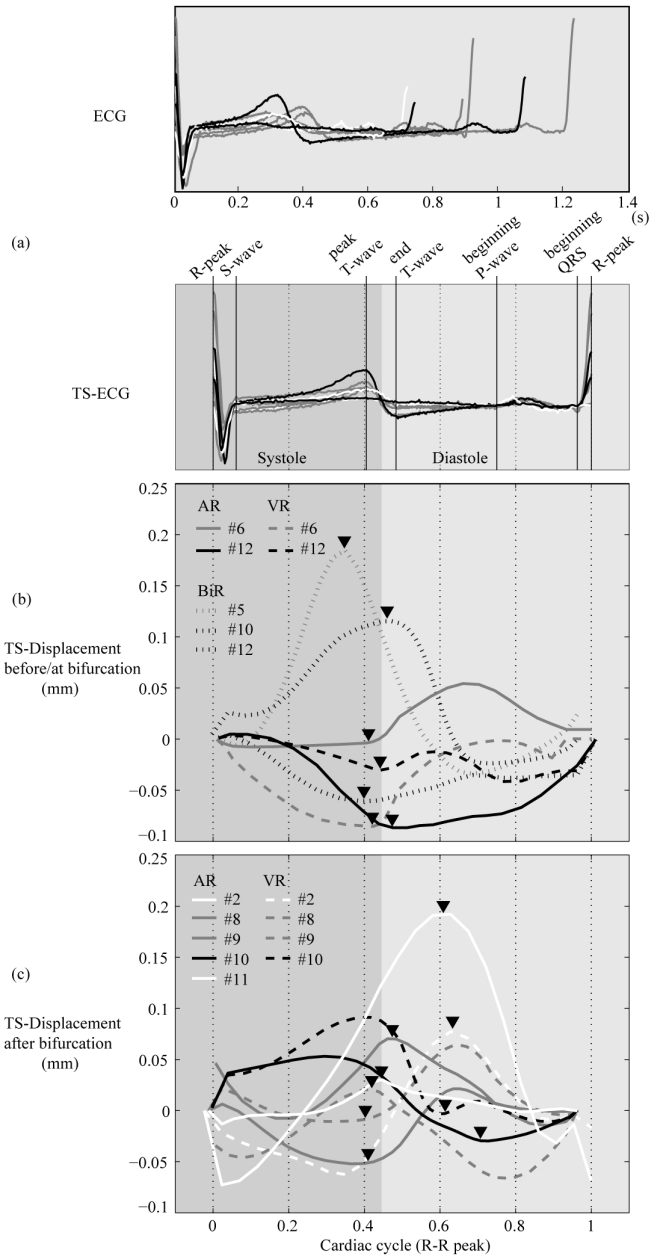

FIGURE 4.6: (a) Original ECG waveforms (R-R peak) of the eight patients and the resulting temporally synchronized ECG (TS-ECG). Synchronization landmarks are also indicated. (b,c) Motion curves of average 3DRA estimated wall displacements after applying the temporal synchronization (TS-Displacement) at regions: right before, or at and after the ICA bifurcation. Triangles indicate the peak motion. (color version on page C6)

5

Conclusions and Outlook

It was the aim of this thesis to investigate technical solutions to objectively estimate, quantify and analyze the 3D cerebral aneurysm and vascular wall motion of individual patients throughout the cardiac cycle.

This goal has been fulfilled, in the form of the following contributions:

- The development of two motion estimation methodologies for the recovery of morphodynamic information from a single 3DRA acquisition within a registration-based framework. This contribution is reported in [130, 131].
- The development of a validation framework using *in silico* and *in vitro* data, able to demonstrate performance in terms of geometry, pulsation and imaging conditions. This contribution is reported in [130, 131].
- The presentation of the first patient study that quantifies and correlates 3DRA and DSA images of *in vivo* cerebral aneurysm and vessel motion during a cardiac cycle. This contribution is reported in [129].

5.1 Conclusions

Motion estimation methodologies. In this thesis, two registration-based methodologies were proposed, both modeling wall motion through a B-spline tensor field that represented the deformation applied to the reference 3DRA volume. Our first methodology (Chapter 2) was able to estimate the aneurysm morphology at a given time instant from its temporal vicinity by matching projections of the deformed 3D reference volume to a sparse set of 2D measured projections in a weighted scheme. This approach approximated the spatiotemporal motion independently from one discrete time point to another, instead of fully addressing the intrinsic temporal consistency or continuity of motion. In addition, the estimated morphology might be compromised by the residual motion introduced by forcing the forward projections at a specific time instant to match the measured projections in its temporal vicinity. Therefore, the second methodology (Chapter 3) employed a single 4D B-spline transformation model for the whole motion cycle. The registration was optimized by measuring a single similarity metric between the entire measured projection sequence and the corresponding forward projections of the deformed volume at their corresponding exact time instants. As a result, this method improved the temporal consistency without introducing blurring, and also improved robustness to image noise and artifacts such as contrast agent induced intensity inhomogeneity.

If we compare both methodologies, while the second one is advantageous for the purpose of analyzing the whole motion pattern, the first could be equally useful when dealing with situations that focus on the morphology at specific time instants. Both techniques were tested on *in silico* and *in vitro* pulsating aneurysm phantoms that were realistic and clinically relevant in terms of geometry, pulsation and imaging conditions. In general, similar accuracy was obtained using both techniques. In the situation with large intensity variations in the contrast-enhanced regions of the projection images, such as inhomogeneous contrast mixing, the second method was more robust than the first one.

GPU-based acceleration. Computationally, both methodologies were quite expensive. This was especially relevant for the second one, where high-resolution temporal sequences of 3D images, 2D measured and forward projections had to be simultaneously processed. Therefore, during the development of the second method, the need for an acceleration algorithm became prominent. Consequently, we proposed a strategy that jointly employed precomputation and object-adaptive regions-of-interest during the DRR generation, for the sampling region of the metric computation (Chapter 3). This strategy also resulted in a reduction of memory requirements. To further speed-up the computation, it was implemented on GPU. This enabled the complete estimation of an entire motion cycle in 5-10 minutes on a standard personal computer.

Wall thickness change estimation. In Chapter 3, a geometrical measure of aneurysmal wall deformation was estimated through strain calculations. This first attempt provided a measure of the relative deformation to which the arterial wall is exposed. Such calculations could be useful to further characterize and estimate vascular wall properties such as elasticity. Note that in our approach individual tissue points on the vascular wall were not tracked, but rather apparent motion from image correspondences were quantified over time, and these were approximations of the same physical point. Thus, whether an image-based approach is adequate to characterize the vascular wall tissue remains to be investigated.

***In vivo* wall motion quantification.** Chapter 4 concluded this thesis with some examples from clinical data. These real-life examples clearly showed that this thesis work can be translated into a clinical setting. 3DRA and 30-fps DSA were used for the estimation and quantification of cerebrovascular wall motion through our second 3D+t methodology and a 2D/2D image registration techniques, respectively. From the 14 regions quantified in 8 patients, we were able to obtain average aneurysmal or vessel wall displacements below the projection image resolution. In addition, a good spatial and temporal agreement was found between them. Generally, peak motion took place towards the endsystole and beginning of diastole. To our knowledge, this is the first study able to quantify and positively correlate 3DRA and DSA images of cerebral aneurysm and vessel motion during the cardiac cycle.

To summarize, this thesis focused on the development of new methodologies to recover and quantify 3D+t wall motion from rotational projection images. To this end, the thesis work relied on the most widely used interventional technique, 3DRA, which has the highest resolution and is preferred in routine endovascular interventions. The general formulation of these techniques could potentially be adapted to other modalities as well as to estimate motion of other organs. In order to facilitate the possibility of usage in clinical practice, these techniques did not need to expose patients to additional radiation, or employing special imaging protocols. Furthermore, acceleration methods were developed to perform the motion estimation within clinically acceptable times. Despite the difficulties in collecting patient data

for evaluating and analyzing *in vivo* motion, we managed to obtain a small population of patients where the vascular wall motion was captured in the acquisitions. We were able to carry out a study to support the feasibility of our techniques to real data. And finally, we expect that the present thesis has contributed to obtaining *in vivo* wall motion in a seamlessly and user-friendly manner in the near future, especially benefiting from the expected advances in image acquisition techniques which would facilitate the capture of small motion. Consequently, we expect that the work done in this thesis will definitely contribute to further progress in this direction.

5.2 Outlook and future work

The ultimate aim of our aneurysm wall motion research is to investigate its potential correlation to growth and possible risk of rupture. The work carried out in this thesis constitutes a first step towards this aim and it has enabled extracting and quantifying motion information in the cardiac cycle from 3DRA. There still remain several unresolved issues before fulfilling this aim.

Motion pattern characterization. Wall motion pattern over the cardiac cycle has been studied on our *in vivo* data presented in Chapter 4. As has been discussed earlier, the small amount of patient data that we managed to collect in this thesis is not sufficient for rendering descriptive statistics of general motion patterns. It is therefore necessary to conduct such a prospective study on a larger series of patient data. Our hypothesis is, that the dynamic pattern of the vessel wall is influenced by anatomical position and shape; and it is also related to the hemodynamics, which is supported by previous studies. In [11, 68], animal or *ex vivo* experiments have shown that aneurysm pulsation follows variations in intra-aneurysmal pressure, potentially with some delay. Therefore, performing such a study in the future could increase the understanding of vascular mechanics and the possibility of detecting early disturbances in the vessel wall.

Estimation of mechanical properties of the vascular wall. Further studies about the biomechanical properties of cerebral aneurysms can help to elucidate the biomechanical conditions preceding rupture. With the progress in *in vivo* aneurysmal wall motion estimation we might soon expect to be able to estimate *in vivo* mechanical material properties of cerebral aneurysms [5]. Such biomechanical parameters might themselves be good predictors of vascular integrity or aneurysm rupture, and eventually become part of a more comprehensive aneurysm management pipeline [110, 111].

Morphodynamic characterization. Regions or spots presenting larger pulsation on the aneurysmal wall during the cardiac cycle could be likely candidates for possible aneurysm rupture points or areas of growth. Therefore, it should be possible to characterize the shape at different time instants using a techniques such as the moment invariants method proposed by Millán at al. [61]. After analyzing the shape at the different time instants for one patient, each of the shapes could be compared to

the precomputed shapes from other patients in a database. Based on the relationship of each shape with respect to its closest neighbors, discriminating between ruptured and unruptured aneurysms should be feasible. Such approach could be also extended to the temporal domain to help determining the potential risk of growth based on the retrieved pulsation patterns.

Combination with blood flow simulations. To date, the variable that has shown to have the largest impact on the computed flow fields is the geometry of the vascular structures [16]. Therefore, combining morphodynamic characterization with computational fluid dynamics (CFD) simulations could help to understand the effects of deforming walls on the hemodynamic patterns [18, 75]. Additionally, it could also provide more realistic intra-aneurysmal flow patterns, which in turn could help to better predict rupture risk.

Application to other vascular districts. Other possible applications in the future could be vascular motion related analysis of carotid arteries [2], aorta [92] or coronary arteries [10, 66], among others. The methodological framework developed in this thesis would probably need to be adapted to these applications, since the motion amplitude and pattern, the shape structure of the studied object, and routine imaging techniques are expected to vary greatly.

Bibliography

References

[1] Graphical Interface for Medical Image Analysis and Simulation. `http://www.gimias.org`, 2009.

[2] O. Al-Kwifi, J.K. Kim, J. Stainsby, Y. Huang, M.S. Sussman, R.I. Farb, and G.A. Wright. Pulsatile motion effects on 3D magnetic resonance angiography: Implications for evaluating carotid artery stenoses. *Magnetic Resonance in Medicine*, 52(3):605–611, 2004.

[3] J. Alastruey, K.H. Parker, J. Peiró, S.M. Byrd, and S.J. Sherwin. Modelling the Circle of Willis to assess the effects of anatomical variations and occlusions on cerebral flows. *J. Biomech.*, 40(8):1794–1805, 2007.

[4] S. Balocco, O. Camara, and A. F. Frangi. Towards regional elastography of intracranial aneurysms. In *D. Metaxas et al. (Eds.): MICCAI2008, LNCS5242*, pages 131–138, 2008.

[5] S. Balocco, O. Camara, E. Vivas, T. Sola, L. Guimaraens, H. A. F. Gratama van Adel, C. B. Majoie, J. M. Pozo, B. H. Bijnens, and A. F. Frangi. Feasibility of estimating regional mechanical properties of cerebral aneurysms in vivo. *Med. Phys.*, 37(4):1689–1706, 2010.

[6] J. Beck, S. Rohde, J. Berkefeld, V. Seifert, and A. Raabe. Aneurysm size and location of ruptured and unruptured intracranial aneurysms measured by 3-dimensional rotational angiography. *Surg. Neurol.*, 65(65):18–27, 2006.

[7] S. Benkner, A. Arbona, G. Berti, A. Chiarini, R. Dunlop, G. Engelbrecht, A.F. Frangi, C.M. Friedrich, S. Hanser, P. Hasselmeyer, R. Hose, J. Iavindrasana, M. Köhler, L. Lo Iacono, G. Lonsdale, R. Meyer, B. Moore, H. Rajasekaran, P.E. Summers, A. Wöhrer, and S. Wood. @neurIST: Infrastructure for advanced disease management through integration of heterogeneous data, computing, and complex processing services. *IEEE Trans. Inf. Technol. Biomed.*, 14(6):1365–1377, 2010.

[8] R. Bhagalia, J. A. Fessler, and B. Kim. Accelerated nonrigid intensity-based image registration using importance sampling. *IEEE Trans. Med. Imag.*, 28(8):1208–1216, 2009.

[9] C. Blondel, G. Malandain, R. Vaillant, and N. Ayache. 4D deformation field of coronary arteries from monoplane rotational X-ray angiography. In *Proc. CARS, Computer Assisted Radiology and Surgery*, volume 1256, pages 1073–1078, 2003.

[10] C. Blondel, G. Malandain, R. Vaillant, and N. Ayache. Reconstruction of coronary arteries from a single rotational X-ray projection sequence. *IEEE Trans. Med. Imag.*, 25(5):653–663, 2006.

[11] H. G. Boecher-Schwarz, K. Ringel, L. Kopacz, A. Heimann, and O. Kempski. Ex vivo study of the physical effect of coils on pressure and flow dynamics in experimental aneurysms. *Am. J. Neuroradiol.*, 21:1532–1536, 2000.

[12] H. Bogunović, A. G. Radaelli, M. DeCraene, D. Delgado, and A. F. Frangi. Image intensity standardization in 3D rotational angiography and its application to vascular segmentation. In *Proc. SPIE Med. Imag.: Image Processing*, page 691419, 2008.

[13] S. Bonnet, A. Koenig, S. Roux, P. Hugonnard, R. Guillemaud, and P. Grangeat. Dynamic X-ray computed tomography. *Proc. IEEE*, 91(10):1574–1587, 2003.

[14] J. L. Brisman, J. K. Song, and D. W. Newell. Medical progress: cerebral aneurysms. *N. Engl. J. Med.*, 355(9):928–939, 2006.

[15] V. Caselles, R. Kimmel, and G. Sapiro. Geodesic active contours. *Int. J. Comput. Vis.*, 22(1):61–79, 1997.

[16] J.R. Cebral, M.A. Castro, S. Appanaboyina, C.M. Putman, D. Millán, and A.F. Frangi. Efficient pipeline for image-based patient-specific analysis of cerebral aneurysm hemodynamics: technique and sensitivity. *IEEE Trans. Med. Imag.*, 24(4):457–467, April 2005.

[17] V. Challa and H. C. Han. Spatial variations in wall thickness, material stiffness and initial shape affect wall stress and shape of intracranial aneurysms. *Neurol. Res.*, 29(6): 569–577, 2007.

[18] L. Dempere-Marco, E. Oubel, M. Castro, C. Putman, A. F. Frangi, and J. R. Cebral. CFD analysis incorporating the influence of wall motion: application to intracranial aneurysms. In *R. Larsen, M. Nielsen, and J. Sporring (Eds.): MICCAI2006, LNCS4191*, pages 438–445, 2006.

[19] P. Després, J. Rinkel, B. Hasegawa, and S. Prevrhal. Stream processors: a new platform for Monte Carlo calculations. In F. Verhaegen, editor, *Journal of Physics: Conference Series, Third McGill International Workshop*, volume 102, page 012007, 2008.

[20] L. A. Feldkamp, L. C. Davis, and J. W. Kress. Practical cone beam algorithms. *J. Opt. Soc. Am. A*, 1:612–619, 1984.

[21] G.G. Ferguson. Physical factors in the initiation, growth and rupture of human intracranial saccular aneurysms. *J. Neurosurg.*, 37:666–677, 1972.

[22] Foundation For Aneurysm Rupture Research. http://www.ffarr.org/, 2007.

[23] M. Grass, R. Koppe, E. Klotz, R. Proksa, M.H. Kuhn, H. Aerts, J. Op de Beek, and R. Kemkers. 3D reconstruction of high contrast objects using C-arm image intensifier projection data. *Comput. Med. Imag. Graph.*, 23:311–321, 1999.

[24] M.V. Green, J. Seidel, S.D. Stein, T.E. Tedder, K.M. Kempner, C. Kertzman, and T.A. Zeffiro. Head movement in normal subjects during simulated PET brain imaging with and without head restraint. *J. Nucl. Med.*, 35(9):1538–1546, September 1994.

[25] L. Hacein-Bey and J. M. Provenzale. Current imaging assessment and treatment of intracranial aneurysms. *Am. J. Roentgenol.*, 196:32–44, 2011.

[26] G.J. Hademenos, T.F. Masssoud, F. Turjman, and J.W. Sayre. Anatomical and morphological factors correlating with rupture of intracranial aneurysms in patients referred for endovascular treatment. *Neuroradiology*, 40:755–760, 1988.

[27] E. Hansis, D. Schäfer, O. Dössel, and M. Grass. Projection-based motion compensation for gated coronary artery reconstruction from rotational x-ray angiograms. *Phys. Med. Biol.*, 53(14):3807–20, 2008.

[28] T. Hassan, E.V. Timofeev, T. Saito, H. Shimizu, M. Ezura, Y. Matsumoto, K. Takayama, T. Tominaga, and A. Takahashi. A proposed parent vessel geometry-based categorization of saccular intracranial aneurysms: computational flow dynamics analysis of the risk factors for lesion rupture. *J. Neurosurg.*, 103:662–680, 2005.

[29] M. Hayakawa, K. Katada, H. Anno, and et al. Imaging of cerebral aneurysm pulsation with ECG gated CT: Possible usefulness in the identification of aneurysmal rupture region. In *Proc. of American Society of Neuroradiology 40th Annual Meeting*, page 272, 2002.

[30] M. Hayakawa, K. Katada, H. Anno, S. Imizu, J. Hayashi, K. Irie, M. Negoro, Y. Kato, T. Kanno, and H. Sano. CT angiography with electrocardiographically gated reconstruction for visualizing pulsation of intracranial aneurysms: identification of aneurysmal protuberance presumably associated with wall thinning. *Am. J. Neuroradiol.*, 26:1366–1369, 2005.

[31] P. A. Heidenreich, J. G. Trogdon, O. A. Khavjou, J. Butler, K. Dracup, M. D. Ezekowitz, E. A. Finkelstein, Y. Hong, S. C. Johnston, A. Khera, D. M. Lloyd-Jones, S. A. Nelson, G. Nichol, D. Orenstein, P. W. F. Wilson, Y. J. Woo, and on behalf of the American Heart Association Advocacy Coordinating Committee, and Stroke Council, and Council on Cardiovascular Radiology and Intervention, and Council on Clinical Cardiology, and Council on Epidemiology and Prevention, and Council on Arteriosclerosis, and Thrombosis and Vascular Biology, and Council on Cardiopulmonary, and Critical Care, and Perioperative and Resuscitation, and Council on Cardiovascular Nursing, and Council on the Kidney in Cardiovascular Disease, and Council on Cardiovascular Surgery and Anesthesia, and Interdisciplinary Council on Quality of Care and Outcomes Research. Forecasting the future of cardiovascular disease in the United States: A policy statement from the American Heart Association. *Circulation*, 123(8):933–944, 2011.

[32] J.H. Hipwell, G.P. Penney, R.A. McLaughlin, K. Rhode, P. Summers, T.C. Cox, J.V. Byrne, J.A. Noble, and D.J. Hawkes. Intensity-based 2D-3D registration of cerebral angiograms. *IEEE Trans. Med. Imag.*, 22(11):1417–1426, 2003.

[33] M. Holden, J. A. Schnabel, and D. L. G. Hill. Quantification of small cerebral ventricular volume changes in treated growth hormone patients using nonrigid registration. *IEEE Trans. Med. Imag.*, 21(10):1292–1301, 2002.

[34] J.U. Howington, S.C. Kutz, G.E. Wilding, and D. Awasthi. Cocaine use as a predictor of outcome in aneurysmal subarachnoid hemorrhage. *J. Neurosurg.*, 99:271–275, 2003.

[35] J. Huang and J. M. van Gelder. The probability of sudden death from rupture of intracranial aneurysms: a meta-analysis. *J. Neurosurg.*, 51(5):1101–1105, 2002.

[36] IEEE. IEEE standard for floating-point arithmetic. *IEEE Std 754-2008*, pages 1–58, 2008.

[37] F. Ishida, H. Ogawa, T. Simizu, T. Kojima, and W. Taki. Visualizing the dynamics of cerebral aneurysms with four-dimensional computed tomographic angiography. *Neurosurgery*, 57(3):460–471, 2005.

[38] F. Jacobs, E. Sunderman, B.D. Sutter, M. Christiaens, and I. Lemahieu. A fast algorithm to calculate the exact radiological path through a pixel or voxel space. *J. Comput. Inform. Tech.*, 6:89–94, 1998.

[39] A. Jain, A. T. Kuhls-Gilcrist, S. K. Gupta, D. R. Bednarek, and S. Rudin. Generalized two-dimensional (2D) linear system analysis metrics (GMTF, GDQE) for digital radiography systems including the effect of focal spot, magnification, scatter, and detector characteristics. In *Proc. SPIE Med. Imag.: Physics of Medical Imaging*, page 76220K, 2010.

[40] S. Juvela. Prehemorrhage risk factors for fatal intracranial aneurysm rupture. *Stroke*, 34:1852–1858, 2003.

[41] S. Juvela, M. Porras, and K. Poussa. Natural history of unruptured intracranial aneurysms: probability of and risk factors for aneurysm rupture. *J. Neurosurg.*, 93:379–387, 2000.

[42] S. Juvela, J. Siironen, and J. Kuhmonen. Hyperglycemia, excess weight, and history of hypertension as risk factors for poor outcome and cerebral infarction after aneurysmal subarachnoid hemorrhage. *J. Neurosurg.*, 102:998–1003, 2005.

[43] C. Karmonik, O. Diaz, R. Grossman, and R. Klucznik. In-vivo quantification of wall motion in cerebral aneurysms from 2D cine phase contrast magnetic resonance images. *Rofo. Fortschr Röntgenstr*, 182(2):140–150, 2010.

[44] Y. Kato, M. Hayakawa, H. Sano, M. V. Sunil, S. Imizu, M. Yoneda, S. Watanabe, M. Abe, and T. Kanno. Prediction of impending rupture in aneurysms using 4D-CTA: histopathological verification of a real-time minimally invasive tool in unruptured aneurysms. *Minim. Invasive Neurosurg.*, 47:131–135, 2004.

[45] T. Krings, P. Willems, J. Barfett, M. Ellis, N. Hinojosa, J. Blobel, and S. Geibprasert. Pulsatility of an intracavernous aneurysm demonstrated by dynamic 320-detector row CTA at high temporal resolution. *Cent. Eur. Neurosurg.*, 70:214–218, 2009.

[46] M. Kroon and G. A. Holzapfel. Estimation of the distributions of anisotropic, elastic properties and wall stresses of saccular cerebral aneurysms by inverse analysis. *Proc. R. Soc. A*, 464:807–825, 2008.

[47] J. Kybic and M. Unser. Fast parametric elastic image registration. *IEEE Trans. Signal. Proces.*, 12(11):1427–1442, 2003.

[48] I. S. Kyprianou, S. Rudin, D. R. Bednarek, and K. R. Hoffmann. Generalizing the MTF and DQE to include x-ray scatter and unsharpness: Application to a new microangiographic system. *Med. Phys.*, 32(2):613–626, 2005.

[49] J. C. Lasheras. The biomechanics of arterial aneurysms. *Annu. Rev. Fluid. Mech.*, 39:293–319, 2007.

[50] W.E. Lorensen and H.E. Cline. Marching cubes: A high resolution 3D surface construction algorithm. In *SIGGRAPH '87: Proceedings of the 14th annual conference on Computer graphics and interactive techniques*, pages 163–169, New York, NY, USA, 1987. ACM Press.

[51] L. A. Love and R. A. Kruger. Scatter estimation for a digital radiographic system using convolution filtering. *Med. Phys.*, 14(2):178–185, 1987.

[52] M. Löw, K. Perktold, and R. Raunig. Hemodynamics in rigid and distensible saccular aneurysms: a numerical study of pulsatile flow characteristics. *Biorheology*, 30:287–298, 1993.

[53] B. Ma, R.E. Hargaugh, and M.L. Raghavan. Three-dimensional geometrical characterization of cerebral aneurysms. *Ann. Biomed. Eng.*, 32(2):264–273, February 2004.

[54] F. Maes, A. Collignon, D. Vandermeulen, G. Marchal, and P. Suetens. Multimodality image registration by maximization of mutual information. *IEEE Trans. Med. Imag.*, 16(2):187–198, 1997.

[55] W.I. Mangrum, J. Huston III, M.J. Link, D.O. Wiebers, R.L. McGlelland, T.J.H. Christianson, and K.D. Flemming. Enlarging vertebrobasilar nonsaccular intracranial aneurysms: frequency, predictors, and clinical outcome of growth. *J. Neurosurg.*, 102:72–79, 2005.

[56] R. Manzke, M. Grass, and D. Hawkes. Artifact analysis and reconstruction improvement in helical cardiac cone beam CT. *IEEE Trans. Med. Imag.*, 23(9):1150–1164, 2004.

[57] W. R. Mark, R. S. Glanville, K. Akeley, and M. J. Kilgard. Cg: A system for programming graphics hardware in a C-like language. *ACM Trans. Graphics*, 22(3): 896–907, 2003.

[58] D. Mattes, D. R. Haynor, H. Vesselle, T. K. Lewellen, and W. Eubank. PET-CT image registration in the chest using free-form deformation. *IEEE Trans. Med. Imag.*, 22(1):120–128, 2003.

[59] R. McGill, J.W. Tukey, and W.A. Larsen. Variations of boxplots. *American Statistician*, 32:12–16, 1978.

[60] F. B. Meyer, J. Huston III, and S. S. Riederer. Pulsatile increases in aneurysm size determined by cine phase-contrast MR angiography. *J. Neurosurg.*, 78(6):879–883, 1993.

[61] R.D. Millán, L. Dempere-Marco, J.M. Pozo, J.R. Cebral, and A.F. Frangi. Morphological characterization of intracranial aneurysms using 3D moment invariants. *IEEE Trans. Med. Imag.*, 26(9):1270–1282, 2007.

[62] A. Molyneux, R. Kerr, I. Stratton, P. Sandercock, M. Clarke, and J. Shrimpton R. Holman. International Subarachnoid Aneurysm Trial (ISAT) of neurosurgical clipping versus endovascular coiling in 2143 patients with ruptured intracranial aneurysms: a randomised trial. *Lancet*, 360:1267–1274, 2002.

[63] A. Morita, S. Fujiwara, K. Hashi, H. Ohtsu, and T. Kirino. Risk of rupture associated with intact cerebral aneurysms in the Japanese population: a systematic review of the literature from Japan. *J. Neurosurg.*, 102:601–606, 2005.

[64] B. Movassaghi, M. Grass, D. Schaefer, V. Rasche, O. Wink, G. Schoonenberg, J. Y. Chen, J. A. Garcia, B. M. Groves, J. C. Messenger, and J. D. Carroll. 4D coronary artery reconstruction based on retrospectively gated rotational angiography: first in-human results. In *Proc. SPIE Med. Imag.: Visualization and Image-Guided Procedures*, volume 6509, page 65090P, 2007.

[65] A. Nader-Sepahi, M. Casimiro, J. Sen, and et al. Is aspect ratio a reliable predictor of intracranial aneurysm rupture? *Neurosurgery*, 54:1343–1348, 2004.

[66] A. M. Neubauer, J. A. Garcia, J. C. Messenger, E. Hansis, M. S. Kim, A. J. P. Klein, G. A. F. Schoonenberg, M. Grass, and J. D. Carroll. Clinical feasibility of a fully automated 3D reconstruction of rotational coronary X-ray angiography. *Circ. Cardiovasc. Interv.*, 3:71–79, 2010.

[67] T. Nishida, M. Kinoshita, H. Tanaka, T. Fujinaka, and T. Yoshimine. Quantification of cerebral artery motion during the cardiac cycle. *Am. J. Neuroradiol.*, 2011. in press.

[68] P. Novak, R. Glikstein, and G. Mohr. Pulation-pressure relationship in experimental aneurysms: observation of aneurysmal hysteresis. *Neurol. Res.*, 18:377–382, 1996.

[69] International Study of Unruptured Intrancranial Aneurysms Investigators. Unruptured intracranial aneurysms–risk of rupture and risks of surgical intervention. *N. Engl. J. Med.*, 339:1725–1733, 1998.

[70] International Study of Unruptured Intrancranial Aneurysms Investigators. Unruptured intracranial aneurysms: natural history, clinical outcome, and risks of surgical and endovascular treatment. *Lancet*, 362:103–110, 2003.

[71] World Health Organization. The global burden of disease: 2004 update, 2008.

[72] M. Oshima, K. Takagi, and Y. Ichijo. Numerical investigation of geometric effects on hemodynamics of cerebral artery using deformable model. In *2003 Summer Bioengineering Conference*, pages 783–784, Florida, 2003.

[73] N. Otsu. A threshold selection method from gray-level histograms. *IEEE Trans. Syst. Man. Cybern*, 9:62–66, 1979.

[74] E. Oubel, J. R. Cebral, M. DeCraene, R. Blanc, J. Blasco, J. Macho, C. M. Putman, and A. F. Frangi. Wall motion estimation in intracranial aneurysms. *Physiol. Meas.*, 31:1119–1135, 2010.

[75] E. Oubel, M. DeCraene, C. Putman, J. R. Cebral, and A. F. Frangi. Analysis of intracranial aneurysm wall motion and its effects on hemodynamic patterns. In *Proc. SPIE Med. Imag.: Physiology, Function, and Structure from Medical Images*, page 65112A, 2007.

[76] V. Patel, K. R. Hoffmann, C. N. Ionita, C. Keleshis, D. R. Bednarek, and S. Rudin. Rotational micro-CT using a clinical C-arm angiography gantry. *Med. Phys.*, 35(10): 4757–4764, 2008.

[77] B. Perrenot, R. Vaillant, R. Prost, G. Finet, P. Douek, and F. Peyrin. Motion correction for coronary stent reconstruction from rotational X-ray projection sequences. *IEEE Trans. Med. Imag.*, 26(10):1412–1423, 2007.

[78] T.W. Raaymakers, G.J. Rinkel, M. Limburg, and A. Algra. Mortality and morbidity of surgery for unruptured intracranial aneurysms: a meta-analysis. *Stroke*, 29:1531–1538, 1998.

[79] M.L. Raghavan, B. Ma, and R.E. Harbaugh. Quantified aneurysm shape and rupture risk. *J. Neurosurg.*, 102:355–362, 2005.

[80] V. Rasche, B. Movassaghi, M. Grass, D. Schäfer, and A. Bücker. Automatic selection of the optimal cardiac phase for gated three-dimensional coronary X-ray angiography. *Acad. Radiol.*, 13(5):630–640, 2006.

[81] V. Rasche, B. Movassaghi, M. Grass, D. Schäfer, H. P. Kühl, R. W. Günther, and A. Bücker. Three-dimensional X-ray coronary angiography in the porcine model: a feasibility study. *Acad. Radiol.*, 13(5):644–651, May 2006.

[82] V. Rasche, B. Schreiber, C. Graeff, T. Istel, H. Schomberg, M. Grass, R. Koppe, E. Klotz, and G. Rose. Performance of image intensifier-equipped X-ray systems for three-dimensional imaging. In *Proc. CARS, Computer Assisted Radiology and Surgery*, volume 1256, pages 187–192, 2003.

[83] G.J. Rinkel, M. Djibuti, A. Algra, and J. van Gijn. Prevalence and risk of rupture of intracranial aneurysms: a systematic review. *Stroke*, 29:251–256, 1998.

[84] C. Rohkohl, G. Lauritsch, L. Biller, M. Prümmer, J. Boese, and J. Hornegger. Interventional 4D motion estimation and reconstruction of cardiac vasculature without motion periodicity assumption. *Med. Image Anal.*, 14:687–694, 2010.

[85] D. Rueckert, L. I. Sonoda, C. Hayes, D. L. G. Hill, M. O. Leach, and D. J. Hawkes. Non-rigid registration using free-form deformations: application to breast MR images. *IEEE Trans. Med. Imag.*, 18(8):712–721, 1999.

[86] S.M. Russeli, K. Lin, S.A. Hahn, and J.J. Jafar. Smaller cerebral aneurysms producing more extensive subarachnoid hemorrhage following rupture: a radiological investigation and discussion of theoretical determinants. *J. Neurosurg.*, 99:248–253, 2003.

[87] M. R. Sabuncu and P. J. Ramadge. Gradient based nonuniform subsampling for information-theoretic alignment methods. In *Proc. Int. Conf. IEEE Eng. Med. Biol. Soc.*, volume 3, pages 1683–1686, 2004.

[88] D. Schäfer, J. Börgert, V. Rasche, and M. Grass. Motion-compensated and gated cone beam filtered back-projection for 3-D rotational X-ray angiography. *IEEE Trans. Med. Imag.*, 25(7):898–906, 2006.

[89] W. Schievink. Intracranial aneurysms. *N. Engl. J. Med.*, 336:28–41, 1997.

[90] W.I. Schievink. Genetics and aneurysm formation. *Neurosurg. Clin. N. Am.*, 9(3): 485–495, 1998.

[91] W.I. Schievink, D.J. Schaid, H.M. Rogers, and et al. On the inheritance of intracranial aneurisms. *Stroke*, 25:2028–2037, 1994.

[92] E. Schwartz, R. Gottardi, J. Holfeld, C. Loewe, M. Czerny, and G. Langs. Evaluating deformation patterns of the thoracic aorta in gated CTA sequences. In *Biomedical Imaging: From Nano to Macro, 2010 IEEE International Symposium on*, pages 21 – 24, april 2010.

[93] P. Seshaiyer and J.D. Humphrey. On the potentially protective role of contact constraints on saccular aneurysms. *J. Biomech.*, 34:607–612, 2001.

[94] D. M. Sforza, R. Löhner, C. Putman, and J. R. Cebral. Hemodynamic analysis of intracranial aneurysms with moving parent arteries: Basilar tip aneurysms. *Int. J. Numer. Meth. Biomed. Engng.*, 26:1219–1227, 2010.

[95] D. M. Sforza, C. M. Putman, and J. R. Cebral. Hemodynamics of cerebral aneurysms. *Annu. Rev. Fluid. Mech.*, 41:91–107, 2009.

[96] R. L. Siddon. Fast calculation of the exact radiological path for a three-dimensional CT array. *Med. Phys.*, 12(2):252–255, 1985.

[97] M. Sluzewski, J.A. Bosch, W.J. van Rooij, P.C. Nijssen, and D. Wijnalda. Rupture of intracranial aneurysms during treatment with Guglielmi detachable coils: Incidence, outcome, and risk factors. *J. Neurosurg.*, 94:238–240, 2001.

[98] H. J. Steiger and H. J. Reulen. Low frequency flow fluctuations in saccular aneurysms. *Acta Neurochir.*, 83:131–137, 1986.

[99] C.L. Taylor, Z. Yuan, W.R. Selman, R.A. Ratcheson, and A.A.Rimm. Cerebral arterial aneurysm formation and rupture in 20,767 elderly patients: hypertension and other risk factors. *J. Neurosurg.*, 83:812–819, 1995.

[100] P. Thevenaz and M. Unser. Spline pyramids for inter-modal image registration using mutual information. In *Proc. SPIE Wavelet Applications in Signal and Image Processing V*, volume 3169, pages 236–247, 1997.

[101] D. Tomaževič, B. Likar, and F. Pernuš. 3D/2D image registraion: the impact of X-ray views and their number. In *MICCAI*, pages 450–457, 2007.

[102] R. Torii, M. Oshima, T. Kobayashi, K. Takagi, and T. E. Tezduyar. Fluid-structure interaction modeling of aneurysmal conditions with high and normal blood pressures. *Comput. Mech.*, 38:482–490, 2006.

[103] J. Ueno, T. Matsuo, K. Sugiyama, and R. Okeda. Mechanism underlying the prevention of aneurismal rupture by coil embolization. *J. Med. Dent. Sci.*, 49:135–141, 2002.

[104] H. Ujiie, H. Tachibana, O. Hiramatsu, A.L. Hazel, T. Matsumoto, Y. Ogasawara, H. Nakajima, T. Hori, K. Takakura, and F. Kajiya. Effects of size and shape (aspect ratio) on the hemodynamics of saccular aneurysms: a possible index for surgical treatment of intracranial aneurysms. *Neurosurgery*, 45(1):119–130, 1999.

[105] H. Ujiie, H. Tamano, K. Sasaki, and T. Hori. Is the aspect ratio a reliable index for predicting the rupture of saccular aneurysms? *Neurosurgery*, 48(3):495–503, 2001.

[106] Y. Umeda, F. Ishida, K. Hamada, K. Fukazawa, Y. Miura, N. Toma, H. Suzuki, S. Matsushima, S. Shimosaka, and W. Taki. Novel dynamic four-dimensional CT angiography revealing 2-type motions of cerebral arteries. *Stroke*, 42:815–818, 2011.

[107] M. Unser. Splines: a perfect fit for signal and image processing. *IEEE Signal Process. Mag.*, 16(6):22–38, 1999.

[108] A. Valencia and F. Solis. Blood flow dynamics and arterial wall interaction in a saccular aneurysm model of basilar artery. *Comput. Struct.*, 84:1326–1337, 2006.

[109] J. Vandemeulebroucke, J. Kybic, P. Clarysse, and D. Sarrut. Respiratory motion estimation from cone-beam projections using a prior model. In *G.-Z. Yang et al. (Eds.): MICCAI2009, LNCS5762*, pages 365–372, 2009.

[110] M.-C. Villa-Uriol, G. Berti, D.R. Hose, A. Marzo, A. Chiarini, J. Penrose, J. Pozo, J.G. Schmidt, P. Singh, R. Lycatt, I. Larrabide, and A. F. Frangi. @neurIST complex information processing toolchain for the integrated management of cerebral aneurysms. *Interface Focus*, 1:308–319, 2011.

[111] M.-C. Villa-Uriol, I. Larrabide, J. M. Pozo, M. Kim, O. Camara, M. De Craene, C. Zhang, A. J. Geers, H. Morales, H. Bogunović, R. Cárdenes, and A. F. Frangi. Toward integrated management of cerebral aneurysms. *Phil. Trans. R. Soc. A*, 368:2961–2982, 2010.

[112] M.-C. Villa-Uriol, I. Larrabide, J. M. Pozo, M. Kim, M. De Craene, O. Camara, C. Zhang, A. J. Geers, H. Morales, H. Bogunović, and A. F. Frangi. *Computational Vision and Medical Image Processing: Recent Trends*, volume 19 of *Computational Methods in Applied Sciences*, chapter Cerebral Aneurysms: A Patient-Specific and Image-Based Management Pipeline, pages 327–349. Springer Science+Business Media B.V., 2011.

[113] P. Viola and W. M. Wells. Alignment by maximization of mutual information. *Int. J. Comput. Vision*, 24(2):137–154, 1997.

[114] J. M. Wardlaw, J. Cannon, P. F. Statham, and R. Price. Does the size of intracranial aneurysms change with intracranial pressure? Observations based on color "power" transcranial Doppler ultrasound. *J. Neurosurg.*, 88(5):846–50, May 1998.

[115] J. M. Wardlaw and J. C. Cannon. Color transcranial "power" Doppler ultrasound of intracranial aneurysms. *J. Neurosurg.*, 84(3):459–461, 1996.

[116] J. M. Wardlaw and P. M. White. The detection and management of unruptured intracranial aneurysms. *Brain*, 123:205–221, 2000.

[117] R. K. Warriner, K. W. Johnston, and R. S. C. Cobbold. A viscoelastic model of arterial wall motion in pulsatile flow: implications for Doppler ultrasound clutter assessment. *Physiol. Meas.*, 29:157–179, 2008.

[118] J. Weese, T.M. Buzug, G.P. Penney, and P. Desmedt. 2D/3D registration and motion tracking for surgical interventions. *Philips J. Res.*, 51:299–316, 1998.

[119] M. Winslow, X. G. Xu, and B. Yazici. Development of a simulator for radiographic image optimization. *Comput. Meth. Programs Biomed.*, 78:179–190, 2005.

[120] D. Woo and J. Broderick. Genetics of intracranial aneurysm. *J. Stroke Cerebrovasc. Dis.*, 11(5):230–240, 2002.

[121] D. Xia, L. Yu, E. Y. Sidky, Y. Zou, N. Zuo, and X. Pan. Noise properties of chord-image reconstruction. *IEEE Trans. Med. Imag.*, 26(2):1328–1344, 2007.

[122] G. K. Yadava, I. S. Kyprianou, S. Rudin, D. R. Bednarek, and K. R. Hoffmann. Generalized two-dimensional (2D) linear system analysis metrics (GMTF, GDQE) for digital radiography systems including the effect of focal spot, magnification, scatter, and detector characteristics. In *Proc. SPIE Med. Imag.: Physics of Medical Imaging*, volume 5745, pages 419–429, 2005.

[123] G. K. Yadava, S. Rudin, A. T. Kuhls-Gilcrist, and D. R. Bednarek. Generalized objective performance assessment of a new high-sensitivity microangiographic fluoroscopic (HSMAF) imaging system. In *Proc. Soc. Photo Opt. Instrum. Eng.*, page 69130U, 2008.

[124] V. Yaghmai, M. Rohany, A. Shaibani, M. Huber, H. Soud, E. J. Russell, and M. T. Walker. Pulsatility imaging of saccular aneurysm model by 64-slice CT with dynamic multiscan technique. *J. Vasc. Interv. Radiol.*, 18:785–788, 2007.

[125] K. Yasuno, K. Bilguvar, P. Bijlenga, S. K. Low, B. Krischek, G. Auburger, M. Simon, D. Krex, Z. Arlier, and et al. Genome-wide association study of intracranial aneurysm identifies three new risk loci. *Nat. Genet.*, 42(5):420–425, 2010.

[126] R. Zeng, J. A. Fessler, and J. M. Balter. Estimating 3-D respiratory motion from orbiting views by tomographic image registration. *IEEE Trans. Med. Imag.*, 26(2): 153–163, 2007.

[127] C. Zhang, R. Cardenes, J. Margeta, M.-C. Villa-Uriol, J. Macho, and A. F. Frangi. Spatiotemporal iterative reconstruction of cerebral vasculature from rotational angiography. In *MICCAI 2010 Workshop - STIA'10: Spatio-Temporal Image Analysis for Longitudinal and Time-Series Image Data*, 2010.

[128] C. Zhang, M. De Craene, M.-C. Villa-Uriol, J. M. Pozo, B. H. Bijnens, and A. F. Frangi. Estimating continuous 4D wall motion of cerebral aneurysms from 3D rotational angiography. In *G.-Z. Yang et al. (Eds.): MICCAI2009, LNCS5761*, pages 140–147, 2009.

[129] C. Zhang, M.-C. Villa-Uriol, R. Cardenes, V. Costalat, A. Bonafé, and A. F. Frangi. In-vivo quantification of cerebral aneurysm wall motion from 3DRA and DSA. 2011. submitted.

[130] C. Zhang, M.-C. Villa-Uriol, M. De Craene, J. M. Pozo, and A. F. Frangi. Morphodynamic analysis of cerebral aneurysm pulsation from time-resolved rotational angiography. *IEEE Trans. Med. Imag.*, 28(7):1105–1116, 2009.

[131] C. Zhang, M.-C. Villa-Uriol, M. De Craene, J. M. Pozo, J. Macho, and A. F. Frangi. Dynamic estimation of three-dimensional cerebrovascular deformation from rotational angiography. *Med. Phys.*, 38(3):1294–1306, 2011.

[132] C. Zhang, M.-C. Villa-Uriol, and A. F. Frangi. Evaluation of an efficient GPU implementation of digitally reconstructed radiographs in 3D/2D image registration. In *Proc. SPIE Med. Imag.: Image Processing*, page 762333, 2010.

[133] C. Zhu, R. H. Byrd, and J. Nocedal. L-BFGS-B: Algorithm 778: L-BFGS-B, FORTRAN routines for large scale bound constrained optimization. *ACM Trans. Math. Software*, 23(4):550–560, 1997.

Publications during Thesis Work

International Journal

1. **C. Zhang**, M.-C. Villa-Uriol, R. Cardenes, V. Costalat, A. Bonafé, A.F. Frangi, In-vivo quantification of cerebral aneurysm wall motion from 3DRA and DSA, submitted, 2011.

2. M. Mazzeo, L. Carotenuto, **C. Zhang**, I. Larrabide, M.-C. Villa-Uriol, A.F. Frangi, Fast resampling and real-time X-ray visualisation of time-varying unstructured data, submitted, 2011.

3. V. Costalat, M. Sanchez, D. Ambard, L. Thines, N. Lonjon, F. Nicoud, H. Brunel, J.P. Leje-une, H. Dufour, P. Bouillot, JP Lhaldky, K. Kouri, F. Segnarbieux, CA Maurage, K Lobote-sis, M.-C. Villa-Uriol, **C. Zhang**, A.F. Frangi, G. Mercier, A. Bonafé, L. Sarry, and F. Jourdan, Biomechanical wall properties of human intracranial aneurysms resected following surgical clipping, under review, 2011.

4. **C. Zhang**, M.-C. Villa-Uriol, M. De Craene, J.M. Pozo, J. Macho, A.F. Frangi, Dynamic estimation of three-dimensional cerebrovascular deformation from rotational angiography, Medical Physics, 38(3): 1294-1306, 2011.

5. M.-C. Villa-Uriol, I. Larrabide, J.M. Pozo, M. Kim, O. Camara, M. De Craene, **C. Zhang**, A. Geers, H. Morales, H. Bogunović, R. Cardenes, A.F. Frangi, Toward integrated management of cerebral aneurysms, Philosophical Transactions of the Royal Society A, 368(1921): 2961-2982, 2010.

6. **C. Zhang**, M.-C. Villa-Uriol, M. De Craene, J.M. Pozo, A.F. Frangi, Morphodynamic analysis of cerebral aneurysm pulsation from time-resolved rotational angiography, IEEE Transactions on Medical Imaging, 28(7): 1105-1116, 2009.

Book Chapter

1. M.-C. Villa-Uriol, I. Larrabide, J.M. Pozo, M. Kim, M. De Craene, O. Camara, **C. Zhang**, A. Geers, H. Bogunović, H. Morales, A.F. Frangi, Cerebral

aneurysms: A patient-specific and image-based management pipeline, J.M. Tavares and R.M. Jorge, eds.: Computational Vision and Medical Image Processing - Recent Trends, Springer book series Computational Methods in Applied Sciences, 327-349, 2011.

International Journal Abstract

1. **C. Zhang**, M.-C. Villa-Uriol, M. De Craene, J.M. Pozo, A.F. Frangi, Time-resolved 3D rotational angiography reconstruction: Towards cerebral aneurysm pulsatile analysis, International Journal of Computer Assisted Radiology and Surgery, v3, S44-46, 2008.

Peer-reviewed International Conference

1. **C. Zhang**, R. Cardenes, J. Margeta, M.-C. Villa-Uriol, J. Macho, A.F. Frangi, Spatiotemporal iterative reconstruction of cerebral vasculature from rotational angiography, MICCAI 2010 Workshop - STIA'10: Spatio-Temporal Image Analysis for Longitudinal and Time-Series Image Data, 2010.

2. **C. Zhang**, M.-C. Villa-Uriol, A.F. Frangi, Evaluation of an efficient GPU implementation of digitally reconstructed radiographs in 3D/2D image registration, SPIE Medical Imaging: Image Processing, page 762333, 2010.

3. **C. Zhang**, M. De Craene, M.-C. Villa-Uriol, J.M. Pozo, B.H. Bijnens, A.F. Frangi, Estimating continuous 4D wall motion of cerebral aneurysms from 3D rotational angiography, International Conference on Medical Image Computing and Computer Assisted Intervention (MICCAI), Part I, LNCS 5761, 140-147, 2009.

International Conference Abstract

1. M.-C. Villa-Uriol, **C. Zhang**, A.F. Frangi, Evaluation of cerebral aneurysm pulsatility on 3DRA and 4DCTA images, International Intracranial Stent Symposium, 2008.

Curriculum Vitae

Chong Zhang has received her M.Sc. and B.E. degree in Electrical Engineering from the Northwestern Polytechnical University, China, in 2004 and 2001, respectively. Afterwards, she worked as research student on digital geometry processing algorithms at Nanyang Technical University, Singapore, and as scientific developer on 3D facial biometrics at CISTIB in Universitat Pompeu Fabra, Barcelona. Since September 2006, she started at CISTIB to work on image registration and reconstruction algorithms on X-ray angiographic images for cerebrovascular morphodynamics estimation, part of which is summarized in this PhD thesis.

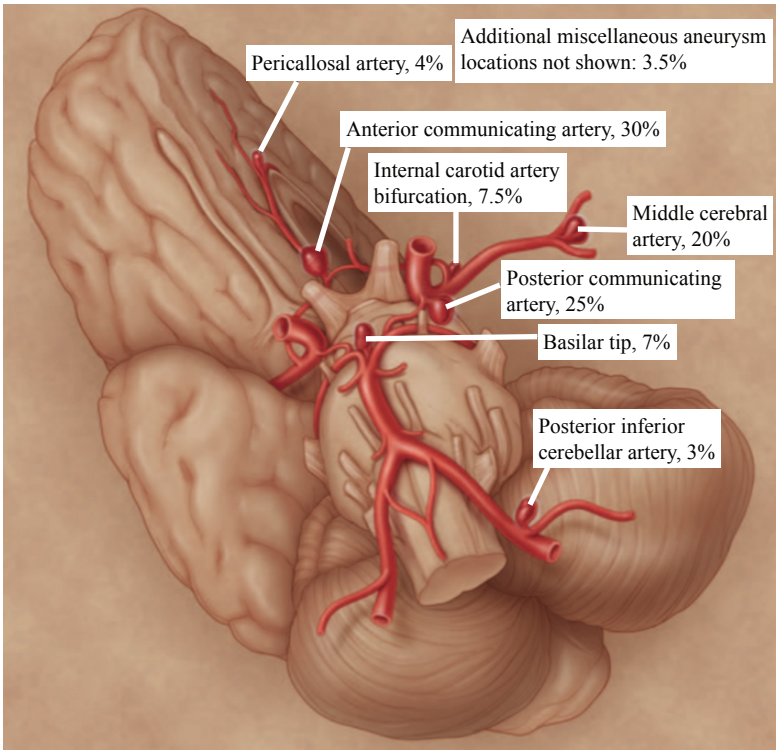

Figure 1.2 (*page 4*): The most frequent locations of cerebral aneurysms in the intracranial vasculature. Reproduced with permission from [14].

Figure 1.3 (*page 9*): A picture of a flat panel 3DRA system Allura Xper FD20 (Philips Healthcare, Best, The Netherlands). 1. X-ray source; 2. Image detector; 3. C-arm that rotates around the patient; 4. Patient table.

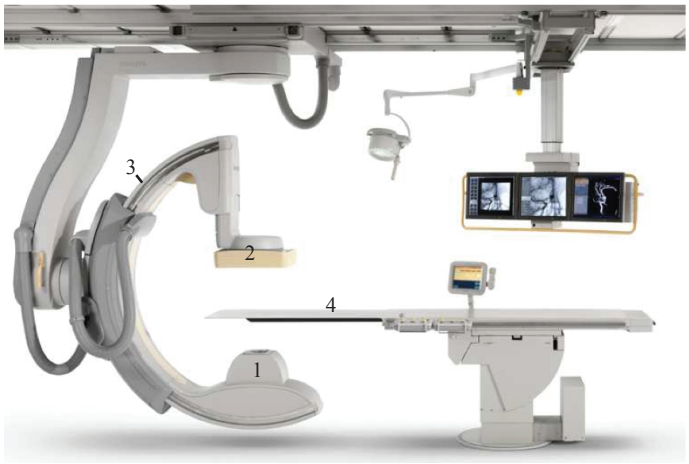

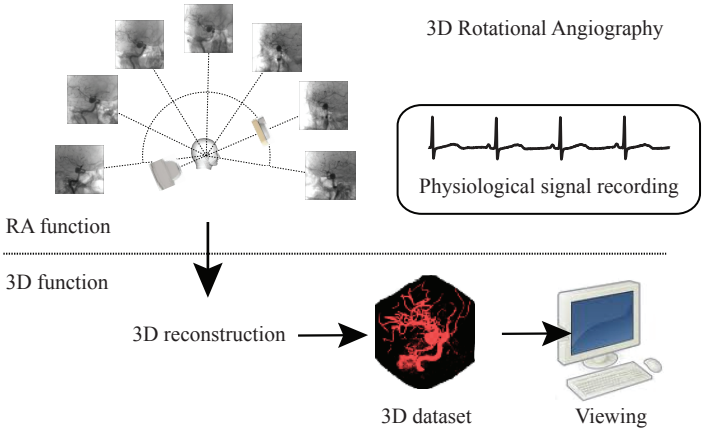

Figure 1.4 (*page 10*): An illustration of the imaging principle of the 3DRA modality. More than 100 contrast-enhanced images are acquired by rotational angiography during a 4-second scan, at constant time intervals and uniformly distributed over more than 200° along a circular trajectory. A 3D volume automatically reconstructed from these image date can be viewed with real-time volume rendering. During the rotational run, a physiological signal can be synchronously recorded as well.

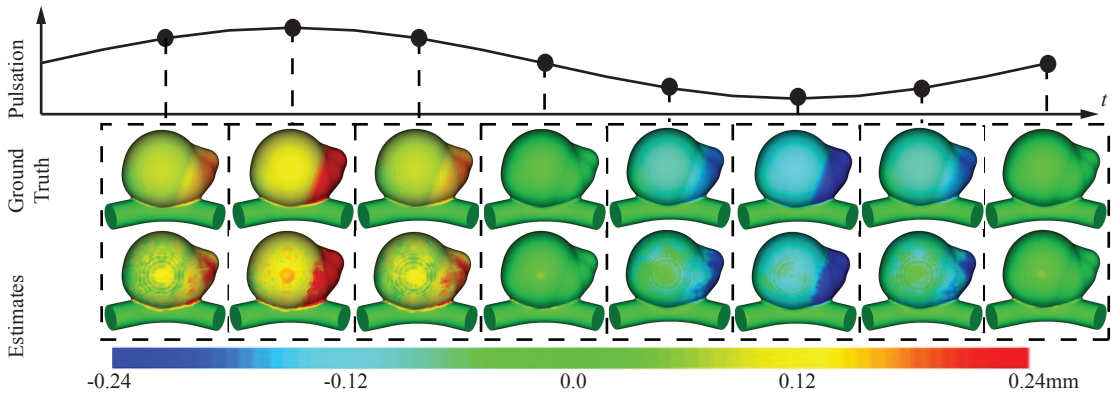

Figure 2.7 (*page 27*): Instantaneous estimated pulsation amplitude distribution at 8 (*dots*) time points referenced to the ground truth pulsation curve. A 12-mm aneurysm with pulsation of 4% (0.48 mm). Ground truth (*top*) is compared to the results from our method (*bottom*).

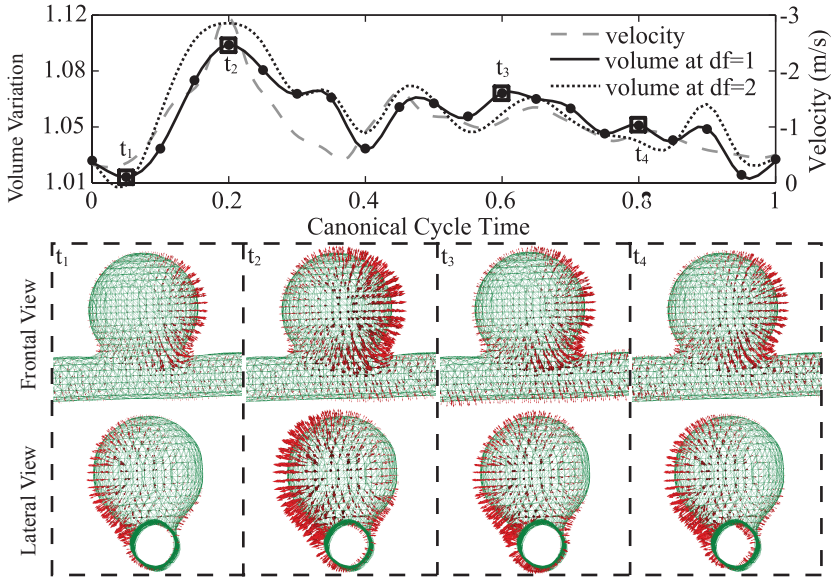

Figure 2.16 (*page 37*): (a) The obtained volume variations with two downsampling factors df=1,2, along with the Doppler ultrasound velocity waveform. (b) Four (*boxes*) out of 20 (*dots*) estimated time points presenting the instantaneous wall displacements with respect to the reference geometry.

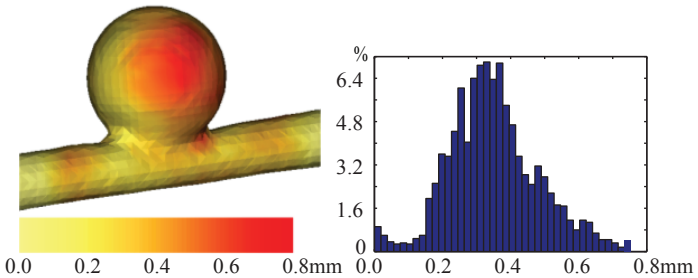

Figure 2.17 (*page 37*): Color-coded displacement range over the cardiac cycle for each point on the surface, and the histogram of the displacement range.

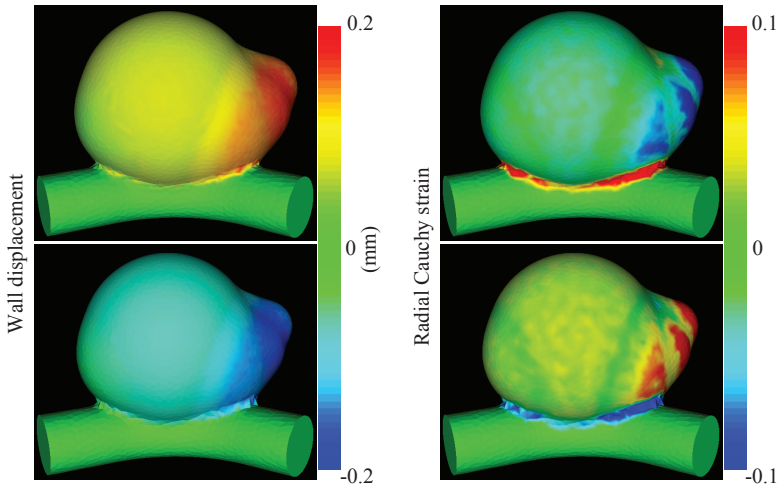

Figure 3.8 (*page 58*): Wall displacement amplitude and radial Cauchy strain at the maximum (*top*) and minimum (*bottom*) deformation states for an *in silico* phantom with diameter of 12 mm and pulsation of 3% (i.e. maximum amplitude of 0.36 mm).

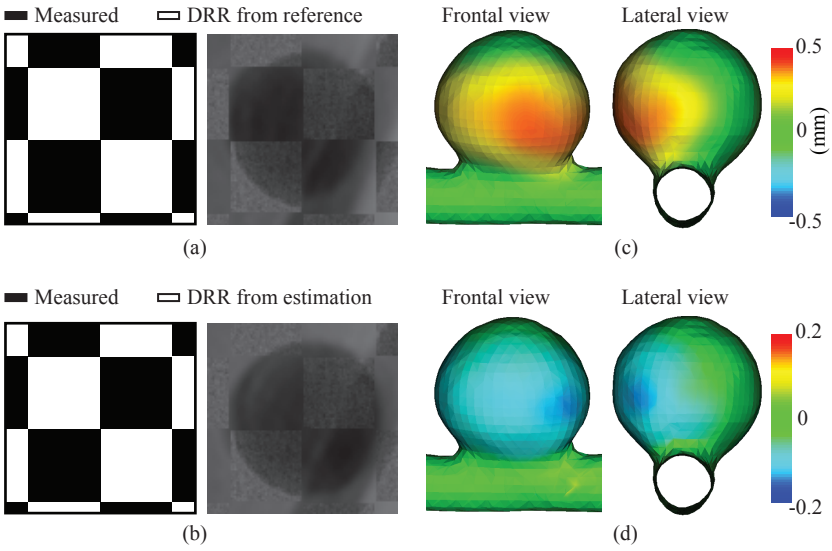

Figure 3.9 (*page 59*): Results from *in vitro* LP phantom: (a,b) Example of checkerboard images for the *in vitro* phantom comparing respectively the measured projection with the equivalent DRR computed from the reference volume and our estimation. The color maps of the wall displacement amplitude (c) and the radial Cauchy strain (d) for the frontal and lateral views at the instant presenting the largest displacement.

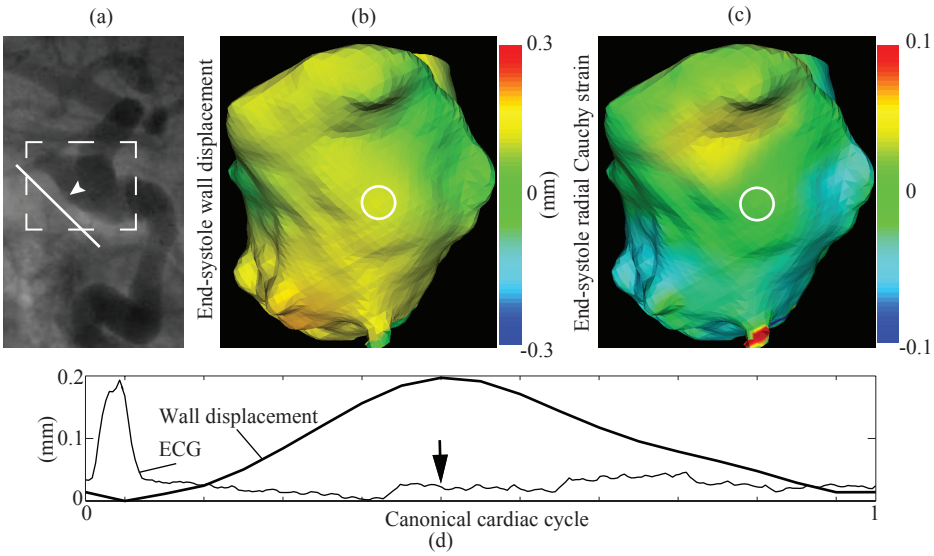

Figure 3.10 (*page 60*): Results of aneurysm wall motion in patient #1. (a) A close view indicating the region where our motion estimation method has been applied (*dashed frame*) in an X-ray angiography. (b) The color map (*line* in (a) indicating the viewing plane) of the displacements around the end-systolic (ES) phase (indicated by the *arrow* in (d)). (c) The radial Cauchy strain at the same phase as in (b). (d) Aneurysm wall displacement amplitude over the cardiac cycle at the location indicated by the *arrow head* in (a) and the *circles* in (b,c).

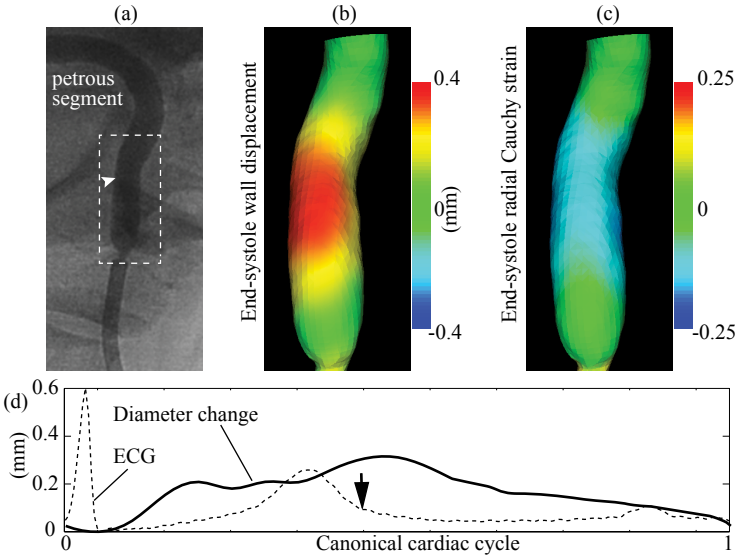

Figure 3.11 (*page 61*): Results of vessel wall motion in patient #2. (a) A close view indicating the region where our motion estimation method has been applied (*dashed frame*) in an X-ray angiography. (b) The color map of the displacements around the end-systolic (ES) phase (indicated by the *arrow* in (d)). (c) The radial Cauchy strain at the same phase as in (b). (d) The vessel diameter change over the cardiac cycle at the location as indicated by the *arrow head* in (a).

Figure 3.12 (*page 62*): Results of catheter tip movements in patient #2. (a) A close view indicating the region where our motion estimation method has been applied (*dashed frame*) in an X-ray angiography. The color maps of the estimated catheter movements (b) and the strain (c) at ten selected time points. (d) The catheter tip (*arrow head* in (a)) longitudinal displacement plotted together with the ECG signal.

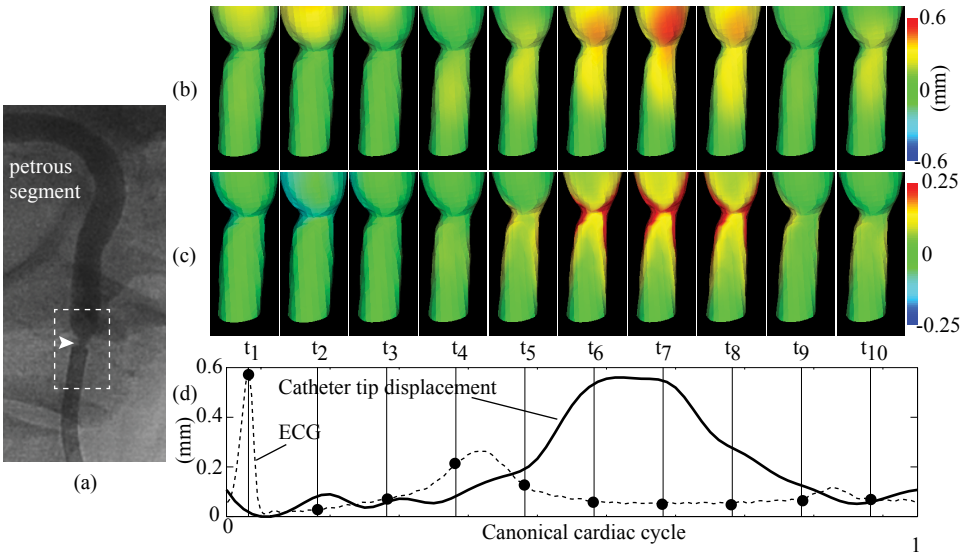

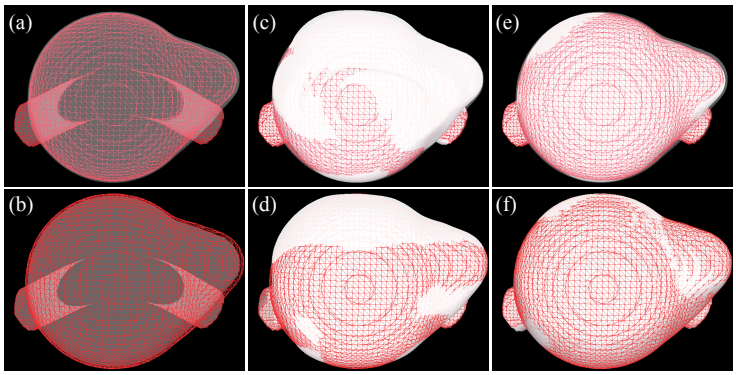

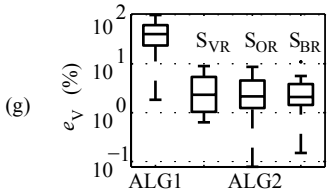

Figure 3.14 (*page 65*): Results comparing the influence of inhomogeneous contrast filling on the method in [130] (denoted as ALG1) and our present technique (denoted as ALG2), using an *in silico* phantom with diameter of 10 mm and pulsation of 4% (i.e. maximum amplitude of 0.4 mm). Results at two instants are shown graphically: (a,c,e) minimum pulsation and (b,d,f) maximum pulsation. The ground-truth shape (*wireframe*) at each time instant is overlaid with: (a,b) the reference, (c,d) the estimation using ALG1, and (e,d) the estimation using ALG2. (g) Comparison of e_V between ALG1 and ALG2 with the three sampling regions: S_{VR} , S_{OR} , and S_{BR} .

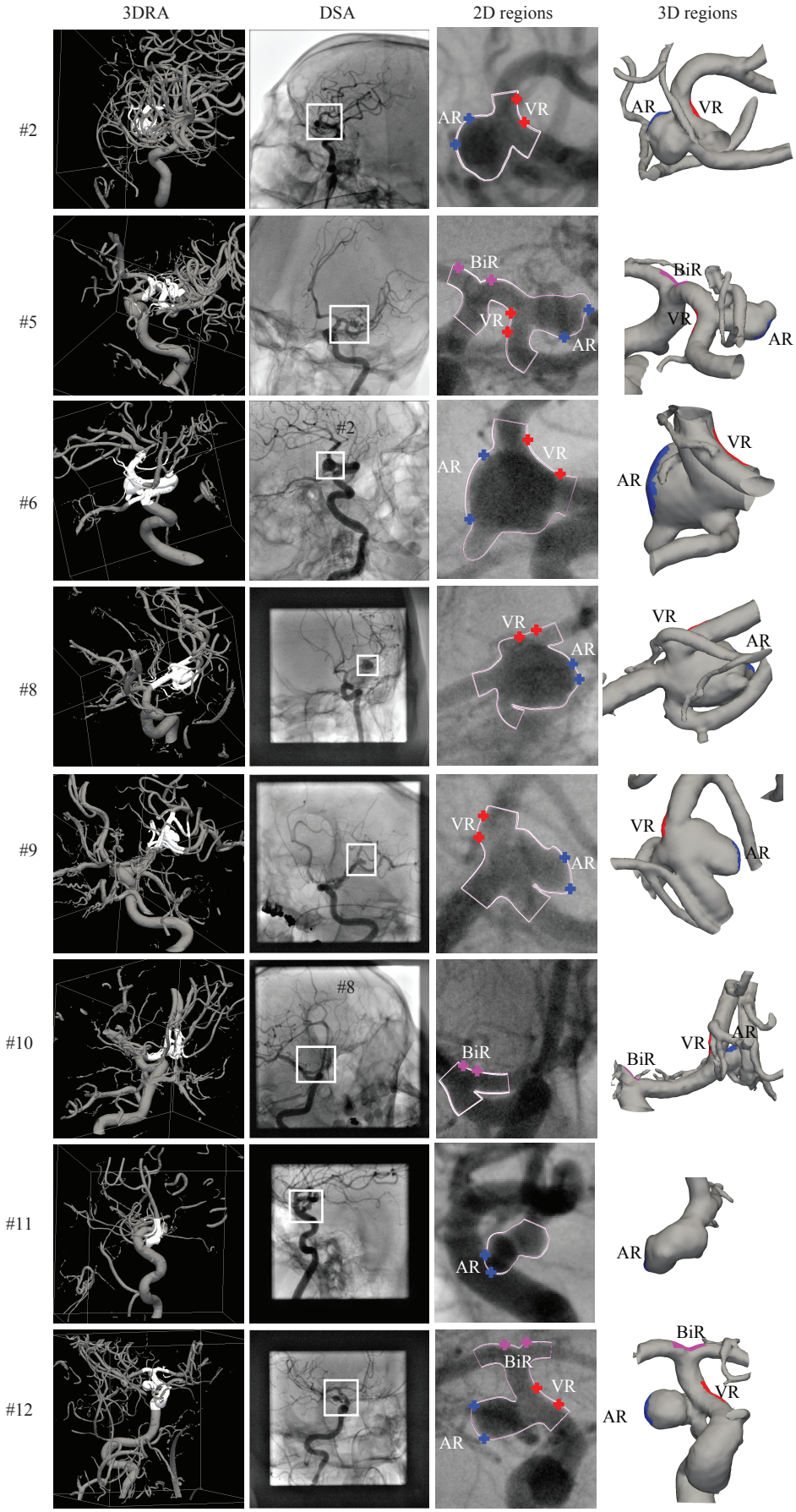

Figure 4.1-2 (*page 75, 76*): Patients #2,5,6,8 and #9,10,11,12: (from *left* to *right*) 3DRA data with the studied region of interest highlighted in different colors: aneurysm region (AR), vessel region (VR) and bifurcation region (BiR); one DSA image; measurement regions on 2D contour delineations (*crosses* indicate the region on the contour); measurement regions on 3D surface.

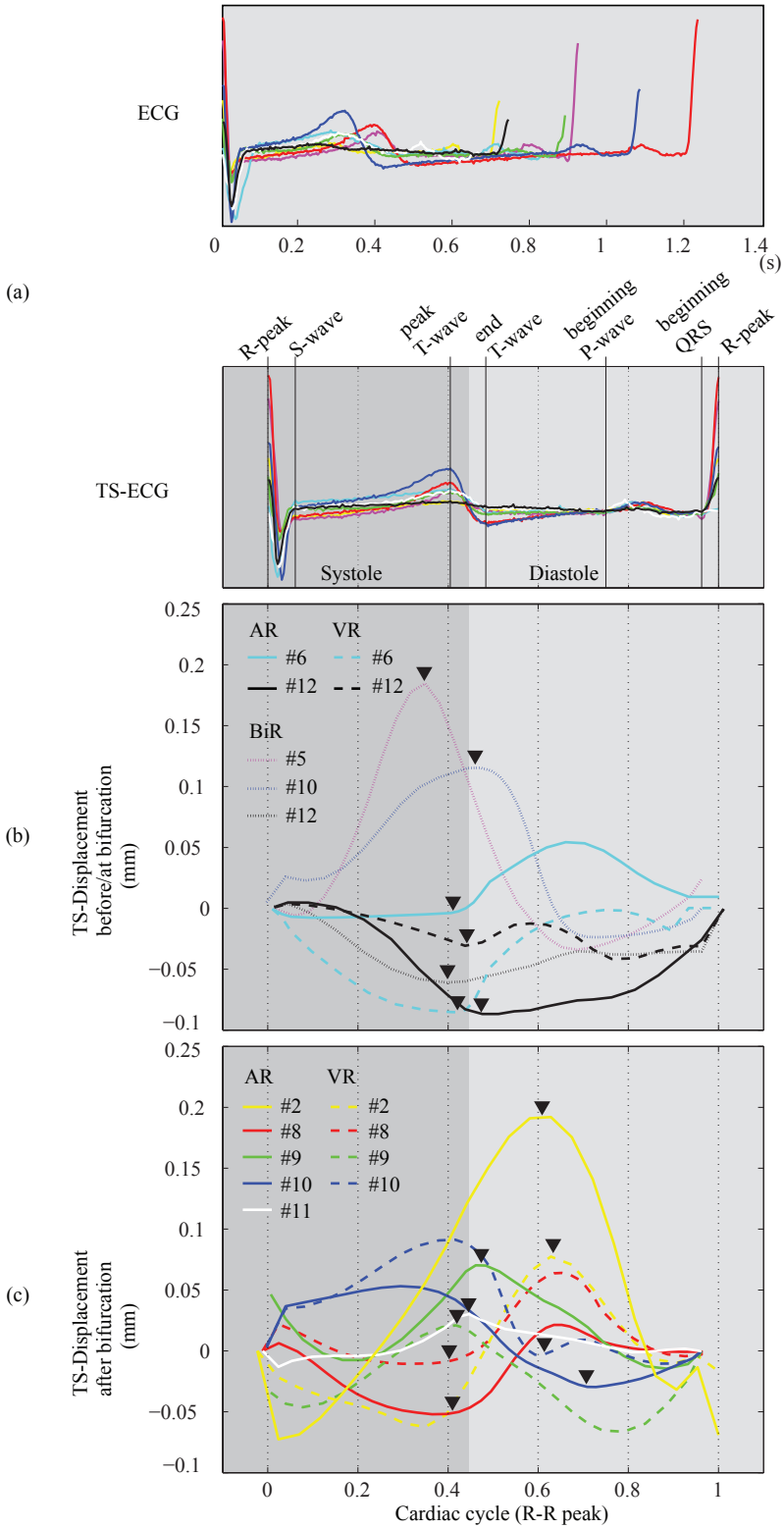

Figure 4.6 (*page 86*): (a) Original ECG waveforms (R-R peak) of the 8 patients and the temporally synchronized ECG (TS-ECG). Synchronization landmarks are also indicated. (b,c) Motion curves of average 3DRA estimated wall displacements after applying the temporal synchronization (TS-Displacement) at regions: right before, or at and after the ICA bifurcation. Triangles indicate the peak motion.